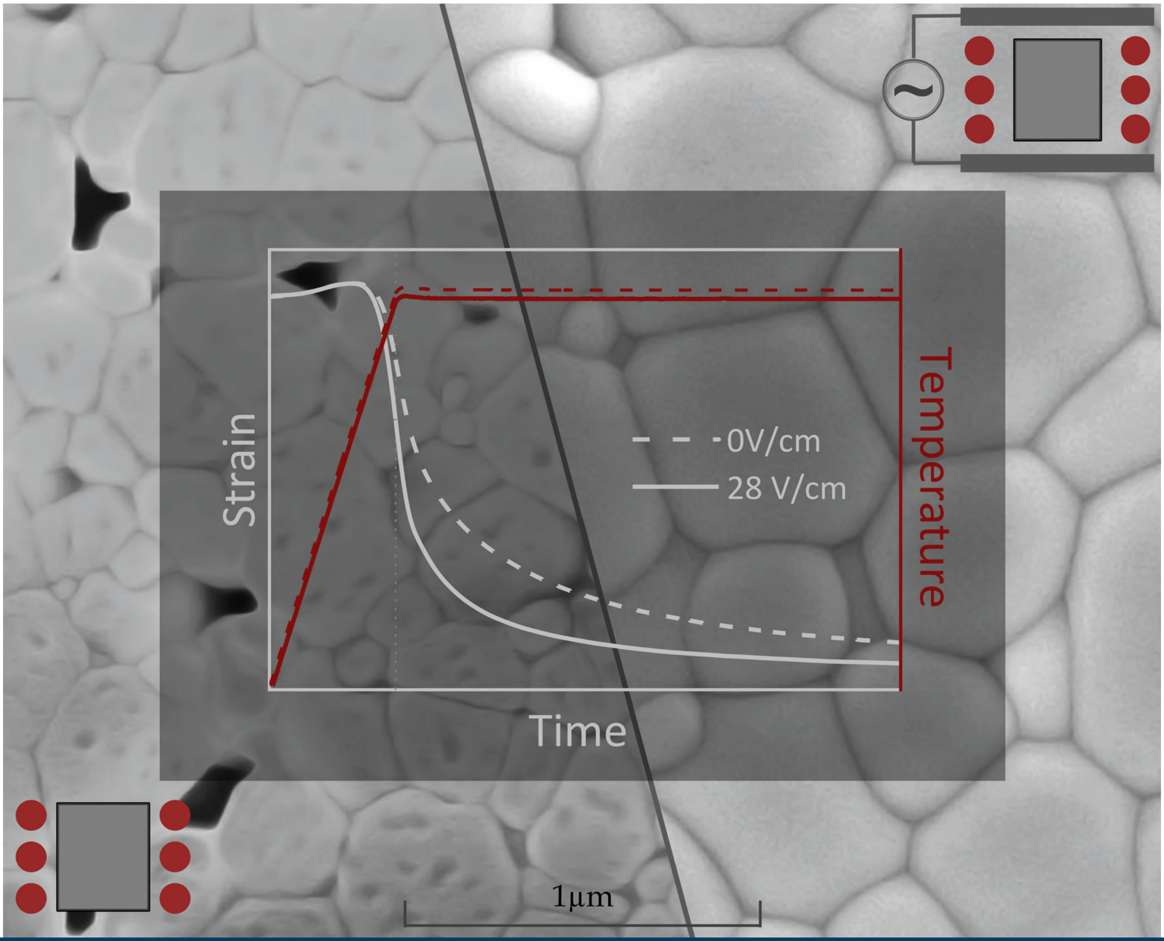

Effect of electric field on the sintering of ceria

Chen Cao

Energie & Umwelt / Energy & Environment
Band / Volume 510
ISBN 978-3-95806-497-3

Mitglied der Helmholtz-Gemeinschaft

JÜLICH
Forschungszentrum

Schriften des Forschungszentrums Jülich
Reihe Energie & Umwelt / Energy & Environment Band / Volume 510

Forschungszentrum Jülich GmbH
Institut für Energie- und Klimaforschung
Werkstoffsynthese und Herstellungsverfahren (IEK-1)

Effect of electric field on the sintering of ceria

Chen Cao

Schriften des Forschungszentrums Jülich
Reihe Energie & Umwelt / Energy & Environment Band / Volume 510

ISSN 1866-1793 ISBN 978-3-95806-497-3

Bibliografische Information der Deutschen Nationalbibliothek.
Die Deutsche Nationalbibliothek verzeichnet diese Publikation in der
Deutschen Nationalbibliografie; detaillierte Bibliografische Daten
sind im Internet über http://dnb.d-nb.de abrufbar.

Herausgeber und Vertrieb: Forschungszentrum Jülich GmbH
Zentralbibliothek, Verlag
52425 Jülich
Tel.: +49 2461 61-5368
Fax: +49 2461 61-6103
zb-publikation@fz-juelich.de
www.fz-juelich.de/zb

Umschlaggestaltung: Grafische Medien, Forschungszentrum Jülich GmbH

Druck: Grafische Medien, Forschungszentrum Jülich GmbH

Schriften des Forschungszentrums Jülich
Reihe Energie & Umwelt / Energy & Environment, Band / Volume 510

D 82 (Diss. RWTH Aachen University, 2020)

ISSN 1866-1793
ISBN 978-3-95806-497-3

Kurzzussamenfassung

Das Sintern mit Unterstützung elektrischer Felder hat als Alternative zum konventionellen Verfahren seit langem das Interesse in der Forschung geweckt, mit der Erwartung, durch den neuen Ansatz die Sinterzeiten deutlich reduzieren und die Materialeigenschaften des gesinterten Körper gezielter einstellen und verbessern zu können. In den letzten Jahren durchlief das feldunterstützte Sintern (Field Assisted Sintering, FAST) eine rasante Entwicklung als Herstellungsmethode von Werkstoffen, die durch konventionelles Sintern nur schwer oder überhaupt nicht hergestellt werden können [1]. Ein Schwerpunkt in der akademischen Forschung wird auf das 'Flash-Sintern' gelegt, bei dem die Verdichtung innerhalb von Sekunden abgeschlossen ist [2]. Die grundlegenden physikalischen Prinzipien des feldunterstützten Sinterns sind jedoch nach wie vor unklar.

In dieser Arbeit wurde das Sintern von yttriumdotierten Ceroxid-Proben (10 Mol-% yttriumdotiertes Ceroxid, 10YDC, und 0,1 Mol-% yttriumdotiertes Ceroxid, 01YDC) unter elektrischen Wechselfeldern bei 50Hz und Feldstärken bis zu 28V/cm untersucht, die deutlich schwächer sind als solche, die für das 'Flash-Sintern' erforderlich sind. Zum ersten Mal wurde die Abhängigkeit der Sinterparameter von den angelegten elektrischen Feldern bei konstanter Probentemperatur untersucht, was durch direkte Messungen im Inneren der Probe und durch thermoelektrische Finite-Elemente-Simulationen sichergestellt wurde. Dadurch konnte die makroskopische Joulsche Erwärmung ausgeschlossen und die auftretenden Mechanismen analysiert werden. Darüber hinaus konnte erstmals das symmetrische Verhalten unter Druck- und Zugbelastung experimentell verifiziert werden. Dieser Teil der Arbeit wurde während eines Forschungsaufenthaltes am National Institute for Materials Science (NIMS), Japan, durchgeführt.

Unter elektrischen Wechselfeldern verformt sich yttriumdotiertes Ceroxid leichter, was sich in einer geringeren uniaxialen Sinterviskosität zeigt; die treibende Kraft für die Verdichtung beim Sintern wird größer, angezeigt durch eine höhere uniaxiale Sinterspannung. Die Aktivierungsenergien für die Verdichtung nehmen durch die Erhöhung der elektrischen Feldstärken ab, dies war besonders ausgeprägt bei 10YDC: Dessen Aktivierungsenergie verringerte sich von 502±40 kJ/mol bei feldfreiem Sintern bis auf 311±25 kJ/mol unter E_{rms}=28 V/cm, während die Aktivierungsenergie für 01YDC unter gleichen Bedingungen moderat von 485±39 auf 439±37 kJ/mol sank. Darüber hinaus wurden die Ionenleitfähigkeiten gemessen, um herauszufinden, ob Korngrenzen und die damit verbundenen Raumladungsschichten durch die elektrischen Felder irreversibel verändert werden. Die Korngrenzenleitfähigkeit von 10YDC nahm mit längerer Haltezeit beim feldfreien Sintern leicht ab und

stieg bei Proben, die unter einem stromlosen elektrischen Feld gesintert wurden, an; die Korngrenzenleitfähigkeit von 01YDC zeigte unter gleichen Bedingungen keine Veränderungen. Die während des Sinterns angelegten elektrischen Felder veränderten nicht die Aktivierungsenergie für die Ionenleitfähigkeiten im Kornvolumen oder an den Korngrenzen auch für 10YDC, verringerten jedoch die effektive Kapazität der Korngrenzen. Letzteres ist die Ursache für die erhöhte Korngrenzenleitfähigkeit beim feldunterstützt gesinterten 10YDC.

Da die makroskopische Erwärmung durch das Feld ausgeschlossen wurden, werden folgende zwei mögliche Mechanismen für den beobachteten Feldeffekt vorgeschlagen: entweder eine mikroskopische Joule-Erwärmung an den Sinterhälsen und Korngrenzen oder eine direkte Wirkung des Feldes auf die Korngrenzendiffusionsprozesse. Letztere Ursache wird favorisiert, da die erwähnte Erhöhung der Korngrenzenleitfähigkeit zusammen mit einer Änderung des Oxidationszustandes der Cer-Ionen in der Grenzflächenstruktur durch eine transmissionselektronenmikroskopische Analyse beobachtet wurde. Es ist erwähnenswert, dass diese Veränderungen *ex-situ* bei einer niedrigen Temperatur beobachtet wurden. Eine Quantifizierung der *in-situ*-Korngrenzenstruktur während des Sinterns bleibt ein offenes und herausforderndes Problem. Dennoch können diese Phänomene den mikroskopischen Joule-Erwärmungseffekt nicht vollends ausschließen, vielmehr sind Charakterisierungsmethoden mit hoher räumlicher und zeitlicher Auflösung sowie *in-situ*-Techniken für die weitere Erforschung des feldunterstützten Sinterns unerlässlich.

Abstract

As one of the alternative to conventional sintering, the application of electrical fields during sintering has aroused interest since decades, aiming at reducing the sintering time as well as improving the targeted material properties. Field assisted sintering (FAST) has undergone rapid development in the last years, as it provides a platform for manufacturing materials which are difficult or even impossible to be produced by conventional sintering [1]. More recently, strong focus is put on 'flash sintering' in the academia, where the densification completes within seconds [2]. However, the governing principles behind the field assisted sintering are still unveiled.

In this work, the sintering of yttria-doped ceria samples (10 mol % yttrium doped ceria, 10YDC, and 0.1 mol % yttrium doped ceria, 01YDC) was studied under alternating electrical fields with a frequency of 50 Hz and field strengths significantly weaker than those required for the 'flash regime'. For the first time, the dependence of sintering parameters on the applied electrical fields was investigated with constant sample temperatures, which was ensured by direct temperature measurement inside the sample and by thermo-electric finite element simulations. This excluded the macroscopic Joule heating and allowed to investigate the occurring mechanisms. In addition, the symmetric behavior under compressive and tensile loading could be experimentally verified for the first time. This part of study was done during a research stay in National Institute for Materials Science (NIMS), Japan.

Under AC electric fields, yttrium doped ceria is deformed more easily, as shown by a lower uniaxial sintering viscosity, and the driving force for densification during sintering becomes larger, as revealed by a higher uniaxial sintering stress. This points to the existence of other mechanisms because the macroscopic thermal effects were excluded beforehand. In order to gain a deeper understanding of the experimental results, activation energies of the material system were measured under AC electric fields with a frequency of 50 Hz. The activation energies for the densification decrease by the increase of electrical field strengths, exerting larger effects for 10YDC. The activation energy for the densification of 10YDC decreased very significantly from 502±40 kJ/mol without electrical fields to 311±25 kJ/mol under E_{rms}=28 V/cm; it also reduced, but moderately, for 01YDC from 485±39 kJ/mol to 439±37 kJ/mol for the same conditions. In addition, ionic conductivities were measured to find out whether grain boundaries and related space charge layers are irreversibly modified by the electrical fields. The grain boundary conductivity of 10YDC decreased slightly after a longer holding time during fieldless sintering; it increased under the application of a non-contacting electrical field during sintering. On the other hand, the grain boundary conductivity of 01YDC did not change under the same conditions. The electrical

fields applied during sintering did not change the activation energy for the ionic conductivities of neither bulk nor grain boundary even for 10YDC, but decreased the grain boundary effective capacitances which is the origin of the higher grain boundary conductivity for 10YDC sintered under electrical field.

As the effect of macroscopic Joule heating was excluded in the experiments the following two possible mechanisms for the observed field effect are proposed: either microscopic Joule heating at the sintering necks and grain boundaries or a direct effect of the field on the grain boundary diffusion processes. The latter is favored, because the above mentioned increase of the grain boundary conductivities were observed together with a change of the valence state of the cerium ions in the vicinity of the grain boundary as analysed by transmission electron microscopy. It is worth mentioning that these changes were observed *ex-situ* at a low temperature. A quantification of the *in-situ* grain boundary structure during sintering remains an open and challenging investigation. Nevertheless, these phenomena could not exclude the microscopic Joule heating effect completely, therefore, characterization methods with high spatial and temporal resolution as well as the *in-situ* techniques are essential for further research of field assisted sintering.

Contents

Nomenclature

Symbols

Fundamental of Sintering

σ	Laplace pressure [Pa]
Ω	atomic or molar volume [m^3]
c_v	concentration of vacancy under the curved surface [1/m^3]
c_{v0}	vacancy concentration without chemical potential gradient [1/m^3]
$\Delta\mu$	chemical potential difference [J/mol]
x, ρ	principal radii of two particles [m]
r	radius of pores/particles [m]
γ_s	specific surface energy [J/ m^2]
P	porosity
ϕ	stress intensification factor

Continuum mechanics of sintering

d	grain size [m]
$\bar{\rho}$	relative density [%]
$\sigma_z, \sigma_r, \sigma_\theta$	stress components along the principal axes [Pa]
$\dot{\epsilon}_f$	free strain rate [1/s]
$\dot{\epsilon}_r, \dot{\epsilon}_z$	sintering rate component along the principal axes [1/s]
E_p, G_p, K_p	uniaxial viscosity, shear viscosity and bulk viscosity [Pa.s]
υ_p	viscous Poisson's ratio
σ_z^s	uniaxial sintering stress [Pa]
Σ	hydrostatic sintering potential [Pa]

Ionic conductivity

δ	grain boundary thickness [m]
σ^{gi}	grain interior conductivity [S/m]
R^{gi}	grain interior resistance [Ω]
C^{gi}	effective grain interior capacitance [F]
σ^{gb}	grain boundary conductivity [S/m]
R^{gb}	grain boundary resistance [Ω]
C^{gb}	effective grain boundary capacitance [F]

Constants

k	Boltzmann constant [J/K]
R	gas constant [J/mol·K]

Abbreviations

01YDC	0. 1 mol % yttrium doped ceria
10YDC	10 mol % yttrium doped ceria
gi	grain interior
gb	grain boundary
PSD	particel size distribution
DTA	Differential thermal analysis
TG	Thermogravimetric analysis
EIS	Electrochemical impedance spectroscopy
XAS	X-ray absorption spectroscopy

List of Figures

List of Tables

1.Introduction

The history of sintering began around 25000 years ago when people fired clay to produce utensils [1]. Sintering, completed even by our ancestors without much knowledge of todays material science, is basically the process of transforming a powder compact into a dense object with specific properties. With the development of society and technology, properties other than mechanical properties, such as electrical, thermal and thermo-electrical properties, have become increasingly important. In order to achieve these varying properties, other techniques apart from the conventional sintering process [1], such as vacuum sintering, hot pressing, liquid assisted sintering, cold sintering and electrical field assisted sintering [2], were also developed. Among all the techniques, field assisted sintering seems to be very promising. The application of external electrical fields offers the opportunity to produce materials with tailored properties that are difficult to obtain with a conventional approach.

The emergence of the field assisted sintering/spark plasma sintering technique (FAST/SPS) methods enables the production of dense products with shorter time and smaller grain sizes. These advantages drive the worldwide market for the field assisted sintering process, which covers a wide scope of industries, such as automotive, manufacturing, energy and so on. There are also industrial application of flash sintering: Lucideon Group Limited, Staffordshire, UK. It is known to manufacture products using flash sintering technique. However, the limited understanding of the mechanisms of field assisted sintering, and thus the difficulties in tuning and controlling the microstructure preciously restrict the market growth to an extent. Convincing explanations are yet to be found, for example, for the abnormal grain growth on either anode or cathode side [3] and for the inhomogeneous distribution of temperature for large scale samples [4].

Many attempts have been made to understand the effect of external fields on the sintering process. These studies are mainly focused on two different kinds of electrical field applications. The first kind is to use low voltage together with high current density, such as FAST/SPS [2,4], during which the powders are typically sintered under high external mechanical pressure. For materials with low conductivity such as ceramics, the electrical fields have no direct effect on materials (e.g. alumina [5] and fully stabilized zirconia [6]). Fast heating rates together with high mechanical loads enhance the densification. However, for materials with higher conductivity, electrical fields increase the sinterability via the interactions between current and the material, such as Joule heating [4,7], percolation effects [8-9] and electrochemical reactions [10-11]. The second kind is to use higher electric fields than the FAST/SPS condition, and the mechanical load is usually applied only to maintain the contact between electrodes and specimens (cylindrical or dog-bone shape specimens are used). One well-known example of this kind is named flash sintering, during which the densification occurs within a few seconds [3,12]. Hypothesis has been proposed either by attributing the amplified mass transport to a facilitated defect generation under electric fields [3,12-13], or by assuming that Joule heating effects, especially macroscopic Joule heating, together with high heating rates, yields a significant improvement of the sintering rate [14-18].

In summary, both thermal and field related effects exist during field assisted sintering, but neither alone can explain all the phenomena for most cases. Thermal effects cannot explain that the type and concentration of defects in ZnO is irreversibly modified by electric fields, even without current flowing through the sample [19]. As pointed out by Conrad *et al.* [20], the effect of AC fields yielding both increasing sintering rate and suppressed grain growth is more significant than with equivalent DC fields, which should yield the same temperature increase. On the other hand, the field effect alone cannot explain that the external electrical field required to generate defects is beyond the simulated dielectric strength of the materials [21]. In addition, previous studies have already shown a field related improvement of sintering for many ceramics even under lower electric field strengths than the field strength required for flash sintering [22-23].

Many studies have been conducted on flash sintering motivated by the promising accomplishment of sintering in a small time interval. However, the dramatic temperature change during flash sintering brings difficulties in measuring the specimen temperature. Without an accurate measurement of specimen temperature, it is impossible to separate the thermal effect and field effect. These two effects co-exist during field assisted sintering process, with potentially one of them dominating under a certain condition. Thus, only by separating the effects one from each another, mechanisms can be identified. Therefore, small fields should be investigated to study the sintering behavior without the problems that the uncontrolled speed of flash sintering causes.

The goal of this thesis is to investigate the mechanisms of field assisted sintering by decoupling the field effect and thermal effect. More specifically, the following points have been of interest, and the possible answers to the following questions are given in the thesis.

- Can discontinuous loading-dilatometry be used for the measurement of sintering parameters under electrical fields?

- Can the compressive response can be extrapolated into the tensile regime in the frame of continuum mechanics of sintering?

- How are the sintering parameters like viscosity, viscous Poisson’s ratio and sintering stress influenced by moderate electrical fields?
- What can be the possible mechanism for improved sintering besides macroscopic thermal effect?
- Are ionic conductivity and related space charge layers irreversibly modified?

2. Background and current knowledge

2.1 Fundamentals of sintering

Ceramics is an important category of materials usually applied in daily life and industry. Ceramics usually have high melting points and are mechanically brittle, so their manufacturing requires techniques that are more complex than those for metal forming (relying on plastic deformation or casting). Sintering is one technology that has been used for a long time. It involves various aspects such as material composition, powder particle size, morphology, homogeneity of green compact, temperature, external mechanical pressure applied, sintering atmosphere and so on. All these parameters influence synergistically the thermal or chemical reaction activated diffusion processes during the sintering.

Sintering can be categorized through the phases present during the process, into four kinds [24]:

1. Solid-state sintering: the green body is usually heated to a homologous temperature between 0.5 and 0.9 of the melting temperature. During the sintering, no liquid phases are formed and the diffusion process happens only in the solid state.
2. Liquid phase sintering: a small amount of liquid is present during sintering. On one hand the liquid phase helps enhancing the sintering process at lower temperature, on the other hand, the existence of both liquid and solid phases also limits the temperature applied during the subsequent operations.
3. Vitrification: a large volume of liquid (typically greater than ~25% of the original solid volume) is present during sintering. The required density can be easily achieved by the formation of liquid phase, the flow of this liquid phase into pores, and the vitrification of this liquid phase during cooling.
4. Viscous sintering: This term is usually attributed to the sintering of amorphous materials (glass). With no existence of grain boundaries, the densification happens by viscous flow associated with particle deformation.

The whole sintering process can be divided into three stages based on the increase of relative density together with the decrease of porosity [1]. A typical densification curve of the sintering process is illustrated in Figure 1, and the three stages are listed below:

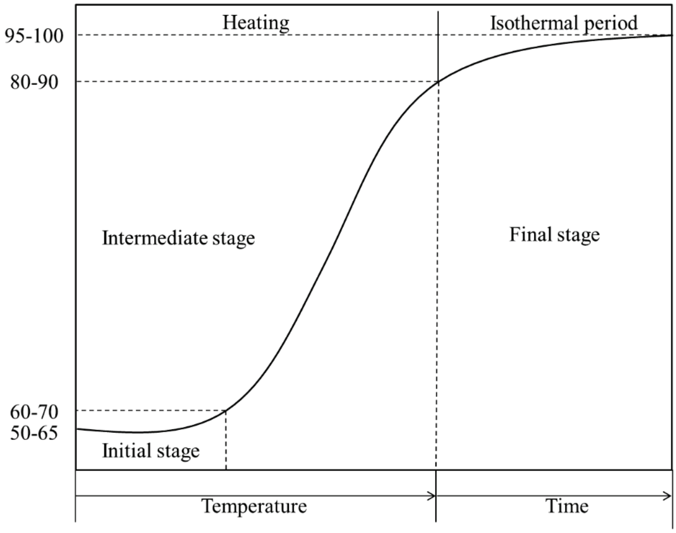

Figure 1: Typical densification curve during sintering as a function of temperature and time [6].

1. Initial stage: Between neighboring particles, a neck forms and grows. Almost no shrinkage (less than 3 %) takes place during this phase and pores are interconnected with one another.
2. Intermediate stage: The major shrinkage and densification happen during this stage and the pores become isolated from one another. Typically, grain growth also starts at this stage.
3. Final stage: Open pores become isolated pores on the grain boundary (porosity less than 8 %). Further densification continues and grain growth starts to become significant. In addition, the removal of the last percentages of porosity renders difficulties.

During the sintering process, the increase of relative density, together with the decrease of porosity, involves the change of material microstructure. The microstructure determines in turn various properties of material such as electrical conductivity, mechanical properties and optical properties, which are essential for applications.

2.2 Driving forces and mass transport

The increase of relative density, together with the decrease of porosity, is realized by the mass transfer along concentration gradients. From the thermodynamic point of view, this migration is driven by lowering total free energy of system, which is a global driving force. From the kinetic point of view, this migration is driven by a local driving force caused by chemical potential [1]. In principle, particles, grains and atoms can only react with forces directly applied to them, namely local driving forces, not to the global driving forces.

2.2.1.1 Energetic considerations

Sintering begins on porous powder compacts, considering of interparticle necks, that build later on grain boundaries, and free surfaces. The free energy decrease of both free surfaces and grain boundaries is referred to as global driving forces, which drives the densification process and grain growth. The following equation (Eq. 2-1) describes the free Gibbs energy G as a function of free enthalpy H and entropy S. System energy is reduced by total surface energy ($A_S\gamma_S$) decrease or total grain boundary energy ($A_{GB}\gamma_{GB}$) decrease. For example, during densification process, the free enthalpy decreases by decreasing free surface areas. Theoretically, the lowest global free energy is reached when powder compact turns into an almost dense single crystal. However, this condition is almost impossible to reach under conventional sintering conditions with limited sintering temperature and time, not to mention that powder distribution can be heterogeneous.

$$G = \Delta H - T\Delta S = A_S\gamma_S + A_{GB}\gamma_{GB} - T\Delta S \tag{2-1}$$

Lange [25] simulated the sintering process using an assembly of three particles, which is shown in Figure 2. The neck grows and free energy keeps decreasing until the contact angle $\varphi = \varphi_e$, where the system reaches a theoretical stable point with minimal free energy. Here, φ_e is called dihedral angle, and its value is related to the ratio between surface energy (γ_S) and grain boundary energy (γ_{GB}), as describes with Eq. 2-2.

$$2\cos\left(\frac{\varphi_e}{2}\right) = \frac{\gamma_{GB}}{\gamma_S} \tag{2-2}$$

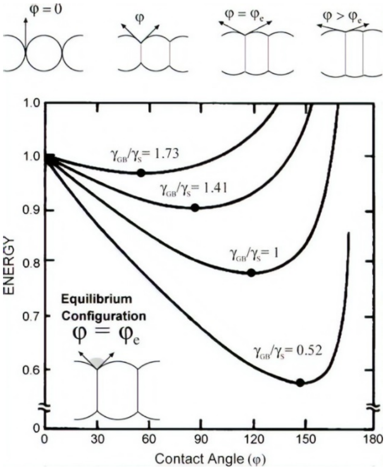

Figure 2: Energy change as a function of contact angle evolution for an assembly of three particles for different ratios between interfacial energies. The dots along the curves represent the minimum, i.e. the dihedral angle [7].

From another point of view, pore shrinkage also happens during sintering. Lange [25] used a model with circular arrays of cylinders or spheres and polyhedral arrays of spheres to calculate the free energy change as the function of the pore radius and the number of surrounding particles (Figure 3). The results lead to an important conclusion, that the pores will only shrink to the energetic-favorable state, $\varphi = \varphi_e$, but will not disappear. The lowest energy corresponds to a finite pore size, but not to zero. Wakai [26] also reached the same conclusion using a 3D numerical method by Surface Evolver, and the shrinkage of a pore was related to the sintering stress, which depended on the pore volume, the dihedral angle, as well as the pore coordination.

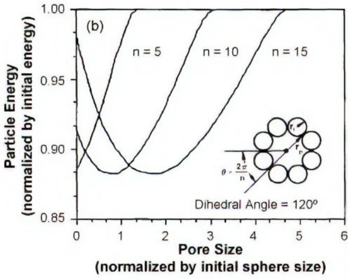

Figure 3: Normalized free energy of a ring array of spheres as a function of the pore radius normalized by the initial sphere size for ring arrays containing *n* number of spheres coordinating the pore [27].

In the case of spherical particles with the same sizes, once they reach the equilibrium state, the sintering process should cease upon thermodynamic considerations. However, real particles usually have faceted surfaces with different surface energies. Castro *et al.* [25] pointed out that in reality, faceted particles rotate to create new solid-solid surfaces, which continues the neck growth (Figure 4).

Castro *et al.* [25] also mentioned another phenomenon that breaks the balance: the movement of newly formed faces. Lange [27] drew the same conclusions but referred it to coarsening. These two description both relate to grain growth. Coarsening mainly happens between particles with distinct sizes, where the grain boundary moves towards the smaller particle until it disappears. Subsequently, a new contact forms and the neck growth continues (Figure 5). Coarsening offers an alternative approach to the decrease of system energy by reducing grain boundary areas, and thus hinder the densification process by lowering its driving force.

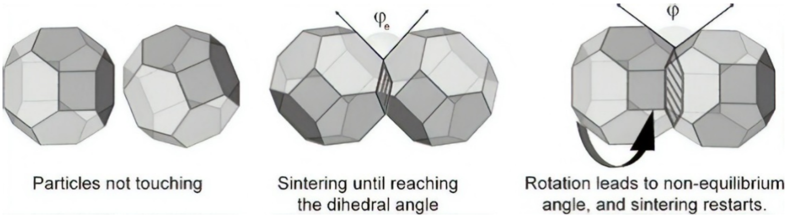

Figure 4: Schematic representation of the non-spherical particles being sintered. Different interface energies can lead to rotation or rearrangement of grains to decrease the total free energy [25].

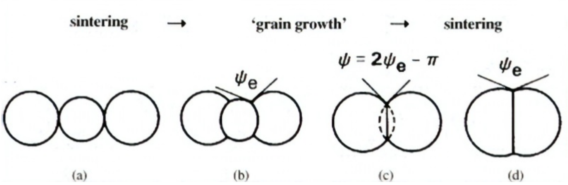

Figure 5: Sequential mass transport for two larger particles sandwiching smaller particle [27].

2.2.1.2 Local driving force

Sintering phenomena not only involves the thermodynamic global driving force, but also related to mass transport. Experimental results with fine-grain matrix and coarse-grain matrix [28-29] showed that densification in most cases is limited by kinetic considerations instead of thermodynamic considerations. Mass transport happens at the atom, grain and particle levels. The concentration gradient of atoms drives the movement of mass. In principle, it is the local driving force due to non-flat surfaces that renders atom concentration gradient.

As mentioned above, the movement of non-flat surfaces is ascribed to the local driving force, which is related to surface curvature. In the case of densification, which happens normally between particles with the same or similar size, the neck curvature leads to the force directly applied on the particles. By assuming the surface tension as the work required for the surface generation, a mathematical expression can be derived. As described by Laplace and Young, the tension, or Laplace pressure, is related to the particle radius and specific surface energy [1]:

$$\sigma = \gamma_s\left(\frac{1}{x} + \frac{1}{\rho}\right) \tag{2-3}$$

where x and ρ are the principal radii and σ is Laplace pressure. The radius of the concave surface is defined as negative while the radius of the convex surface is defined as positive. Thus, the neck surface is under tension, which drives the atoms on the neck region to move into the neck surface. Thereby the neck grows and the vertical distance between two particles decreases, which leads to the densification, as illustrated in Figure 6.

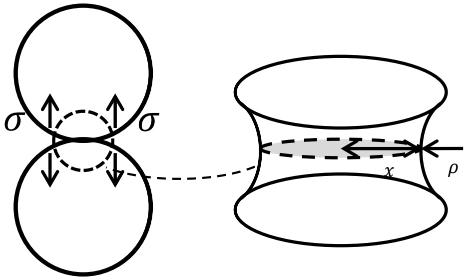

Figure 6: Illustration of tensile force induced by surface curvature in the neck region.

In the case of grain growth, the curved grain boundaries, between particles with different sizes, drive the directional movement. Grain growth can occur in both dense and porous polycrystalline solids [1]. The stress state induced by the non-flat grain boundaries favors the movement of atoms from concave positions to convex positions, and thus drives the movement of grain boundary to the concave side, as illustrated in Figure 7. This process leads to the growth of one grain at the expense of the other one.

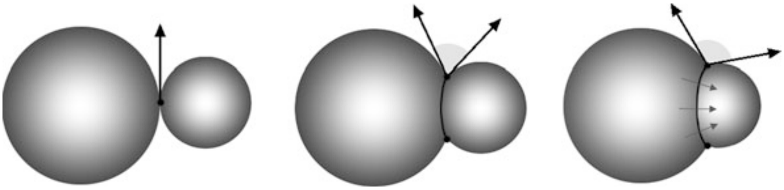

Figure 7: Illustration of grain boundary movement between two particles with different grain sizes [25].

Both sintering and grain growth require directional movements of atoms and the countermovements of vacancies under the curved surfaces. This atom movement is related to the concentration gradient, which is associated to the chemical potential difference. This chemical potential difference $\Delta\mu$ is strongly dependent on the stress states of the atoms, with a relation defined as follows [1,25]:

$$\Delta\mu = \sigma\Omega \tag{2-4}$$

where Ω is the atomic or molar volume, and the induced concentration difference of vacancies can be expressed as follows [1,25]:

$$c_v = c_{v0} \cdot \exp\left(\frac{\Delta\mu}{kT}\right) \tag{2-5}$$

where c_v is the concentration of vacancy under the curved surface, c_{v0} is the vacancy concentration without chemical potential gradient (under a flat surface). Take the densification as an example, vacancies diffuse to the neck region (grey area in Figure 6) and atoms diffuse to the neck surface, in this way, the neck growth happens.

2.2.1.3 Mass transport

Mass transport of solid state sintering involves three factors: source of the matter, transport path and sink of the matter. The sink of matter is always the same (inter-particle neck), while there exist six mechanisms differing in the sources of matter and in the transport path [1]: 1) from the surface through surface diffusion, 2) from surface through lattice diffusion, 3). from the surface through vapor transport, 4). from grain boundary through grain boundary diffusion, 5). from grain boundary through lattice diffusion, 6). from dislocation through lattice diffusion (Figure 8). Among the mechanisms above, only mechanisms 4-6 can efficiently decrease the distance between the two particles and are referred to as densifying mechanisms, while mechanisms 1-3 are non-densifying. However, all mechanisms can lead to neck growth. In other words, non-densifying mechanisms reduce the driving forces without increase of density. In order to obtain dense sintered body, it is important to suppress the non-densifying sintering mechanisms while promoting the densifying ones.

One option for densification is to increase the heating rate. The activation energy of surface related processes is lower than that of the processes related to grain boundary and bulk. Therefore, surface related processes happen at lower temperature. With a higher heating rate, the temperature regime, in which densifying mechanisms dominate, can be reached faster. In this way, the surface related processes can be suppressed.

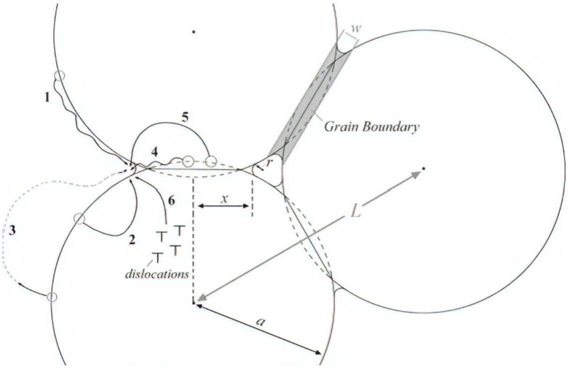

Figure 8: Illustration of the sintering mechanisms in ceramics for a three particle array. The numbers represent the different mechanisms. (1) surface diffusion (from surface); (2) Lattice diffusion (from surface); (3) evaporation/condensation (from surface); (4) boundary diffusion (from grain boundary); (5) lattice diffusion (from grain boundary) (6) lattice diffusion (from dislocations) [1].

2.2.2 Activation energy

As introduced above, the sintering process is very complex, involving microstructure evolutions activated by various mass transport processes. It is one of the ultimate objectives for sintering studies to define the dominating process and its corresponding activation energy. Rahaman *et al.* [1] concluded that the densification rate, $(1/\rho)(d\rho/dt)$, can be written in the following general form:

$$\frac{1}{\rho}\frac{d\rho}{dt} = \frac{3}{L}\frac{dL}{dt} = \frac{AD}{d^m kT}\left(P_a\phi + \frac{\alpha\gamma_s}{r}\right) \tag{2-6}$$

where $(1/L)(dL/dt)$ is the linear shrinkage rate (assuming here isotropic sintering with the same shrinkage rate in all directions), A is a constant, D is the diffusion constant, d is the grain size, m is an integer depending on the diffusion mechanism ($m = 2$ for lattice diffusion and $m = 3$ for grain boundary diffusion), $\alpha\gamma_s/r$ is the sintering stress with α representing the geometrical constant that depends on the shape of the pore, P_a is the external applied stress and ϕ is the stress intensification factor to relate the external applied stress to the internal stress on the grain boundary. The stress intensification factor depends on the pore structure. In the case of spherical pores randomly distributed in the matrix, the stress intensification factor can be easily described as follows [1]:

$$\phi = \frac{1}{1-P} = \frac{1}{\rho} \tag{2-7}$$

with the porosity P. The coefficient of diffusion, D, is temperature dependent, and can be written as follows:

$$D = D_0 exp\,(-\frac{Q_A}{kT}) \tag{2-8}$$

with D_0 representing the diffusion constant and Q_A as the activation energy for the corresponding densification process. By combining Eq. 2-6 and Eq. 2-8, the activation energy can be obtained through the following relationship:

$$ln\left(T\frac{1}{\bar{\rho}}\frac{d\bar{\rho}}{dt}\right) \propto -\frac{Q_A}{T} \tag{2-9}$$

Wang and Raj [30] proposed a constant heating rate approach to determine the activation energy. The Master sintering curve approach [31] is also a common method involving with the experiments using different heating rates. But as the whole thermal cycle is considered, an effective value is measured [32], which often does not correspond to a single mechanism. Langer *et al.* [33] calculated the activation energy at the isothermal period during the sintering. It is noteworthy mentioning that Eq. 2-9 requires the grain size to be constant for the comparison of sintering activation energies under difference conditions.

2.3 Continuum mechanical description of sintering

The discussion of sintering was at first based on the concept of discrete particles in order to understand the analytical description of a few idealized grains [1]. In order to generalize and decide the macroscopical changes of the geometry of a powder compact [34], continuum mechanics is the most promising method. Macroscopic factors considered here include external loadings, density gradient, geometrical condition and so on. The introduction of continuum mechanics of sintering is organized as follows: in Section 2.3.1, the fundamental continuum formulas are represented, and in Section 2.3.2, sintering parameters are introduced.

2.3.1 Theory

It is assumed that the material is isotropic and the sintering mechanism is not modified by the applied stress. This fits well with the low pressure experiments conducted in this work, where the applied stress is in the range of the sintering stress [35]. However, if the electric field changes the sintering mechanism, the following constitutive equations may not be applied anymore. Additionally, it is assumed that the material response to external stresses is viscoelastic, that is to say, the sintered compact at first shows an instantaneous elastic strain, and then a continuous deformation during sintering [34,36], as illustrated in Figure 9. The major problem involved is that the modulus and the viscosity of the compacts are not constant but time dependent: as the porosity decreases, the modulus and viscosity increase. In this case, the Laplace transform does not yield a reasonable result on the base of the Maxwell model [36]. In order to solve this problem, Raj *et al.* [37] assumed that the moduli are constant, and Bordia *et al.* [36] proposed that it is reasonable to derive constitutive equations considering pure viscous deformation, since the elastic strain is negligible compared to the densification. This assumption is also supported by the experimental results from Cai *et al.* [38].

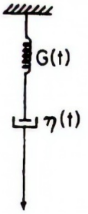

Figure 9: Maxwell model with the modulus G and viscosity η [36].

The constitutive relationship between the normal stress components (σ_1, σ_2, σ_3) and strain rates ($\dot{\varepsilon}_1$, $\dot{\varepsilon}_2$, $\dot{\varepsilon}_3$) can be written as:

$$\dot{\varepsilon}_i = \dot{\varepsilon}_f + \frac{1}{E_p}\left[\sigma_i - \upsilon_p \sum_{j=1}^{3}(1-\delta_{ij})\sigma_j\right] \tag{2-10}$$

with the direction index i=1..3, Kronecker δ_{ij}, υ_p the viscous Poisson's ratio and E_p is the uniaxial viscosity. These equations are analogous to Hooke's law for linear elastic, isotropic continua, with strain rate replacing strain and the addition of the intrinsic free sintering strain rate, $\dot{\varepsilon}_f$. In the case of the cylindrical coordinates, the equations can be thus written as follows [39]:

$$\dot{\epsilon}_r = \dot{\epsilon}_f + \frac{1}{E_p}\left[\sigma_r - \upsilon_p(\sigma_\theta + \sigma_z)\right] \tag{2-11}$$

$$\dot{\epsilon}_z = \dot{\epsilon}_f + \frac{1}{E_p}\left[\sigma_z - \upsilon_p(\sigma_\theta + \sigma_r)\right] \tag{2-12}$$

where σ_r, σ_z and σ_θ are the stress components along the principal axes, $\dot{\epsilon}_f$ the free strain rate without any constraints. In the case of uniaxial stress applied along the z axis of a cylindrical sample, Eq. 2-11 and 2-12 reduce to:

$$\dot{\epsilon}_r = \dot{\epsilon}_f - \frac{\upsilon_p}{E_p}\sigma_z \tag{2-13}$$

$$\dot{\epsilon}_z = \dot{\epsilon}_f + \frac{1}{E_p}\sigma_z \tag{2-14}$$

2.3.2 Sintering parameters

For a linear viscous material, traditionally five sintering parameters are defined: the uniaxial viscosity (E_p), the viscous Poisson's ratio (υ_p), the shear viscosity (G_p), the bulk viscosity (K_p) and the uniaxial sintering stress (σ_z^s). These parameters depend on the temperature (except for υ_p) and the microstructure (especially grain size and relative density). In addition, these parameters are associated with each other: the uniaxial viscosity and the viscous Poisson's ration can be expressed as the function of the bulk viscosity and the shear viscosity. The sintering stress is an equivalent intrinsic stress, which is also related to the free shrinkage rate without any external stress. The theoretical models for the expressions of the sintering parameters are broadly classified into phenomenological and micromechanical models [40]. Bordia and Scherer [36] performed a comparison of several models. Later, Olevsky [34] gave a detailed review of the application of the models from discrete to continuum theory.

The micromechanical models are based on a representative volume element, in terms of pores and solid body skeleton. Mackenzie and Shuttleworth [41] described the sintering as a uniform compression of a spherical shell model, and derived the expression of the bulk viscosity and the shear viscosity as a function of porosity. Scherer *et al.* [42-43] elaborated a method to express the uniaxial viscosity and the viscous Poisson's ratio as the function of relative density based on the viscous sintering of glass materials with the cylindrical shaped powder particles. Skorohod *et al.* [44-45] suggested the expression for effective shear and bulk viscosities as a function of porosity on the base of generalized-viscous flow body. Other models, such as those proposed by McMeeking and Kuhn [46], Cocks [47] and Riedel *et al.* [48-49], took the stages of sintering into consideration. However, all the above models concentrated on the model of a simple, different regular arrangement of pores and isotropic powder packing structures.

Besides the above-mentioned analytical models, an effective experimental approach to determine the sintering parameters as a function of relative density was also developed, namely the loading-dilatometry technique. How to use this technique in the measurement of the sintering parameters is discussed in section 3.4.2. Phenomenological models were derived from this empirical approach, and were proposed by Rahaman *et al.* [50], Raj and Venkatachari [51] and Hsueh *et al.* [39]. The detailed discussion about the above models is presented in the following corresponding part.

2.3.2.1 Uniaxial viscosity

The uniaxial viscosity can be experimentally determined from the slope of the uniaxial strain rate – stress curve. The uniaxial viscosity derived from Eq. 2-14, in the case of the uniaxial loading, is expressed as follows:

$$E_p = \frac{\sigma_z}{\dot{\epsilon}_z - \dot{\epsilon}_f} \tag{2-15}$$

The increase of the uniaxial viscosity is a result of both grain growth and relative density increase. Experiments for the measurements of uniaxial viscosity includes the measurements on alumina [35], gadolinia doped ceria [52], low temperature co-fired ceramics (LTCC) [53] and calcium aluminosilicate (CAS) glass [54]. As illustrated in Figure 10, the experimental results showed the same trend in general: the viscosity increases quasi-linearly and remains low until about 85 to ~ 90 % relative density due to the sintering of investigated material and then increases strongly due to grain growth [35]. In contrast, the increase in viscosity for the LTCC material and CAS glass is less drastic, in particular for the CAS glass material, as the contribution of grain growth does not exist in this case [64]. But if crystallization takes place, this will change the viscosity dramatically and crystallization control is an important issue in the design of LTCC materials.

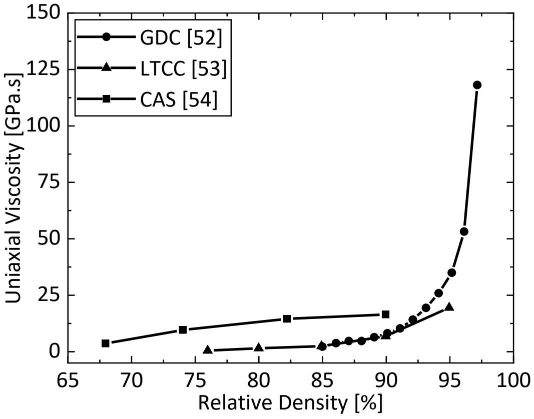

Figure 10: Uniaxial viscosity GDC at 1100 °C [52], LTCC at 840 °C [53] and CAS at 850 °C [54].

In the case of polycrystalline materials, the uniaxial viscosity at a constant temperature can be expressed in the following general form [55]:

$$E_p = E_{p0} \times E_{p1}(\bar{\rho}) \times E_{p2}(d) \times E_{p3}(T) \tag{2-16}$$

where E_{p0} is a scaling factor, E_{p1}, E_{p2} and E_{p3} are functions of relative density $\bar{\rho}$, grain size d and temperature T, respectively. As viscosity decreases with increasing temperature, function E_{p3} is based on the activation energy of the dominant matter transport mechanism and can be expressed as follows:

$$E_{p3}(T) = exp\left(\frac{Q_{E_p}}{RT}\right) \tag{2-17}$$

The increase of relative load bearing area is expressed as the function of E_{p1} and the grain growth is taken into consideration in the function of E_{p2}. Semi-empirical models were generated on the base of different experimental results. Rahaman's model [25] was derived by combining Coble's creep mechanism [25,78], i.e. grain boundary diffusion, and Beere's [79-80] calculation of the stress intensification factor, Φ, considering a more complicated geometry of pores in the microstructure. The derived following equation for the uniaxial viscosity [25]:

$$E_p = E_{p0} \times E_{p1}(\rho) \times E_{p2}(d) = A \times \bar{\rho}\frac{exp\,[-3a(1-\bar{\rho})]}{3\,exp[-a(1-\bar{\rho})]+exp\,[-2a(1-\bar{\rho})]} \times d^3 \tag{2-18}$$

where A is a scaling factor, d is the grain size, $\bar{\rho}$ is the relative density and a is a parameter related to the dihedral angle.

2.3.2.2 Bulk and shear viscosity

Besides uniaxial viscosity, bulk and shear viscosity are essential under the frame of continuum mechanics. The relationship between volumetric densification rate, $\dot{\epsilon}_v$, and the driving force can be expressed as follows:

$$\dot{\epsilon}_v = 2\dot{\epsilon}_r + \dot{\epsilon}_z = \frac{1}{K_p}\left(\frac{\sigma_z}{3} + \Sigma\right) \tag{2-19}$$

where K_p is the bulk viscosity and the driving force consists of two parts: Σ, the sintering potential and σ_z, the external applied stress. Because the sintering potential is related to the free shrinkage rates without any constraints, Eq. 2-19 can be expressed as follows:

$$\dot{\epsilon}_v = 3\dot{\epsilon}_v^f + \frac{1}{K_p}\frac{\sigma_z}{3} \tag{2-20}$$

Similar to the determination of uniaxial viscosity [52], the bulk viscosity can then be obtained through the inverse of the slope of the plot $\dot{\epsilon}_v$ vs. $\frac{\sigma_z}{3}$. By analogy to bulk moduli for an isotropic material [36], bulk viscosity can be expressed as follows:

$$K_p = \frac{E_p}{3(1-2\upsilon_p)} \tag{2-21}$$

Subsequently, the shear viscosity, G_p, can be expressed in terms of uniaxial viscosity and bulk viscosity as follows:

$$G_p = \frac{3E_pK_p}{3K_p - E_p} \tag{2-22}$$

The shear viscosity, G_p, can also be calculated according to the following relationship from Eq.2-21 and Eq. 2-22 :

$$G_p = \frac{E_p}{2(1+\upsilon_p)} \tag{2-23}$$

Different models has been proposed to represent bulk and shear viscosities. Hsueh *et al.* [39] assumed that the uniaxial viscosity depend on the instantaneous grain size and density. They expressed the shear viscosity and bulk viscosity as follows, respectively:

$$G_p = G_p^0 \times \bar{\rho}^p \times (1-\bar{\rho})^{-\lambda} \tag{2-24}$$

$$K_p = -K_p^0 \times \frac{\bar{\rho} \times (1-\bar{\rho})^{\lambda}}{(1-\bar{\rho})^{1+\lambda}} \tag{2-25}$$

where G_p^0 and K_p^0 are the initial shear viscosity and initial bulk viscosity, respectively. λ and p are both the fitting parameters. p gives the dependence on density assuming the same grain size, while λ related to the grain growth during sintering.

Raj and Venkatachari model [51] was also generated on the base of Coble's creep mechanism, and the load bearing area was assumed to be proportional to the relative density. The expression for bulk and shear viscosity were derived as follows:

$$G_p = G_p^0 \times d^3 \times \bar{\rho} \tag{2-26}$$

$$K_p = K_p^0 \times d^3 \times \frac{1}{\bar{\rho}}[ln(1-\bar{\rho}) + 0.5\bar{\rho}(\bar{\rho}+2)] \tag{2-27}$$

2.3.2.3 Viscous Poisson's ratio

The Viscous Poisson's ratio represents an important sintering parameter, especially for constrained sintering [53,56]. According to Eq. 2-11 and Eq. 2-12, the viscous Poisson's ratio can be described as follows:

$$\upsilon_p = \frac{\dot{\epsilon_f} - \dot{\epsilon_r}}{\dot{\epsilon_z} - \dot{\epsilon_f}} \tag{2-28}$$

This experimental approach to obtain uniaxial Poisson's ratio is challenging since it involves the subtraction of two measured small rates. With this in mind, a more robust approach was developed to obtain the viscous Poisson’s ratio, as shown for low temperature cofired ceramics (LTCC) materials [56]. Together with the uniaxial viscosity E_p and bulk viscosity K_p, the viscous Poisson’s ratio can be calculated according to the following equation:

$$\upsilon_p = \frac{3K_p - E_p}{6K_p} \tag{2-29}$$

On the other hand, the above deduction also implies that the viscous Poisson’s ratio, υ_p, is related to both bulk viscosity and shear viscosity under constant temperature as follows [57]:

$$\upsilon_p = \frac{3K_p - 2G_p}{2(3K_p + G_p)} \tag{2-30}$$

Bordia and Scherer [36,57] compared several models describing the viscous Poisson’s ratio and pointed out that it depends only on the relative density under a constant temperature, due to the same dependency of bulk and shear viscosity on the grain size. However, the overestimation of shear viscosity according to Hsueh’ model renders a negative viscous Poisson’s ratio in contradiction to the thermodynamic theory and experimental data [39]. Uniaxial viscous Poisson’s ratio exhibits a close to linear dependence on relative density, ranging from about 0.1 at green density to 0.5 at 100 % of theoretical density, as shown by Zuo *et al.* [35,58] for alumina, Okuma *et al.* [54] for calcium aluminosilicate (CAS) glass and Salamone *et al.* [59] for $YBa_2Cu_3O_{6+x}$. The most accepted technique used to determine the viscous Poisson’s ratio is called discontinuous loading-dilatometry technique [35,53]. It offers not only an accurate measurement of axial strain rate as well as radial strain rate, but can also alleviate the anisotropic effect brought by the application of uniaxial load. Zuo *et al.* [58] compared his results with several theoretical models designed for the prediction of the viscous Poisson’s ratio, and found out that it fitted well with semi-empirical models, such as Rahaman’s model [50] as well as Venkatachari and Raj’s model [51].

However, Wakai *et al.* [60] pointed out the lack of underlying physics of these models due to not taking into account grain boundary sliding. Riedel *et al.* [49] developed a method to estimate bulk and shear viscosities of isotropic porous materials from the knowledge of microstructure. The densification process is related to the microscopic motion of individual particles. The normal velocity vector to the grain boundary is proportional to the grain boundary diffusion coefficient, while the tangential velocity is linked to the microscopic viscosity. Kraft and Riedel [61] related bulk and shear viscosities to grain boundary, bulk and surface diffusion in simulating solid state sintering process. Wakai *et al.* [60] analyzed how the shear viscosity and the viscous Poisson’s ratio depend on grain boundary sliding, local structure, and relative density. When grain boundary diffusion is the dominating mechanism during sintering, the bulk viscosity depends on the grain boundary diffusion coefficient, and the shear viscosity depends on both the grain boundary diffusion coefficient and grain boundary sliding, which is characterized by the non-dimensional viscosity, η^*:

$$\eta^* = \eta \frac{\Omega \delta D_{gb}}{kTr^2} \tag{2-31}$$

where η is the microscopic viscosity, δ is the grain boundary thickness, D_{gb} is the grain boundary diffusion coefficient, T is the temperature, Ω is the atomic volume and r is the particle radius [60].

The macroscopic response of material during sintering under external stress dependents on η^*, a combination of microscopic viscosity and grain boundary diffusion coefficient. In addition, the non-dimensional viscosity, η^* is not a material constant but a parameter relating to the microstructural evolution during sintering. On the base of the above theory, Wakai *et al.* [60] concluded that viscous Poisson's ratio decreased with increasing coordination number, ratio of grain boundary energy to surface energy as well as non-dimensional viscosity.

2.3.2.4 Sintering stress

The hydrostatic sintering stress or sintering potential Σ, as driving force for the densification, is related to the grain size, pore size, surface energy and grain boundary energy [62]. The sintering stress is a mathematical concept, which is the equivalent externally applied compressive stress that causes the same effect during free sintering as the surface energy of pores and grain boundaries [24,36].

The analytical formulation of sintering stress renders difficulties considering the complex of the microstructure, and thus requires simplification. Take the final stage of sintering of polycrystalline system as an example, if the pores are assumed to have a quasi-equilibrium shape and the grains are nearly spherical, the hydrostatic sintering stress is expressed as follows: [62]:

$$\Sigma = \Omega \left(\frac{2\gamma_{GB}}{d} + \frac{2\gamma_S}{r} \right) \tag{2-32}$$

where d is the grain size, r is the radius of pores. γ_{GB} and γ_S is the grain boundary energy and the specific surface energy, respectively.

The hydrostatic sintering stress describes the mechanical stress necessary to stop the porous solid shrinking while the uniaxial sintering stress describes the stress needed to stop the shrinkage on only one direction. The relationship between sintering potential Σ and uniaxial sintering stress, σ_z^s, can be expressed as [35]:

$$\Sigma = \frac{\sigma_z^s}{1 - \upsilon_p} \tag{2-33}$$

In other words, the reduced free energy during the sintering can be set equal to the work done by the uniaxial sintering stress in reducing the height of the sintering compact. This means that the densification in the axial direction stops, when the uniaxial stress that is similar to that of the sintering stress is applied. The uniaxial sintering stress can be experimentally determined by the extrapolation of the linear relation between uniaxial strain rate vs. uniaxial stress until the uniaxial strain rate equals to zero [57], which can be described as follows:

$$\sigma_z^s = -\dot{\epsilon}_f E_p \tag{2-34}$$

The magnitude of the uniaxial sintering stress varies among material systems from around 0.1 MPa for low temperature co-fired ceramics (LTCC) [53] and calcium aluminosilicate (CAS) glass [54], to a few MPa for submicron alumina [35], until up to 100 MPa in nanocrystalline zirconia [63-64]. As illustrated in Figure 11, the absolute value of the sintering stress increases during the intermediate stage of sintering and then starts to decrease on the transition from intermediate sintering to the final stage of sintering. However, agglomerates and inhomogeneities in powder compacts shift the beginning of the grain growth to relative densities lower than 90 % and thus can affect the viscosity/sintering stress-density relationship [63].

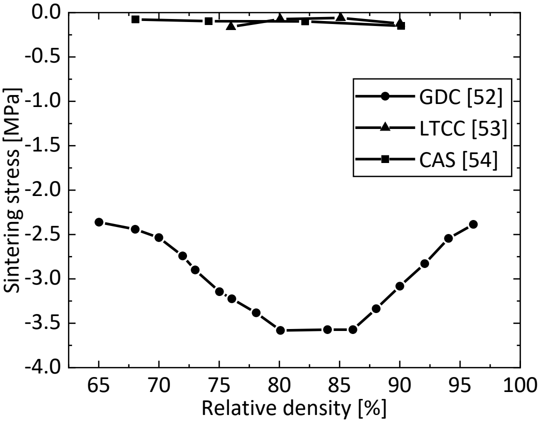

Figure 11: Sintering stress of alumina [35], LTCC at 840 °C [53] and CAS at 850 °C [54].

2.4 Field assisted sintering

As introduced before, conventional sintering requires a significant amount of energy to form products with desired properties out of ceramic powder compacts. In order to reduce this required energy, as well as to target unique properties required for applications, different approaches have been applied, including the usage of electric fields [2-4]. The application of external electrical fields can be basically divided into two groups: high voltage and low voltage consolidation [65-66]. The usage of low voltage, together with high current density, is referred to as the field assisted sintering/spark plasma sintering technique (FAST/SPS) [2,4]. Grasso *et al.* [67] emphasized a subgroup belong to FAST/SPS named electric current activated/assisted sintering (ECAS), which used pulsed ac or dc while sintering. One special example of the application of high voltage refers to as flash sintering, during which the densification occurs within a few seconds [3,12]. Flash sintering was firstly reported in 2010 by Cologna *et al.* with yttria-stabilized zirconia [12].

2.4.1 Material and applications

Field-assisted sintering provides opportunities for the usage of materials that once showed difficulties in industry application. The usage of this technique can be divided into the following directions [4]: the reduction of sintering temperature, the achievement of targeted properties and accelerated phase formation.

1. The reduction of sintering temperatures
    a. High melting temperature materials, for example refractory metals or the ultra-high temperature ceramics. These materials possess outstanding mechanical, thermal and electrical properties. The main problem in sintering this kind of material is the rapid grain growth when a high relative density (higher than 95 %) is required. Therefore, the use of FAST/SPS technique offers the opportunity for a fast densification under a much lower furnace temperature.
    b. Materials for energy applications. Both solid-state batteries and solid oxide fuel cells (SOFC) have received increasing attention, because of their safety advantages as well as their high power densities [68]. For SOFCs, field assisted sintering provides the possibility of fabricating the electrolyte and electrodes with improved solid-solid interface properties, as well as with higher density [69-71]. Francis *et al.* [72] reported the application of flash sintering on manufacturing anode–electrolyte multilayers. For solid-state batteries, the application of field assisted sintering is also aiming to avoid undesirable reactions during co-firing and thereby improving the performance of battery [73-75].
2. The achievement of targeted properties. Optical and mechanical properties are taken as examples.
    a. Optical properties: Transparent ceramics, as an example, have a wide range of application in the areas of laser hosts, infrared (IR) windows/domes, lamp envelopes and transparent armors [76]. High heating rate together with the shorter time provided by the FAST/SPS ensure a finer grain size [77].

   b. Mechanical properties: The mechanical properties can be improved by lowering the grain size, as in the application of nanostructured materials. During conventional sintering, however, powder with small particle size is inclined to coarsen, leading to a larger grain size than desired. Field assisted sintering advances in a shorter holding time and higher heating rate for achieving the same relative density. Therefore, small grain sizes can be achieved.

3. Accelerated phase formation. Theories have been promoted that electrical fields act as a second driving force in addition to the chemical gradient for the movement of ions [78]. The acceleration of the transformation of ion across the boundaries is mostly amplified through the electrical fields [79-80]. This has been applied in t solid-state reactive synthesis [81-82] as well as the field assisted soldering [80,83]. The application goes on with functional materials as well as the non-equilibrium materials [4].

2.4.2 Possible mechanisms

Though the concept of applying a current to sinter powder compacts has already been used before, a clear understanding of mechanisms involved in field assisted sintering is still missing. The field assisted sintering was previously referred to spark plasma sintering. However, the evidence of formation of plasma is insufficient [25]. In order to understand the effect of electrical fields during the sintering, several mechanisms have been proposed. As introduced before, sintering itself, without electrical fields, already involves several processes taking place at the same time. Thus, not a single mechanism should be expected to describe field assisted sintering. A combination of different phenomena seems to be a more reasonable approach, with one of them dominating for a given material at a certain condition (temperature, electrical field strength, current density and so on.). In the following section, different possible mechanisms are discussed.

2.4.2.1 Macroscopic Joule heating

Electrical current through the specimen leads to temperature increase, which is named as Joule heating effect. This temperature increase is the most direct effect of field with contacting electrodes. In the case of FAST/SPS, specimens are sintered inside the graphite tool (see Figure 12). For ceramic systems where high-electric currents flow directly through the green body rather than through the surrounding (graphite) tools, the higher current density through the specimen can then cause significant Joule heating. One important example is flash sintering, which happens under a certain electrical field above a given temperature, at which conductivity reaches a threshold. During the flash sintering, the densification occurs within a few seconds [3,12].

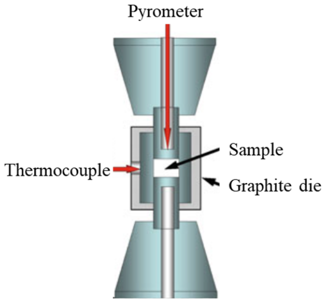

Figure 12: Schematics of FAST/SPS set-up [6].

The thermal runaway model has successfully predicted the critical threshold of the electrical field as a function of the furnace temperature to trigger flash sintering [14-17]. According to this model, the Joule heating, especially the macroscopic bulk Joule heating, is considered to be the main reason for the onset of flash sintering. In this work, the thermal runaway model developed by Pereira da Silva *et al.* [17] was applied for the onset prediction, in which the flash sintering event happens when there is a discontinuity in the equilibrium surface of the stable sample temperatures caused by the heat balance between Joule heating and the heat losses [84]:

$$\frac{E^2 e^{-\frac{\Delta E}{k\theta}}}{\Omega_0} - h(\theta - \theta_0) = 0 \tag{2-35}$$

where E is the electrical field, ΔE is the activation energy for resistivity. In this simulation, the resistivity was measured by Impedance Spectroscopy. k is the Boltzmann constant, θ is the sample temperature,Ω_0 is the pre-exponential constant for resistivity, h is the heat transfer coefficient for convention and θ is the furnace temperature.

Direct evidence for macroscopic Joule heating effect has been provided using *in situ* energy dispersive x-ray diffraction (EDXRD) of TiO_2 [85] and Ceria [86] in the steady state of flash sintering. In both cases, the true sample temperatures, determined from the calibration of the unit cell expansion, were higher than furnace temperatures due to Joule heating effect and were comparable to the respective specimen temperatures during conventional sintering, which were the same as the furnace temperature.

The effect of Joule heating in improving densification is correlated not only to improved specimen temperature but also to fast heating rate,. In the case of FAST/SPS (Figure 6), for materials with a significantly lower electrical conductivity than the graphite tool, the comparison with hot pressing under the same conditions shown that there is no direct effect of the electrical fields, as evidenced for alumina [5] and fully stabilized zirconia [6]. The improvement in the sintering behavior was attributed to the mechanical compressive load and the high heating rates involved. The high heating rate can promote the densification according to two assumptions. Firstly, since the temperature dependence of activation energy of non-densify process and densify process is often different, densification is more favored at high temperature while surface diffusion is more favored at low temperature (Figure 13). Take the flash sintering as an example, the temperature surge corresponds to a much higher heating rate compared to conventional sintering. High heating rate is beneficial by avoiding long dwelling time in the low temperature range where non-densify process happens more easily.

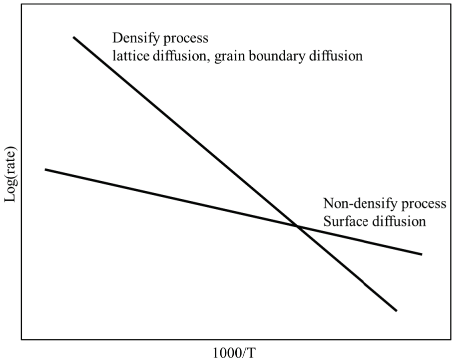

Figure 13: the sketch of the densification/coarsening rate on the dependence of temperature.

Secondly, an increase in grain boundary and bulk conductivity of flash sintered samples compared to conventionally sintered specimens was observed with *ex-situ* impedance spectroscopy [87-88]. The difference is attributed to defect accumulation on the grain boundary which promotes the ion migration during the sintering. The defect accumulation was kept during the cooling and thus influence conductivity of the grain boundary of the specimen. The high heating rate during the flash sintering leads to the formation of this ‘non-equilibrium grain boundary’ because no time is allowed for the relaxation [89]. However, direct evidence is still missing, considering the limitation of impedance spectroscopy in the conductivity measurement under high temperature.

At the same time, experimental results showed that a material can also undergo an instantaneous densification process, similar to flash sintering, as proved by Meng *et al.* [18,90] used the exothermic reaction between Ni and Al powders as the thermal source. The results showed that alumina can be sintered within 2 min under a heating rate of 1873 K/min, moreover, a difference in grain boundary microstructure was also observed [91]. This significant improvement in sintering without electrical fields emphasizes the role of rapid heating behavior during field assisted sintering [89].

2.4.2.2 Microscopic Joule heating

Unlike macroscopic Joule heating effect describing increase of specimen temperature, the microscopic Joule heating is based on the preferential Joule heating at microscopic scale, such as particle necks, grain boundaries and so on. The Grain boundaries as a fast migration path for ions play a significant role in sintering. They exhibit different properties compared to the bulk, such as ionic and electronic conductivities as well as a different atomic structure, the so-called space charge layer, in the case of ceramics with doping elements with a different valence. The space charge layer is formed in the direct vicinity of the grain boundary in response to a non-zero charge due to charged defects segregation. The width of the space charge layer, also called Debye layer, can be calculated using the following equation:

$$L_D = \sqrt{\frac{\varepsilon' \varepsilon_0 kT}{2e^2 u_{acc}^2 c_{acc,\infty}}} \tag{2-36}$$

where ε' is the relative dielectric constant of the ceramic, ε_0 is the permittivity, e is the charge of an electron, $u_{acc}$is the charge number of the species that is accumulated in the space charge layer, and $\mathrm{c}_{\mathrm{acc},\infty}$ is its concentration far away from the grain boundary. The Debye layer can be several tens of nanometers thick [92], while thickness of the grain boundary region is 0.5–1 nm indicated by high-resolution transmission electron microscopy[1]. Considering the small thickness of the pace charge layer, the intrinsic electrical field in the Debye layer can be comparable or larger than the external applied field. In addition, the existence of space charge layers has been experimentally confirmed [93-94]. However, it is worth noting that present theories calculating space charge layer's potential or thickness are based on the Mott-Schottky profiles, which are only valid with the dilute concentration [95-97]. In summary, the space charge layer is assumed to act as a blocking layer for the ion transfer trespassing the grain boundaries due to low local oxygen vacancy concentration [98], which may in turn cause a higher temperature in the grain boundary.

Local Joule heating effects are also one of the mechanisms for fields assisted sintering. Indirect experimental evidence has been found as the proof for the local Joule heating effect in both metal [99] and ceramic systems [100-102] in flash sintering experiments, by attributing the differences in grain boundary microstructures (*ex situ* observations) to the localized high temperature during sintering. The same evidence has also been found in the case of FAST/SPS by the work of Schwesig [9] on nanocrystalline silicon, where density fluctuations in the microstructure were used as an indication of the existence of a microscopic temperature gradient. However, the authors attribute this fluctuation not to microscopic temperature gradient on grain boundaries but to the percolation effects, which basically described the formation of percolating current paths inside the green body due to the intrinsic inhomogeneity of powder compacts [4].

Along with experiments, simulation works have also been performed for a comprehensive understanding. Vikrant *et al.* [103] simulated the possible start of flash sintering on the base of local Joule heating introduced by the high grain boundary resistance on the base of space charge layer theory under DC fields. However, Holland *et al.* [104] performed the numerical simulation of mixed or ionically conducting ceramics at particle necks, and pointed out that there is no significant contribution to a better densification behavior of high temperature gradients induced by high current flow of 10^4 A/m^2 and they were limited to a few degrees (smaller than 10 K of particle with 100 nm diameter). This is due to the small particle size, which levels out the temperature gradient. The similar conclusion has been drawn by Semenow *et al.* [105] via a metal system with thermo-electro-mechanical modeling even with ten times higher electrical loading than a typical FAST/SPS condition, considering the high thermal conductivity of metal.

Biesuz and Sglavo [3] pointed out that current density or electrical fields used in the above simulations is quite low compared to flash sintering, therefore additional effects, which may increase the local temperature gradient, should also been taken into account, for example, 1) rapid release of surface enthalpy leading to an additional overheating at the grain boundary [3]. 2) highly localized electrical fields appears in the area of geometry of neck due to the short distance between two particles. According to the simulation of Holland *et al.* [106], the local field strengths can be higher than the applied external field by a factor of about 180 for materials with a dielectric coefficient of 30. Therefore, it is reasonable to propose the possible interaction between the external applied field and the intrinsic electric field in space charge layer. Jeong *et al.* [107] proposed the assumption of the shift of migration energy barrier (Figure 14), and confirmed this assumption by experiments with alumina. As proposed by the authors, the positively charged grain boundary lowers the activation energy for anion while increases the activation energy for cation (Figure 14a). A positive bias on the small grain side exerts an opposite effects on the cation migration, while a negative effect on the anion migration (Figure 14b).

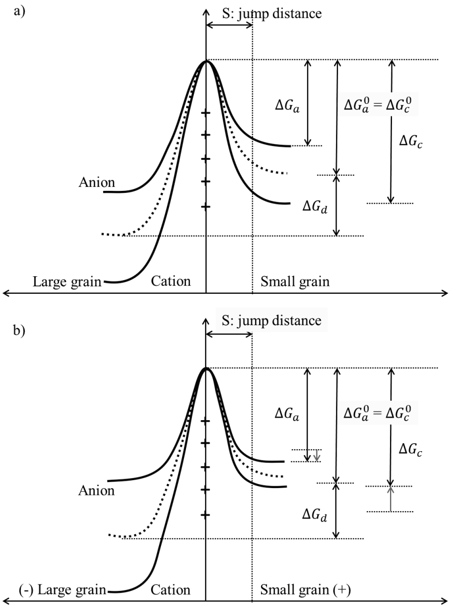

Figure 14: Schematic illustrations of (a) the effect of the space charge on the activation energy for an ion jump, and (b) the effect of external electrical fields on the activation energy for ions jumping across the boundary, denoted as red arrows [107].

This temperature increase near the grain boundary is also assumed to be the reason for a slow grain growth, i.e. grain boundary mobility [12,92]. Ghosh *et al.* [92] gave an explanation based on a thermodynamic argument, relating the grain boundary energy, γ_{GB}, to a Gibbs free energy quantity given by:

$$\gamma_{GB} = \Delta H_{GB} - T\Delta S_{GB} \tag{2-37}$$

where ΔH_{GB} and ΔS_{GB} are the excess of enthalpy and entropy, respectively, associated with the grain boundary. The entropy part decreases as the temperature increases, moreover, the $T\Delta S_{GB}$ parts increases, and lead to the decrease of the grain boundary energy, γ_{GB}. Therefore, the local temperature increases and creates a potential well for grain boundary mobility (Figure 15). However, if the field reaches a certain point, the high grain boundary movability will exceed this thermodynamic pinning effect, since larger grain size has been observed with higher electrical fields in experiments [87].

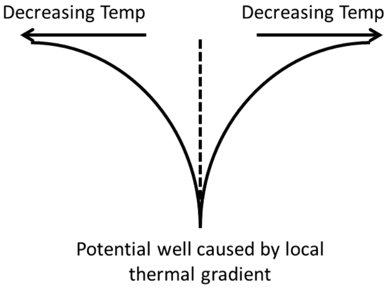

Figure 15: Electrical boundary resistance can increase the local temperature of the boundary, producing a spatial minimum in its energy [92].

2.4.2.3 Field induced defects

Sintering as well as grain growth involves mass diffusion, and defects are essential pathways in the solid state in order to allow diffusion. In ionic materials, a single charged vacancy cannot exist by itself because of the constraint of charge neutrality. Therefore, either a Frenkel defect, a pair of a vacancy and an interstitial site, or a Schottky defect, a pair of anion vacancy and cation vacancy, is generated. The concentration of defects is known in thermodynamic equilibrium with temperature and the level of doping level. But the effect of electrical field on the defect chemistry is still under debate.

Further experiments showed that the onset temperature of flash sintering was approaching a lower limit of Debye temperature, which is claimed to be the threshold for the possible thermal activated lattice vibration in an equilibrated crystal [108-109]. Doubts have been aroused, since the atomistic simulations have shown that the electric field strength required to generate anti-Frenkel pairs (oxygen vacancies and oxygen interstitials) is beyond practical relevance. For example, the required electrical field strength for monoclinic and cubic HfO_2 was found to be about 0.1 GV/cm, that is to apply 10^7 V to a 1 mm thick sample [21]. This value is beyond the dielectric strength of the materials, and far higher than the field strengths used so far in flash sintering experiments. However, Jongmanns *et al.* [110] performed the molecular dynamics (MD) simulations of an aluminum single crystal with a free surface. Only at temperatures above Debye temperature, the non-equilibrium excitation of lattice vibration will not decay but lead to the generation of crystal defects. Besides Debye temperature, two other conditions need to be fulfilled: 1) the lattice vibration mode should lie close to the Brillouin zone edge; 2) the excitation rate should be sufficiently high. The author argued that his calculation is based on the non-equilibrium phonon distribution, therefore there exists no conflict with the calculation of the field-enhanced generation of points defects for HfO_2 by equilibrium thermodynamic calculations [21].

Jongmann *et al.* [111] also applied MD simulation in rutile TiO_2, and compared the simulation results with *in-situ* X-ray total scattering experimental results for the short range displacements of the Ti and O atoms of rutile TiO_2 during FS [112]. The idea is to correlate the non-linear vibrations of atoms to the softening of shear modulus, which leads to the lower formation energy of the point defects. Yoon *et al.* [112] claimed that a similar theory was applied for the supercooled liquids and glasses on the base of the knowledge gained from the face-centered cubic metallic system by Granato [113], in which the interstitials were claimed to be the reason for the decreasing shear modulus. The theory was also confirmed with experiments done with metallic glass [114]. However, it is worth mentioning that Granato's theory [114] is base on the dumbbell interstitials, which is common in metals. Therefore, the connection between these two theories requires a further carefully consideration.

2.4.2.4 Electrochemical effects

The partial reduction of a material due to the electrochemical effects has been attributed to the formation of 'electrochemical blackening' [3,115-116]. An oxygen ion conducting material is used as an example for the illustration of this phenomenon. On the anodic side, the reaction favors the generation of oxygen vacancies ($V_{\ddot{O}}$) as well as of electrons,

$$O_O^x \leftrightarrow 2e' + V_{\ddot{O}} + \frac{1}{2}O_2(g) \tag{2-38}$$

The positively charged oxygen vacancies move towards the cathodic side and react there with the electrons and oxygens according to the right side of Eq. 2-38. Biesuz *et al.* [3] pointed out that since this reaction is not fast enough, the oxygen vacancies get discharged according to the reaction as follows:

$$2e' + V_{\ddot{O}} \rightarrow V_O \tag{2-39}$$

The excess trapped electrons lead to the reduction of the surrounding cations, thereby a partial reduction of the oxide. This partial reduction and the accumulation of oxygen vacancies (electrochemical blackening) starts from the cathodic side and propagates to the anodic side. The associated transition of the presence of electronic conductance inside the material, promoted by the new energy level created by the trapped electrons. This has recently been experimentally proven by *in-situ* impedance spectroscopy using single crystal cubic zirconia [117]. Similar experiment has been conducted by Maso *et al.* [118] with polycrystalline 8 mol % yttria-stabilized zirconia (8YSZ), and the onset of electronic conductivity was found under small DC loading at high temperature. Maso *et al.* [118] argued that the reaction in Eq. 2-40 is more realistic rather than the alternative annihilation-creation mechanism (Eq. 2-39), and emphasized importance of O^- in enhanced conductivity.

$$O_O^x \rightarrow O_{\dot{O}} + e' \tag{2-40}$$

As discussed above, the electrochemical reactions in principle lead to a change of oxygen partial potential in the material, and the existence of oxygen potential transition has been modeled [119]. Moreover, the experiments have been conducted using grain size as the marker to prove the existence of oxygen potential transition [120-121]. Therefore, both experiments and modelling validated the correlation between oxygen potential transition in material and the movement of charged species. However, the role of electrical field on the generation of charged species, such as electrons and holes, is still unclear, because the mixed ion and electron conductivity was observed both in air [118] and reduced atmospheres [119]. In addition, Dong *et al.* [119] emphasized that poor electrode kinetics can also trigger the cathode reduction.

The electrochemical effect is also assumed relating to the alternation of grain boundary mobility induced under the DC loading, and thus the grain size gradients [85-86,120,122]. Direct experimental evidence for chemical reduction was reported by Jha *et al.* [86] with ceria and Charalambous *et al.* [85] with titania. They both observed a bifurcation into two peaks of the XRD signals near the cathodic side, and related this to the reduction of TiO_2 and CeO_2. However, this reduction on the cathodic side renders an inverse effects on the grain size (larger grain size for CeO_2 at anode, and larger grain size for TiO_2 at cathode). More specifically, on one hand, models and experimental evidence exist relating the accumulation of oxygen vacancies induced by the reduction on the cathodic side to a higher grain boundary mobility, and thereby a larger grain size. On the other hand, experimental evidence also exists for larger grain size on the anodic side.

Moreover, current flowing (flow of both ions and electrons) is essential in order to relate the observed phenomena to the above mentioned mechanisms. However, the type and concentration of defects in ZnO is irreversibly modified by electric fields, even if no current flows through the sample [19]. Also, the change of the electrical response of grain boundaries was found under DC flash sintering [88], but not under AC flash sintering [123]. In summary, the investigation on the influence of electrical fields still requires new experimental approaches as well as simulations on the non-equilibrium state.

2.5 Cerium oxide

2.5.1 Applications

The study of ceria as well as doped ceria has started years ago and has a wide use in industry, as the storage of Cerium is more abundant than copper and tin [124]. Ceria is used in applications such as exhaust catalysts [125-126], oxygen concentration sensors [127-128] and electrolytes in solid oxide fuel cell (SOFC) [129-130]. Ceria also demonstrates its possibility of industrial use in oxygen separation membranes for syngas production [131-132]. The SOFC is one of the most promising candidates for future power generation [133], as electricity can be generated from the chemical reactions without contaminations (Figure 16).

The application of material is generally based on its properties. Taking the electrolyte in SOFC as an example, several requirements have to be fulfilled [68,134-135], such as 1) high ionic conductivity (together with neglected electrical conductivity); 2) stability in both oxidizing and reducing atmosphere; 3) mechanical stability. The well-known material used is for this purpose yttrium doped zirconia, which usually operates in the temperature range of 700 °C-1000 °C [133]. Doped ceria can achieve higher ionic conductivity at lower temperatures (500 °C – 700 °C) [68,136-137], which provides the possibility to further reduce the energy consumption. Moreover, at lower temperatures, the interface reactions between different components inside the fuel cell will be suppressed, and leads to an increase of efficiency and lifetime of the cell [137]. Therefore, ceria based materials are also widely applied in solid oxide fuel cells as an alternative to zirconia, even though this kind of material also possesses several disadvantages, such as its reducibility at low oxygen partial pressure and its difficulty of sintering [138]. The latter can be solved by applying electric fields during sintering [137].

In general, in order to produce a product which meets the requirements of the industry, the sintering parameters need to be tailored on the base of knowledge of its mass transport and defect chemistry in the material.

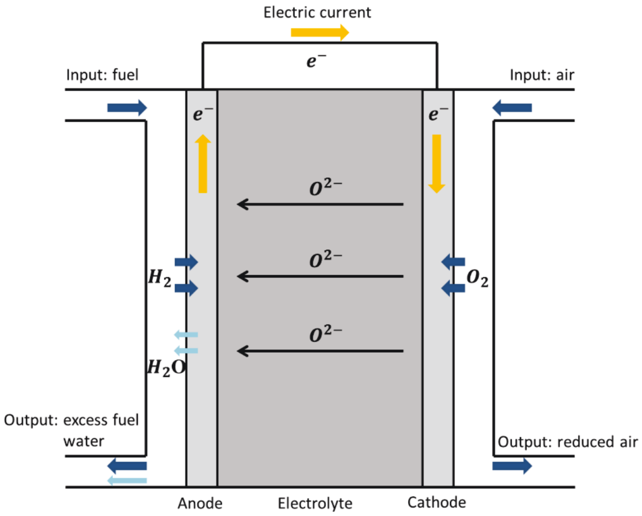

Figure 16: Schematic illustration of the working principle of SOFC during operation.

2.5.2 Crystal structure and defect chemistry

Cerium (valence electrons: $5s^2 5p^6 4f^1 5d^1 6s^2$) is the second member in the lanthanide series. As the most reactive element, *Ce* has two stable oxidation modes: $Ce^{3+}$and Ce^{4+} [124]. Ce^{4+} is more stable compared to Ce^{3+} due to the electronic structure, $5s^2 5p^6 4f^1$ for Ce^{3+} and $5s^2 5p^6$ for Ce^{4+}, because the fully occupied band is energetically more stable than the half-filled band. Figure 17 illustrates the band structure of ceria, with the valence band derived from *O* 2p while the conduction band from *Ce* 5d [139]. In order to generate the anti-Frenkel pair in CeO_2, an external electrical field with the magnitude of 0.1 GV/cm is needed, as reported in HfO_2 with the similar ~6 eV band gap [21].

Cerium dioxide (denoted as ceria in the following context) has a fluorite structure (FCC) with space group Fm3m (Figure 18a) and can also be interpreted as a cubic oxygen sub-lattice with the cerium ions occupying alternate octahedral interstitial sites (Figure 18b). In ceria, oxygen vacancies are the most well-known defects and are of an important technological importance. The oxygen vacancies can be introduced into the system either through the readily reduction from Ce^{4+} to Ce^{3+} (Figure 19a) or though doping (Figure 19b). For undoped ceria the color change is the first direct proof for the reduction of cerium: pure CeO_2 is pale yellow and the color turns from blue to almost black with increasing degree of nonstoichiometry [140].

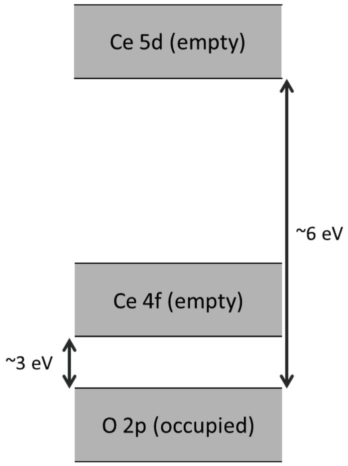

Figure 17: Schematic band diagram for ceria with no defects.

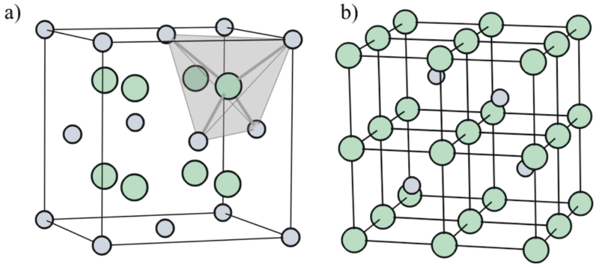

Figure 18: The crystal structure of stoichiometric undoped CeO_2 (grey spheres: *Ce*; green sphere; *O*). a) fluorite structure of cerium lattice with anions occupying tetrahedral sites; b) cubic structure of oxygen sub-lattice with cations occupying alternating octahedral sites.

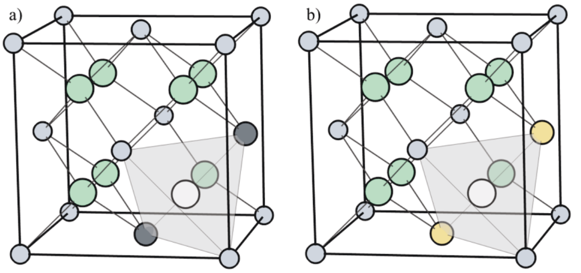

Figure 19: Schematic illustration of the generation of oxygen vacancies through a) the reduction of cerium; b) the doping with a trivalent element. (light grey spheres: Ce^{4+}; dark grey spheres: Ce^{3+}; green sphere; O^{2-}); hollow sphere: oxygen vacancy; yellow sphere: trivalent dopant).

The generation of oxygen vacancies in undoped ceria can be written in in the Kröger–Vink notation as follows:

$$O_O^{\mathrm{x}} + 2Ce_{Ce}^{\mathrm{x}} = 2Ce_{Ce}' + V_{\ddot{O}} + \frac{1}{2}O_2(g) \tag{2-41}$$

with O_O^{x} and Ce_{Ce}^{x} denote an ion sitting on its lattice site with neutral charge, Ce_{Ce}' denotes an ion sitting on its lattice site a single negative charge (the reduction from Ce^{4+} to Ce^{3+}) and $V_{\ddot{O}}$ denotes an oxygen vacancy with two positive charges. In the atomic point of view, the two positive charges are attributed to a vacancy in the following process: two electrons are trapped in the system when one oxygen ion (O^{2-}) leaves and forms a neutral species; these electrons are then inclined be localized at two cerium sites, the periphery of Ce^{3+} [124], which leaves the vacancy positively charged. The material is readily reduced, since the Ce^{4+}/Ce^{3+} conversion has a lower activation energy (0.21 eV [141]) than the oxygen migration energy (0.87 eV [142]), as pointed out by Chen *et al.* [143]. The reduction happens more easily at higher temperatures or reduced oxygen partial pressures.

An excess of oxygen vacancies can also be generated by introducing dopants with lower valences than Ce^{4+} (acceptor dopants), e.g. yttria studied in this work. The reaction of generating oxygen vacancies can be expressed as follows . [143]:

$$Y_2O_3 + 2Ce_{Ce}^{x} + O_{O}^{x} = 2Y_{Ce}' + V_{\ddot{O}} + 2\mathrm{Ce}O_2 \tag{2-42}$$

with Y_{Ce}' denotes a Y ion sitting on Ce lattice site with a single negative charge. The doping will not exclude the reaction (Eq. 2-40) in doped ceria. Therefore, in the case of doped ceria, it is noteworthy to distinguish an intrinsic regime, in which reaction (Eq. 2-40) dominates and an extrinsic regime, where the dopants affect the defect chemistry most . [143-144]. The separation criteria of these two regimes lies in whether the doping is dilute. By a common definition, doping is considered as dilute when its level is lower than 1 mol % [136,144].

In both intrinsic regime and extrinsic regime, the impurity center (Y_{Ce}') and oxygen vacancy ($V_{\ddot{O}}$) are the main ionic defects in doped ceria. These two defects have opposite charge. Therefore, these two species have a high tendency to combine, due to the electrostatic attraction. Moreover, the elastic interaction also exists inside the crystal structure. For example, *Y*, as an oversized dopant, may be attracted the open space of an oxygen vacancy [145]. Both factors lead to the formation of local defect complexes: $(Y_2V_O)^x$ and $(YV_O)^{\cdot}$ [136]. The latter, with no cation diffusion required, is favored, because the mobility of *Y* is reported to be negligible under 1000 °C [146]. Other defect clusters also exist, as reported by Li *et al.* [147], and he also pointed out that the inclination of low-temperature reduction in the ceria lattice is due to the short-range ordered defect complex.

2.5.3 Ionic conductivity

In order to investigate the mass diffusion of oxygen ions, the ionic conductivity, determined by the migration of oxygen ion, is used as a benchmark. The temperature dependency of ionic conductivity can be expressed on the base of Arrhenius relation is as follows [136,148]:

$$\sigma T = Aexp(-\frac{H_\sigma}{kT}) \tag{2-43}$$

where σ is ionic conductivity, A is the scaling factor, and H_σ is the effective activation enthalpy, consisting of association enthalpy of defect complex (H_A) and migration enthalpy (H_m). With increasing doping levels, the ionic conductivity first increases in the range of dilute doping and then decreases, as reported by Wang *et al.* [136]. This behavior can be attributed to the decrease of association enthalpy at low concentration range, and increase of migration enthalpy at the high concentration range [143]. From the microscopic point of view, three paths are possible for the oxygen ion migration (Figure 20a) and path I (Figure 20a) along the <001> direction is reported to be most favored due to low migration energy

[149]. More specifically, the ionic conductivity has only been discussed in the context of oxygen-ion jump in the crystal lattice regardless of the microstructural characteristics, such as grain boundaries. This ionic conductivity is attributed as the bulk conductivity, which is the intrinsic property of the material.

In polycrystalline materials, oxygen ionic conductivity is greatly influenced by the microstructural characteristics (e.g. grains boundaries). As pointed out by Chen *et al.* [143-144], the grain boundary mobility in the intrinsic regime is enhanced by doping elements with low association enthalpy of defects complex (*Y* and *Gd*), and on the other hand, suppressed by elements with high binding energy (Sc and *Yb*), because of the opposite effects of these elements on the free oxygen vacancy concentration. While in the extrinsic regime, the mobility is suppressed due to solute drag, among which 1 mol % *Y* doping in CeO_2 exerts the most effective suppression. The build-up of the solution cloud can be explained either by elastic mismatch or by electrostatic interactions (space charge layer).

The process of sintering requires both cation and anion diffusion. In the case of ionic ceramics, the diffusion of cation and anion should preserve the total charge of the material. The cation diffusion in our case is the rate limiting transport process. More specially, the slowest element in the fastest path would dominate the kinetics, i.e. the grain boundary diffusion of cation is of great importance.

The cation diffusion (diffusion of Ce in yttria doped ceria) is accomplished either by interstitial or vacancy diffusion. Chen *et al.* [143-144] proposed that cation diffuses through interstitial mechanism, and suggested that cation interstitial concentration increases according to oxygen vacancies (Figure 20b). On the other hand, Beschnitt *et al.* [150] pointed out that with adjacent oxygen vacancy, the migration enthalpy is also the lowest for the vacancy mechanism along <110> direction ((Figure 20b)). Moreover, the cerium interstitial concentration is much lower compared to cerium vacancies concentration in acceptor-doped CeO_2. Dong *et al.* [151] further developed the theory using the first-principle method and concluded that the pure size effect due to adjacent oxygen vacancy can only slightly mitigate the migration energy. It is the synergistic effect of reduction and oxygen vacancy together that has the largest effect due to electrostatic consideration. Moreover, the lowest migration energy is around 3.28 eV for vacancy mechanism in ceria. Nevertheless, the enhanced cation diffusion with higher oxygen vacancy concentration is also experimentally observed. Kinemuchi *et al.* [152] attributed the sintering rate of submicron ceria to cation diffusion through oxygen vacancies on the base of dilatometer analysis. This assumption is also supported by the successful attempts to enhance the sintering activities of ceria by increasing oxygen vacancy concentration, which is achieved by sintering ceria under lower oxygen partial level [153-154].

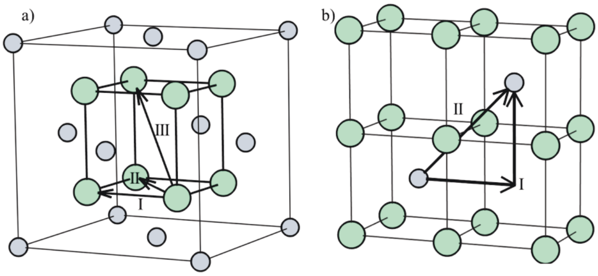

Figure 20: Schematic illustration of a) oxygen diffusion mechanism with path I along <001>, path II along <011> and path III along <111>; b) cerium diffusion mechanism with path I: interstitial mechanism and path II: the vacancy mechanism (light grey spheres: Ce^{4+}; green sphere; O^{2}).

2.5.3.1 Conductivity measurement

The conductivity of materials is characterized by an electrochemical impedance spectroscopy (EIS), which will be introduced in section 3.5. For a single-phase crystal, the three arcs correspond to the grain interior, the grain boundary and the electrode with decreasing frequency [155]. Typical results obtained from EIS is shown in Figure 21.

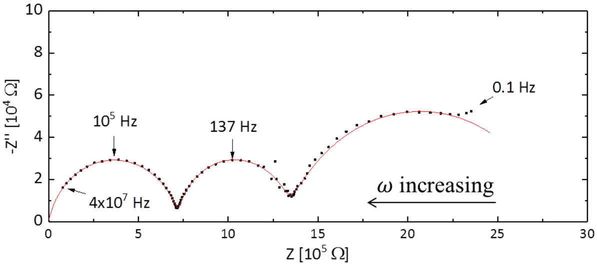

Figure 21: Schematic impedance plot (black dot) and the resulting fit results (red) of 10YDC at 200 °C.

As can be seen in Figure 21, different domains have been attributed to the measured arcs. EIS acts as a tool to build the connection between the model and the behavior of a real system. It is necessary to relate the microstructural components to electrical elements in order to simplify [156]. The benchmark used is the similarity of the electrical response between the microstructural characteristic and electrical elements. The basic electrical elements involved are resistors, capacitors and inductors:

- Resistance (R), where the current follows the voltage without a delay:

$$Z(t) = R \tag{2-44}$$

The resistance is the instantaneous response of the current to the voltage, which can be involved with the directional movement of charge carriers (simple defects such as vacancies, ionic interstitials and etc. or electrons).

- Capacitance (C), where the current can not follow through, but an accumulation of charges can form:

$$Z(t) = \frac{1}{j2\pi fC} \tag{2-45}$$

The real current signal obtained from the experiments is usually out-of-phase compared with the input voltage signal. Therefore, a capacitor is used to simulate this kind of behavior, which involved with the polarization of the defects with electric dipole moments, usually complex defects (Section 2.5.2) [157]. Each capacitor is characterized by its relaxation time and or a distribution of them, if it involves the polarization of several main clusters of complex defects. Funke and Wilmer [158] pointed out that relaxation time is related to the time required for system to relax the mismatch introduced by the ion hopping. In summary, the physical transport and charge transfer process is frequency related [159].

- Inductance (L), where the voltage is built due to the electromotive force induced by the current:

$$Z(t) = j2\pi fL \tag{2-46}$$

With f denoting frequency. The inductance is due to the disturbing signal introduced by the inductor in the equipment, which can not be eliminated, and depends on the length of leads and their positioning. This signal noise can be obvious especially at higher temperatures.

Taking a single-phase ceramic as an example, it is commonly accepted that the bulk can be interpreted as a resistance and a capacitance, connected in parallel (parallel RC element) [157,160]. Bauerle *et al.* [157] at first extended the study into the polycrystalline form, by introducing the a second phase as the grain boundaries. Ho *et al.* [161] confirmed the contribution of grain boundary impedance by the measurements of polycrystalline $Li_{4+y}Si_{1-y}Al_yO_4$ varying from 60 % of relative density to almost the theoretical density. The studies [157,161] also indicate that the microstructure characteristics do not perform as a perfect capacitor, because even in the microscopic point of view, material properties are themselves often distributed or not homogenous [157]. Therefore, in a real microstructure, a RQ element (resistance and constant phase element) is usually used instead of a RC element of the specific domain. The effective capacitance of the RQ element (C_{eff}) and the impedance of the constant phase element (Z_Q) are calculated as follows:

$$Z_Q = 1/[Q(iw)^n] \tag{2-47}$$

$$C_{eff} = Q^{1/n}R^{(1/n-1)} \tag{2-48}$$

where Q and n are the constants of the constant phase element, ω is the frequency and R is the resistance of the specific domain. In order to assign the RQ element to different domains of a single-phase specimen, the magnitude of capacitances is used as the criterion, which is listed in the following table.

Table 1: Capacitance values and the possible microstructural feature [160].

Capacitance (F)	**Microstructural characteristic**
10^{-12}	bulk
10^{-11}	Minor, second phase
10^{-11}-10^{-8}	Grain boundary
10^{-10}-10^{-9}	Bulk ferroelectric
10^{-9}-10^{-7}	Surface layer
10^{-7}-10^{-5}	Sample-electrode interface
10^{-4}	Electrochemical reaction

Afterwards, an equivalent circuit consisting of the electrical elements is generated. The equivalent circuits are proposed to fit the experimental results. To deliver the same fitting results, there exists normally not only one equivalent circuit. Therefore, the equivalent circuit analysis should be combined with the microstructure model as well. The most common model used for the polycrystalline crystal is the so-called brick-layer model [162] (Figure 22), and the corresponding equivalent circuit based on this microstructure model is depicted in Figure 23.

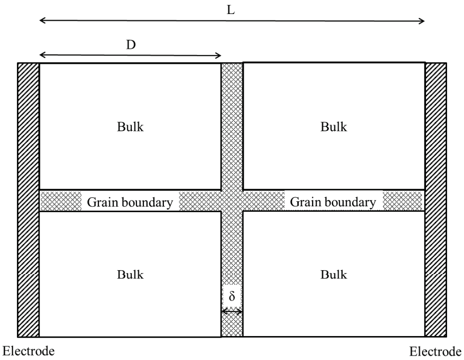

Figure 22: Brick layer model for polycrystalline ceramic, showing array of cubic grains, separated by flat grain boundaries.

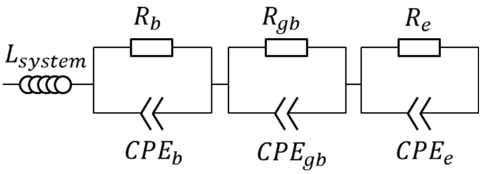

Figure 23: Circuit equivalent for a polycrystalline ceramic and modeling the RC element of the bulk (b), grain boundary (gb) and the electrode (e) with the inductance due to the system connected in series.

Thereby, the conductivity of different domains can also be calculated accordingly. The specific grain interior conductivity, σ^{b}, can be calculated from the bulk resistance, R^{b}, sample thickness L and sample cross-sectional area A according to the following equation:

$$\sigma^{\mathrm{b}} = \frac{L}{A \cdot R^{\mathrm{b}}} \tag{2-49}$$

However, when it comes to grain boundaries, since the effective length and area of grain boundary is unknown, and do not equal to the sample dimension. Therefore, instead of the resistances of the single grain boundary, the total conductivity of grain boundaries, σ^{gb}, in series with the grain interior, is calculated from the grain interior resistance, R^{gb}, as follows:

$$\sigma^{\mathrm{gb}} = \frac{1}{R^{gb}} \frac{\mathrm{L}}{\mathrm{A}} \left(\frac{\delta}{\mathrm{d}}\right) \tag{2-50}$$

where δ is the effective grain boundary thickness (i.e. the thickness of the GB core plus the extension of the space charge layer on either side of the core) and d is the grain size. Considering that dielectric constants of most materials lies in the range of 5 to 100 [157], it is reasonable to assume the dielectric constants of grain and grain boundary are almost the same, which leads to [155]:

$$\frac{C^{\mathrm{b}}}{C^{\mathrm{gb}}} = \frac{\delta}{d} \tag{2-51}$$

In summary, the brick layer model is used to analyze the obtained Nyquist plot from polycrystalline materials with two or three arcs. Thereby, information such as effective bulk and grain boundary conductivities and capacitance can be calculated and used in understanding the ion transfer inside the material.

3.Methodology

The material system used in this work is a commercially available powder (CerPoTech, Tiller, Norway) with two kinds of doping: 10 mol % yttria doped ceria, $Ce_{0.9}Y_{0.1}O_{2-\delta}$, (10YDC) and 0.1 mol % yttria doped ceria, $Ce_{0.999}Y_{0.001}O_{2-\delta}$, (01YDC). The process applied to produce the powder is described as follows: at first, the pyrolysis, in which a water-based solution containing dissolved cerium- and yttrium ions, was sprayed into a furnace to form oxide powders. The powders were then calcined to remove any nitrates or carbonates, and to form a homogeneous single-phase material. Subsequently, the agglomerates were broken down by wet ball milling. Finally, the powders were sieved and calcined at 400 °C to remove any organic residuals from processing. In order to finish all the experiments in the PhD thesis, the powders were purchased three times, denoted as Batch1, Batch2 and Batch3, respectively, in the following part.

3.1 Material characterization

Different methods to characterize the powder properties are listed and briefly described below.

3.1.1 Particle size distribution

The laser diffraction method was used for the measurement of particle size distribution (PSD). The experiments were performed with a static laser diffraction particle size analyzes LA-950 (Horiba, Kyoto, Japan) with 2 laser diodes providing two kinds of wavelengths: 650 nm and 405 nm. The shorter wavelength is important to extend the lower limit of the measurements because of its high sensitivity for small particle size. It can be used to measure both dry samples and dispersions with particle sizes from 30 nm to 3 mm [163].

The working principle is based on the different scattering angles due to different particle size, and the PSD is calculated from the pattern of scattered light characterized by intensity and angle [164]. More specifically, the intensity increases while the diffraction angle decreases with larger particle size. In order to calculate the PSD on the base of experimental results, Fraunhofer models and Mie models are applied. Fraunhofer theory as a simplification of the Mie theory is usually used for large particles. One simple limitation is that the diameter of particle size is at least about 40 times of used light wavelength [164]. Refractive light becomes important for a high accuracy of PSD determination with particle size smaller than limit.

For this work, considering the small particle size, the Mie theory was used. The refractive indexes were taken as [165-166] 2.2-0.05i for 10YDC and 1.688 for 01YDC.

3.1.2 Specific surface area

The specific surface area is a parameter used to indirectly measure particle size and surface morphology defined as the ratio between total surface area and mass of the powder. The experiments were performed with a SA-9600 Surface Area Analyzer (Horiba, Kyoto, Japan).

The working principle is based on the assumption that gas molecules can be adsorbed on the solid surface. Generally, there are two types of adsorption: physisorption (gas adsorbed on the surface through van der Waals force) and chemisorption (gas adsorbed on the surface via electrochemical bonding. The flowing gas method applied by the equipment is built on the physisorption principle. More specifically, the surface of the measured powder is at first chilled until the boiling temperature of liquid nitrogen (–196 °C), and then gas is purged into the chamber for the adsorption, finally, the temperature inside the chamber increases for desorption [167]. Thereby, the adsorbed gas area is measured.

The specific surface area was calculated using a mathematical model proposed by Stephen Brunauer, Paul Hugh Emmett and Edward Teller (BET) [168]. The direct measured adsorbed gas volume was based on multilayer adsorption. The model was used to transfer the gas volume for multilayer adsorption to the gas volume for monolayer adsorption, which revels the real information of the exposed surface of the sample. The general equation is:

$$\frac{1}{V(\frac{P}{P_o}-1)}=\frac{c-1}{V_m c}\times\frac{P}{P_o}+\frac{1}{V_m c} \tag{3-1}$$

with c as the constant relating to the enthalpy of adsorption, P as the partial vapor pressure in equilibrium of the chamber, P_o as the standard pressure of adsorbate gas at the boiling temperature, V as the measured volume of adsorbed gas and V_m as the volume of gas adsorbed in the monolayer. Via plotting $1/(V(P/P_o-1)$ vs P/P_o, the desired V_m can be calculated. However, this linearity is only valid when P/P_o lies in 0.05 and 0.3 [168]. With varying partial pressure, a multipoint fitting can be conducted for a more reliable extrapolation.

3.1.3 X-ray diffraction

The X-ray diffraction method is a fast and non-destructive measurement of lattice parameters and the crystal structure of a material. The experiments were performed with a D4 endeavor (Bruker AXS

GmbH, Karlsruhe, Germany). X-ray diffraction was used to define the lattice parameter, and validate the crystal structure of the material.

The working principle of XRD measurements performed in this case is based on the interference of X-rays and the crystal structure of the sample. Generally, the target material (Cu) is hit by the accelerated electrons via high voltage (40 kV, 40 mA). When the energy of the accelerated electrons is higher than a certain threshold value, electrons from one of the inner electron shells are excited. This leads to electrons from a higher atomic level dropping to the vacant level with the emission of a characteristic X-ray radiation, Cu-$K_{\alpha 1,2}$. Meanwhile, the sample is measured in a Bragg-Brentano geometry in the range of 10 °- 80 ° with a step size of 0.02 ° and 0.75 s/step.

The peak position as well as the peak intensity of reflections is the fingerprint of the crystal structure. The X-ray detector can only receive the signal when the Bragg's law is obeyed, which describes the elastic scattering of X-ray waves by the crystal lattice and reads:

$$n\lambda = 2dsin\theta \tag{3-2}$$

where n: the order of diffraction, λ: the wavelength of X-ray; d: the spacing of crystal planes; θ: the incidence and reflection angle (Figure 24). Correspondingly, only when the diffracted beams of the parallel planes are in phase, the reflection will happen and at the same time, the intensity amplifies instead of annihilation.

The intensity of reflected X-rays, I, is expressed as a Fourier transform within the first-order Born approximation, in which it is proportional to the square of structural factor, F_{hkl}:

$$I \propto |F_{hkl}|^2 \tag{3-3}$$

structural factor, F_{hkl}, describes the relationship between diffraction of the crystal lattice and a single electron of one atom [169].

$$F_{hkl} = \sum_{j=1}^{N} f_j e^{-2\pi i(hx_i+ky_i+lz_j)} \tag{3-4}$$

where N: the number of atoms in the unit cell, f_j: the scattering factor for each atom; x_i, y_i, z_j: the coordinates of each atom in the unit cell; h, k, l: Miller index of crystallographic planes. The diffraction can only happen with $F_{hkl} \neq 0$. That is to say, not all crystallographic planes can be detected via X-ray diffraction. Together with the information such as crystal structure, the lattice parameter can be determined using Bragg's law.

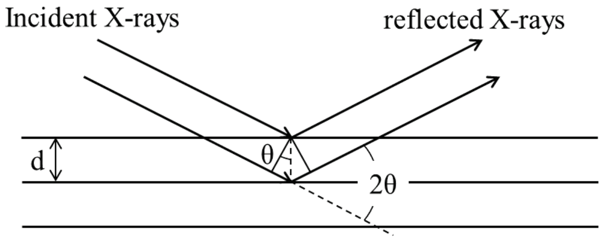

Figure 24: Schematic illustration of the working principle of X-ray diffraction.

X-ray diffraction method also provides information about the crystallite size. More specifically, the half width of peaks is related to the crystallite size and micro-strain in the polycrystalline samples. Thereby, the peak width can be used to calculate the crystallite size [170].

3.1.4 Inductively coupled plasma optical emission spectrometry

The stoichiometry of the material was measured using ICP-OES, which uses the emission spectra of samples to define and quantify the element content. For the 10YDC and 01YDC, weight percentage of cerium, yttrium as well as other impurities was obtained. The oxygen content cannot be detected with this technique. 50 mg powder was mixed with 2 mL H_2SO_4 and 2 mL H_3PO_4, and then diluted with 2 mL HNO_3 and 2 mL H_2O_2 to 50 mL. The quantitive determination of cerium requires further dilution to one to hundredth while the determination of yttrium together with other impurities requires a dilution until one to tenth.

3.2 Sample preparation

Three kinds of samples were prepared for different kinds of tests: cylindrical bulk samples, dog-bone shape samples and disk samples.

3.2.1 Cylindrical bulk samples

Bulk samples are designed for the preliminary sintering characterization experiments, sintering parameter (Section 2.3.2) measurements and activation energy measurement. Three sets of bulk samples were prepared. Before experiments, the top and bottom surfaces of the specimens were polished with SiC paper with 4000 grit to ensure a smooth surface and thereby a better contact between sample and electrodes.

The first Batch of bulk samples was prepared using 10YDC-Batch1 for preliminary sintering characterization experiments. To allow for particle coarsening and a more homogeneous particle size distribution, the as-delivered powder was calcined at 1150 °C for 3 h and milled in ethanol for 72 h with a speed of 90 rpm using a tumble mixer. After calcination and grinding, the suspension was put to stand for 3 h and dried. The specimens were uniaxially pressed with a 8 mm diameter press form (Msscientific Chromatographie-Handel GmbH, Berlin, Germany) under 100 MPa for 1 min to be able to be fixed into Netzsch TMA402 F1 (Netzsch, Selb, Germany). The cylindrical specimens of 10YDC were 6.48 mm±0.5 % in height and 7.5 mm±0.5 % in diameter, with a relative green density of 57.98 ± 2 %. Manufactured cylindrical specimens of 01YDC were 6.33 mm±2 % in height and 7.55 mm±0.2 % in diameter, yielding a relative green density of 59.7±0.6 %.

The second set of bulk samples was prepared using 10YDC-Batch1 after calcination and milling as the first set for sintering parameter measurement under different conditions. Cylindrical specimens were at first uniaxially pressed using a die with 10 mm diameter under 100 MPa for 1 min and subsequently cold isostatically pressed at 300 MPa for 1 min. The obtained cylinders of 10YDC were 14.80 mm±0.9 % in height and 9.39 mm±0.6 % in diameter, yielding a relative green density of 62.0±2 %.

Another set of bulk samples was prepared using 01YDC-Batch3 and 10YDC-Batch3 for the sintering parameter measurement as well as activation energy measurement. Cylindrical specimens were first uniaxially pressed using a die with 10 mm diameter under 5 kN for 1 min and subsequently cold isostatically pressed at 300 MPa for 1 min. Subsequently, the samples (01YDC) used for the viscosity measurements were preheated with a heating rate of 20 K/min to 900 °C for 1 h and cooled down with a cooling rate of 10 K/min to maintain the same heating history as the dog-bone shape samples, which will be introduced in the following part. The obtained specimens of 01YDC were 14.87 mm±0.5 % in height, 9.26 mm±0.2 % in diameter, yielding a relative green density of 69.5±0.6 %. The activation energy measurement was conducted on samples without preheat program, the obtained specimens of 10YDC were 15.47 mm±0.1 % in height, 9.27 mm±0.3 % in diameter, yielding a relative green density of 61.8±0.4 %. The obtained specimens of 01YDC were 14.9 mm±1 % in height, 9.28 mm±0.4 % in diameter, yielding a relative green density of 63.3±0.6 %.

3.2.2 Dog-bone shape samples

Dog-bone shaped samples were designed to perform the viscosity measurements under tensile stress and prepared using the 01YDC-Batch3 powder. In order to avoid the anisotropy and defects brought by uniaxial pressing, the as-received powder was pressed using a die with 25 mm diameter under 15 kN for 1 min and then cold isostatic pressed at 300 MPa for 1 min. Subsequently, the disks were preheated with a heating rate of 20 K/min to 900 °C for 1 h and cooled down with a cooling rate of 10 K/min to increase the mechanical stability. The flat dog-bone shaped tensile specimens with a gauge length of 10 mm, width of 2.7 mm were machined with pre-sintered disks by water jet. Two small holes with a diameter of 1.5 mm were created by mechanical machining to connect platinum wires, and the distance between the two small holes was defined by the distance to the edge (Figure 25). The obtained dog-bone shaped specimens of 01YDC were 2.68 mm±0.3 % in width, 3.41 mm±0.6 % in thickness and 10.01 mm±0.2 % in gauge length, yielding a relative green density of 70.0±0.4 %. Subsequently, Pt paint was applied to the surface of the two small holes three times, followed with a annealing for 20 min using a hot plate after each painting. After the specimen was fixed to the SiC jig, additional Pt paint was applied again in the gap between the hole and Pt electrode.

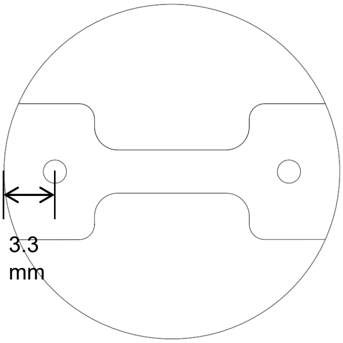

Figure 25: Sketch of the design of the dog-bone shape sample.

3.2.3 Disk samples

The disk samples were designed for the impedance spectroscopy measurements, which will be described later. The specimens were prepared using 10YDC-Batch2 and 01YDC-Batch2. The powder was pressed uniaxially using a die with 13 mm diameter under 100 MPa for 2 min to give a pellet of (13.01 mm±0.08 %) in diameter and (3.0 mm±0.3 %) in height, yielding a relative green density of 52.2±0.6 %.

The pellets were sintered with a heating rate of 30 K/min to 1300 °C for 2 h and then cooled down with a cooling rate of 30 K/min to freeze the grain boundary structure at high temperature. Electrical fields were also applied during the sintering, both contacting and non-contacting electrical fields. For electrical fields, different conditions of applied electrical fields E_{rms}=0 V/cm, 14 V/cm and 28 V/cm with a frequency of 50 Hz were applied. For non-contacting electrical fields E_{rms}=50 V/cm and 100 V/cm, two alumina disks with a thickness of 0.66 mm were settled between the electrodes and the specimen, as illustrated in Figure 26. The relationship between the external applied voltage and the voltage applied on the sample is described as follow:

$$V = \frac{V1}{d} 2\varepsilon_r^{Al_2O_3} d^{Al_2O_3} \tag{3-5}$$

where V is the set volt set , $V1$ is the set volt between electrodes, d is the thickness of the sample and $d^{Al_2O_3}$ is the thickness of alumina disk, $\varepsilon_r^{Al_2O_3}$ is the relative dielectric constant of alumina. For contacting electrical field E_{rms}=28 V/cm, the specimen temperature during the experiments were kept constant by lowering furnace temperature, as introduced in section 3.3.2.

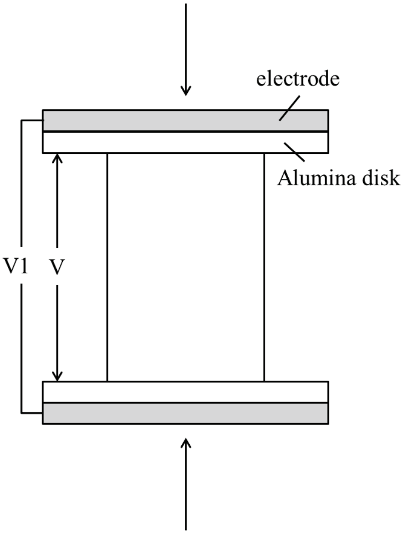

Figure 26: Set up of non-contacting electric field.

The densities of the sintered samples, determined according to Archimedes' principle, were 94 %-96 % of the theoretical density. After the sintering, samples were then mechanically ground with SiC paper down to 4000 grit to a thickness of 1.00 - 1.60 mm. Pt|Ag electrodes were manufactured for both specimens: at first, both top and bottom surfaces were sputtered with Pt generated by 20 mA for 150 s using a desktop sputter coater (Cressington Scientific Instruments Ltd., Watford, UK). Thereby, the contact between the specimen and electrodes can be improved. Subsequently, Ag paint was applied for three times at each surface, after each painting, the specimen was dried for 20 min in the explosion-proof furnace. Finally, the samples were then annealed with a heating rate of 2 K/min at 650 °C for 1 h. The produced electrodes were about 1 mm thick.

3.3 Calibration of temperature distribution

As introduced in Section 2.4.2.1, the difference in sample temperature as well as the furnace temperature is one of the main issues that needs to be clarified in studying the effect of electrical fields. The approach for the measurement of sample temperature is elucidated in the following part.

3.3.1 Infrared (IR) camera

The sample temperature was measured using an IR camera, FLIR SC655 (FLIR Systems, Inc., Oregon, USA). It was equipped with a 41 mm objective, which offers a field of view of $15^o \times 11^o$. With an IR camera, the non-contact temperature measurements of sample surface can be performed directly with an accuracy smaller than 1 °C. The densified samples were heated with a heating rate of 30 K/min to 1200 °C, and held at sintering temperature until the temperature was stabilized, and then the power source was turned on, off and on again, each time for at least 15 minutes. The experimental setup is shown in Figure 27. The radial laser receiver was removed to allow the set-up the IR camera.

It is noteworthy mentioning that the measurements by the IR camera can be easily influenced by the atmosphere between the target and the camera, because the signal is transferred through the atmosphere to the detecting system. In our work, the radiation of the heating elements, the furnace and etc. are all factors that can influence the accuracy of the measurements. Especially the heating elements, because the position of one of the heating elements is directly in front of the specimen (Figure 27b).

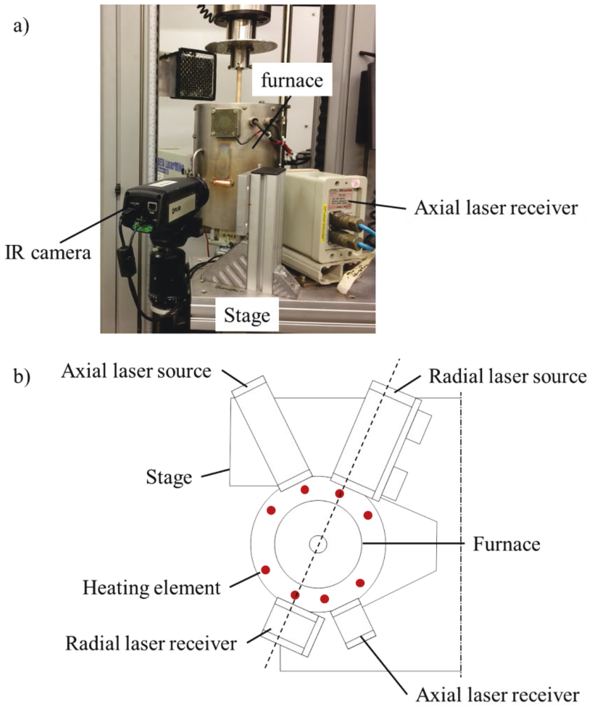

Figure 27: Setup of temperature measurement using IR camera a) front view b) top view.

3.3.2 Thermocouple measurement

An alternative for the temperature determination is through a direct measurement via thermocouples. Thermocouples are sensors generating a voltage that changes over temperature. By detecting the current between the temperature sensing junction and the reference junction maintained at the isothermal temperature, the temperature can be then calculated on the base of the Seeback effect. Table 2 lists the thermocouple used in this work and its properties according to the International Electrotechnical Commission Standard (IEC-EN60584).

Table 2: Information of thermocouple type, materials, temperature range and thermocouple error according to The International Electrotechnical Commission Standard (IEC-EN60584).

Type	Materials	Temperature range (°C)	Thermocouple error (°C)
S	Pt10Rh-Pt	0-1600	±1.5 or (0.0025x|T|)

More specifically, the temperature calibration was conducted with a fully densified specimen of 10YDC-Batch1 (8.08 mm in diameter) with a 3 mm ± 0.05 mm depth hole drilled mechanically. Three thermocouples were installed (Figure 28): the thermocouple 1 was used to measure the furnace temperature (T1). An insulating mantle thermocouple was used to measure the temperature inside the sample (T2) and the third one was used to measure the temperature near the sample surface (T3), 2mm away from the sample surface. The thermocouples used in this study were all of type S with accuracy of ± 1.5°C. The sample was heated to different furnace temperatures: 1100 °C, 1200 °C, 1300 °C, with 0 V/cm and field strength of E_{rms} = 14 V/cm, 21 V/cm, 28 V/cm and 42 V/cm until the temperature was stable. Each measurement was repeated twice.

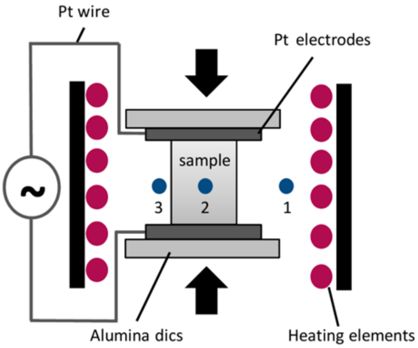

Figure 28: Schematic of the placement of thermocouples: T1: furnace; T2: inside sample; T3: near sample surface.

3.3.3 Simulation setup

Finite element analysis (FEA) was conducted with a commercial software, Ansys Workbench 19.2 (ANSYS Inc., Canonsburg, USA) to simulate the temperature distribution of the specimen inside the furnace during the experiment. Densification was not taken into account by this model. The geometry used in the simulation included all main features of the experimental setup of the loading dilatometry, in order to yield realistic results that reflect all heat transport processes inside the furnace (Figure 30). To save simulation time, half of the 3D geometry was modelled and a corresponding symmetry condition was applied. The mesh was generated with quadrangular element type.

The thermal expansion coefficient was measured separately (+ 2K/min, 1400 °C, 30 min, - 2 K/min). The electrical resistivity of the specimen was measured during constant heating rate experiments. Figure 29 and Table 3 summarize the material properties used for this model. The boundary conditions of the model were the following: the top sample surface was set to different dc electrical potentials (the same as the effective ac potentials in the experiments) and the bottom sample surface was kept at 0 V. Heat losses through heat conduction between specimen and alumina disks (the temperature at the end of the alumina pushing rod was denoted in Figure 30) and heat radiation from sample surface, alumina disks and electrodes were taken into account. Samples were heated internally by Joule heating and externally by heating elements inside the furnace through the radiated heat transfer from the furnace to the sample.

Table 3: Material properties of 10YDC

Property	10YDC
Density [g/cm^3]	6.983
Thermal conductivity [W/mK]	12 [140]
Emissivity	0.98

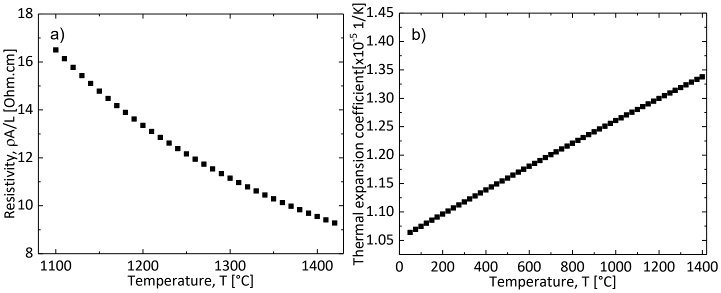

Figure 29: a) Resistivity of 10 YDC; b) coefficient of thermal expansion of 10YDC.

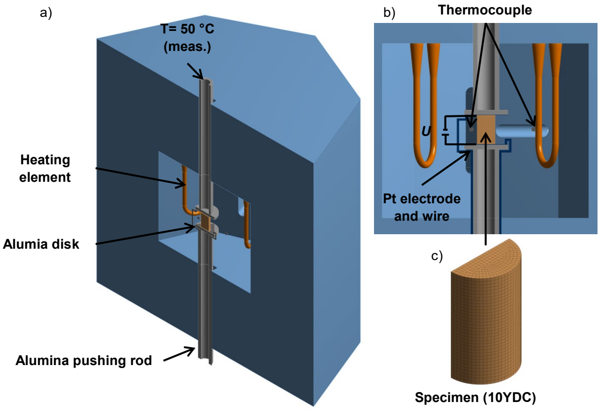

Figure 30: Finite element model of the loading dilatometry test frame a) isometric view; b) detailed front view of furnace chamber; c) mesh of the sample.

3.4 Dilatometric methods

The shrinkage over time and temperature is the fingerprint of the samples during sintering. Dilatometric approaches are typical to obtain such information. In the following part, three dilatometry used in this work are introduced.

3.4.1 Differential thermal analysis / Thermogravimetric analysis

The DTA/TG method was applied to have a deeper understanding of the sintering process. The DTA/TG measurements were carried out with the thermal analyzer STA 449 F1 Jupiter coupled with mass spectrometer QMS 403C Aëolos (Netzsch, Selb, Germany).

The experiments were designed as follows: the powder was at first heated with a heating rate of 30 K/min to 1000 °C, and then held at sintering temperature for 30 minutes under an argon atmosphere. Subsequently, the powder was cooled down. The air was purged into the system when the temperature was stable at RT. Afterwards the powder was heated again with a heating rate of 30 K/min to 1000 °C under air atmosphere in the second period.

TG is an analysis aiming at measuring the mass change in dependence of temperature under a controlled atmosphere. It is a powerful method which provides information of reactions happening along with the temperature, including physical reactions involving evaporation, physisorption, desorption, chemical reactions involving chemisorption, thermal decomposition, oxidation and etc. However, it is noteworthy mentioning that some reactions will take place without mass change, for example, phase change, glass transition and so on. Therefore, this technique is usually combined with DTA for a complete analysis. DTA is a technique to measure the temperature difference between the specimen and the temperature inert reference material. The peak of the signal in this context represents the exothermic reaction while the valley represents the endothermic reaction.

3.4.1.1 Conventional dilatometry

Preliminary sintering experiments with bulk samples were conducted at first with a Netzsch TMA402 F1 dilatometer (Netzsch, Selb, Germany) in order to determine the appropriate sintering temperature for sintering parameter measurements. This dilatometry array [171] consists of a SiC furnace with an operating temperature range from room temperature (RT) to 1550 °C and controlled heating/cooling rates from 0.001 K/min to 50 K/min, a highly precise inductive displacement transducer (LVDT) for the displacement measurement until 5000 μm with the digital resolution of 1.25 nm, integrated mass flow controllers (MFC), which offers a accurately controlled atmosphere (inert, air and vacuum with pressures less than 10 $^{-4}$ mbar) and electromagnetically force control system allowing the forces to be set in the mN-range from 0.001 N to 3 N.

The experiments were designed as follows: the samples were at first heated with a heating rate of 30 K/min to 1200 °C 1300 °C and 1400 °C, and then held at sintering temperature for 8 hours under an air flow of 60 ml/min. During the experiment, a minimal load of 50 mN was used to maintain the contact between the measurement setup and the sample.

3.4.2 Custom made loading dilatometry

Two kinds of custom made loading dilatometry were used in this work. One is at IEK1, Forschungszentrum Jülich, Germany and the other one is in the National Institute of Material Science, Tsukuba, Japan.

The first custom made loading dilatometry equipment in Jülich is the only testing frame allowing the measurement of both diameter and height during the experiments [172]. It is equipped with an independent programmable power source (ACS-2200-PS from HBS Electronic GmbH, Brühl, Germany). The controllable mechanical load (10 N - 160 N) was applied with an electromechanical testing system (model 5565, Instron, Norwood, USA) with an accuracy of 0.1 N. The radial and axial strains during sintering were optically measured by two laser scanners (Model 162-100, Beta LaserMike, Dayton, USA), allowing a dynamic resolution of about 2 μm. The instantaneous relative density, $\bar{\rho}$, during the experiments was calculated automatically on the basis of the measured data:

$$\bar{\rho} = \frac{\rho_0}{\rho_{th}.\exp\,(2\varepsilon_r+\varepsilon_z)} \tag{3-6}$$

where ρ_{th} is the theoretical density and ρ_o is the green density.

The second custom made loading dilatometry equipment in Japan consisted of an independent power source (High voltage amplifier, model HAP-0.6B2000, Matsusada Precision Inc, Shiga, Japan) and an electromechanical testing system (Instron 5581, Instron, Norwood, USA) with an accuracy of 0.1 N, aiming at applying mechanical load (1 N – 17 N) [173]. The specimens were fixed into the testing frame using SiC jigs. Tensile extension was determined from the crosshead displacement under the assumption that the elongation as well as the sintering of the sample was uniform in the gauge region.

3.4.2.1 Determination of sintering parameters

As introduced before, the main idea for the measurement of sintering parameters require the application of mechanical loads on the specimen with a specific relative density. Two approaches are applied most commonly for the purpose. The discontinuous loading dilatometry was applied in this work.

3.4.2.2 Cyclic loding-dilatometry

During cyclic loading-dilatometry, a constant uniaxial load is applied intermittently (for a small range of density) on a cylindrical sample. Strains in the both directions (axial direction or radial direction) or only axial shrinkage can be recorded as a function of time and density, allowing computing sintering parameters. The load-free periods should be effective in removing the stress-induced microstructural alteration due to the loading periods. The major advantage of this technique is that only a single run is needed to compute the sintering parameters over the whole density range. The disadvantage is that it is difficult to switch between loading and loading-free period. Mohanram *et al.* [174] performed the cyclic loading-dilatometry, with only axial strain recorded, to measure viscosity of glass-based system.

3.4.2.3 Discontinuous loading-dilatometry

Discontinuous loading-dilatometry is a technique to apply a constant uniaxial load on specimens only once and for a short range of time during the experiment. Both axial and radial strains are recorded as a function of time and density. This technique has already been successfully applied for experimental investigations on different materials [35,52-53]. This approach is a compromise of using minimum load (comparable to the sintering stress), maximum resolution and a large number of experiments valid only in a small range of increased density. Theoretically, the load can be either tensile stress or compressive stress. However, until now, only compressive stress has been used in experiments. This is also the reason why this technique was often referred to as discontinuous sinter-forging [52-53,58]. It is worth mentioning that sintering parameters were for the first time measured in this work under tensile stress state.

3.4.3 Experimental design

Different sets of experiments were designed:

3.4.3.1 Prediction of onset condition for flash sintering

The specimens made of 10YDC-Batch1 were firstly heated with a heating rate of 5 K/min to 600 °C for 1 hour, and then heated with a heating rate of 30 K/min to 1200 °C, 1000 °C. During the experiment, a minimal load of 10 N (i.e. 0.15 MPa) was used to maintain the contact between the platinum electrode and the sample. Once the isothermal temperature was reached, the furnace was held under the temperature. Subsequently, the applied dc electrical fields were increased until the onset of flash sintering. The current limit was set up to 1.5 A for 10 s as the signal of flash sintering. This current limit was given based on the assumption that specific current density for the onset of flash sintering is about 34 mA/mm^2 [17]. However, the definition of this power peak is a very subjective assumption, for example, in the investigation of onset of flash sintering for gadolinium doped Ceria, Hao *et al.* [175] suggested the specific volume power dissipation for the onset of flash sintering is about 10 mA/mm^2 while Spiridigliozzi *et al.* [176] defined he specific volume power dissipation for the onset of flash sintering about 148 mA/mm^2.

3.4.3.2 Influence of electrical fields on the sintering parameters

The experiments were conducted using the custom made loading dilatometry in Jülich. All the free sintering experiments were conducted with 10YDC-Batch1 under a minimal load of 10 N (i.e. 0.15 MPa) to maintain the contact between the electrodes and the specimen. All these measurements were conducted under three different conditions of applied electrical fields E_{rms} = 0 V/cm, 14 V/cm and 28 V/cm with a frequency of 50 Hz. Three different sets of experiments were designed to investigate the influence of electric field on sintering parameters. The true longitudinal axial strain was used considering the large deformation during the sintering. The sintering strain rates ($\dot{\varepsilon_z}$ and $\dot{\varepsilon_r}$) of interest were then calculated using the derivation of an exponential fitting to curves of strain vs. time. The quality of the fitting was considered adequate when the coefficient of determination, R^2, was larger than 0.999.

The cycles were performed on samples freely sintered to a desired density of 70 %, 75 %, 80 % and 85 % during the isothermal period (1208 °C and 1188 °C) under three different conditions of applied electrical fields E_{rms} = 0 V/cm, 14 V/cm and 28 V/cm with a frequency of 50 Hz and then subjected to a constant pressure of 1.2 MPa or 2.4 MPa. This mechanical loading was applied within a 3 % increase of relative density. These two pressure values were chosen so that the anisotropy introduced by uniaxial mechanical load can be minimized. More than 20 experiments were done, including two complete free sintering experiments at the same temperature with the holding time of 2 h.

3.4.3.3 Confirmation of symmetric behavior under tensile loading

All these measurements were conducted with 01YDC-Batch3 under the electrical fields E_{rms} = 14 V/cm with a frequency of 50 Hz.

I. Discontinuous loading-dilatometry cycles with dog-bone shaped samples under tensile stress

The dog-bone shaped samples were heated under a constant load of 1 N (tensile stress in the gauge area: 0.1 MPa) to maintain the tension and with a heating rate of 15 K/min to 900 °C and then 20 K/min to 1150 °C. Due to the size of furnace, the true heating rate was 12.7 K/min ± 0.07 % until 900 °C and 11.4 K/min ±0.1 % until 1150 °C. Discontinuous loading-dilatometry cycles were performed on the samples after 35 min when the thermocouple near the specimen reached 900 °C, and then subjected to a constant load of 4 N, 8.2 N and 17 N (i.e. 0.44 MPa, 0.91 MPa and 1.9 MPa). The mechanical load was applied for 5 min. More than 20 experiments were done.

Two complete free sintering experiments with the holding time of 2 h were also conducted. The free sintering experiments were conducted with fully densified sample to exclude the thermal expansion of the testing system, because the tensile extension recorded during the experiment contained the thermal expansion of the whole system as well.

II. Discontinuous loading-dilatometry cycles with bulk samples under compressive stress

The cycles were performed on samples freely sintered with a heating rate of 13 K/min until 900 °C, and then 11 K/min until 1150 °C. The mechanical loads, 70 N and 137 N, yielding a pressure of 1.2 MPa and 2.4 MPa, were applied to the specimen when the relative density of the specimen reached a desired density of 80 %. This mechanical loading was applied for 5 min.

3.4.3.4 Activation energy measurement

Free sintering experiments were conducted on bulk samples (10YDC-Batch3 and 01YDC-Batch3) under a constant load of 10 N (i.e. 0.15 MPa) to maintain the contact between the electrodes. In order to define the activation energy under three different kinds of electrical fields: E_{rms}=0 V/cm, 14 V/cm and 28 V/cm with a frequency of 50 Hz. Isothermal heating experiments were conducted under each electrical field with a heating rate of 30 K/min and a holding time of 2 h. The detailed set-up is shown in the following table.

Table 4: Set-up of furnace temperatures under different electrical fields (°C).

Material	**Electrical fields [V/cm]**			**Electrical fields [V/cm]**			**Electrical fields [V/cm]**		
	28 V/cm			14 V/cm			0 V/cm		
01YDC	1050	1100	1150	1050	1100	1150	1050	1100	1150
10YDC	1050	1100	1150	1050	1100	1150	1050	1100	1150

3.5 Electrochemical impedance spectroscopy

The ionic conductivity of the specimens are measured via impedance spectroscopy (EIS) (Novocontrol Technologies, Montabaur, Germany), consisting of an Alpha-A High Performance Modular Measurement System offering a broad frequency range of 3×10^{-5} Hz – 4×10^{7} Hz with an amplitude of 30 mV from RT to 1600 °C with the resolution of 0.1 °C under air atmosphere conditions.The temperature of the specimens was measured using a type-S thermocouple. The resistances and capacities were extracted from the impedance spectra with the ZView program (version 3.5d, Scribner Associates, Inc., Southern Pines, USA). The working principle of IS is to give the system a small AC signal with different frequencies, because EIS is based on the linearization of nonlinear electrochemical equations [157]. Subsequently, the in and out-of-phase components of the voltage across the sample are measured. By dividing these components by current, the resistive and reactive (capacitive/inductive) components can be obtained. As the measurement results, the real and imaginary components of the impedance are plotted as a function of frequency.

The electrical properties were measured using the disk samples (10YDC-Bacth2 and 01YDC-Batch2) under potential sinusoidal perturbations with a peak of 30 mV. The temperature range for the conductivity measurement for 10YDC was 200 °C – 350 °C, while the temperature range for 01YDC was 400 °C – 650 °C. The upper temperature limit was given by a minimal sample resistance in order to analyze the impedance spectrum.

3.6 Microstructure analysis

Microstructure observation was performed on polished samples. The cross section of the samples were ground firstly with SiC papers with grits from 800 grit to 1200 grit using water-based lubricant and then polished with pastes of 3, 1 and 0.05 μm diamond particles. Subsequently, the samples were thermally etched at a temperature 50 K lower than the sintering temperature for 1 hour.

Micrographs were taken with a high-resolution scanning electron microscope, Zeiss Ultra55, (Carl Zeiss Microscopy, Oberkochen, Germany). As samples are electrically non-conductive, a 1 nm thick coating of Pt was deposited on the surface of the sample.

3.6.1 Grain size analysis

The obtained SEM images were imported into an image processing software (analySIS pro, Hamburg, Germany). After contrast enhancement, the threshold was set to separate the pores and grains. Finally, the arithmetic mean of all diameters of a grain was calculated by the software for angles in the range 0° through 179° with step width 1°. Subsequently, the D_{50} was calculated from the distribution of arithmetic mean diameter of each detected grain. In order to estimate the average 3D grain size from the mean 2D grain size obtained from the software, a factor of 1.6 was applied [177].

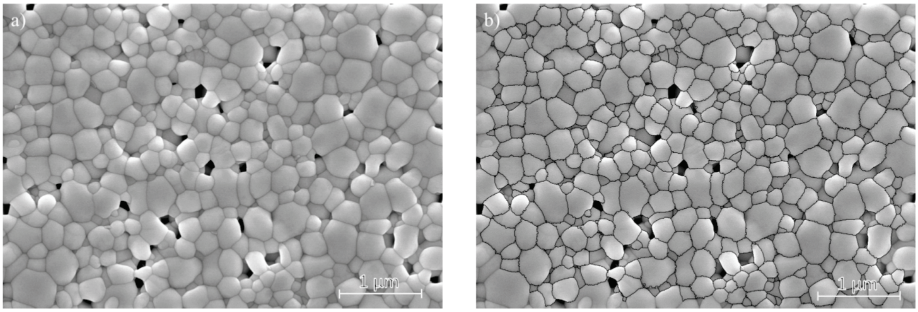

Figure 31: Image analysis process of the micrographs a) obtained micrograph b) generated grain boundaries using image processing software.

3.6.2 Pore characterization

Pores were also analyzed to quantify their properties. At least 1000 pores were investigated per sample. The pore orientation was quantified using the concept of cumulated pore lengths [178-179] in which the weighted pore length was analyzed as a function of the pore orientation angle. The calculation of cumulated pore length, k, was calculated as follows:

$$\mathrm{k} = \frac{\sum_i (d_i \varepsilon_i sin\theta_i)^2}{\sum_i (d_i \varepsilon_i cos\theta_i)^2} \tag{3-7}$$

where i denotes the ith pore in the microstructure. ε_i is the maximum ratio of larger and shorter of a bounding rectangle for the pore, d_i is the larger diameter and θ_i is the orientation angle. An equal distribution of cumulated pore length in polar coordinates to an isotropic microstructure.

3.6.3 X-ray absorption spectroscopy

X-ray absorption spectroscopy (XAS) is a widely used technique for determining the local geometric and/or electronic structure of matter by analyzing the absorbed spectra. The working principle of the XAS is based on the interaction between the high energetic X-ray and the deep-core electron. When the input energy is higher enough, the deep-core electron is excited and propagates away, leaving a core hole behind. Subsequently, a higher-lying electron decays into the core-hole and emits a photon. This interaction correlates with a sharp change in absorbed spectra.

A typical XAS curve is usually divided into two regions (Figure 32) : X-ray absorption near edge structure spectroscopy (XANES) extending until 50 eV after the absorption edge and extended X-ray Absorption Fine Structure (EXAFS), representing the area after XANES until 1000 eV. XANES can reveal the short range order of the microstructure with a good structural model. On the other hand, XANES represents the local structure of coordinated atoms. Moreover, the position of edge shows the oxidation state of the atom.

In this work, the XANES was analyzed with 10YDC-Batch1 freely sintered under E_{rms} = 0 V/cm and 28 V/cm with a frequency of 50 Hz to verify the *ex situ* effect of electrical fields on oxidation states of Ce. XAS techniques were used to evaluate the electronic structure and the chemical bonding of Ce-M-edge in their local environment.

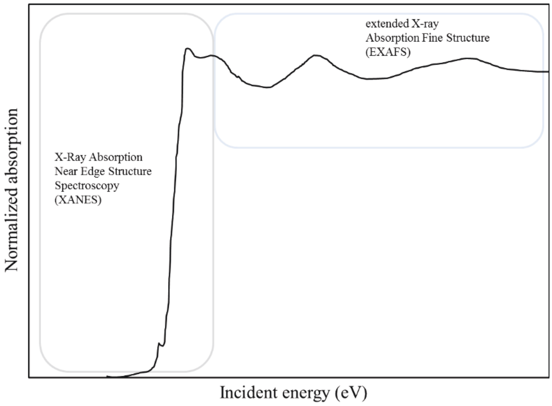

Figure 32: Separation of regions of XANES and EXAFS in a typical XAS experimental results.

4.Results and Discussion

4.1 Material characterization

4.1.1 Particle size distribution and powder morphology

The sintering behavior of powder compact is affected by the powder's particle size distribution. In order to investigate, PSD was used to analysis the particle size distributions of the Batches used in this thesis.

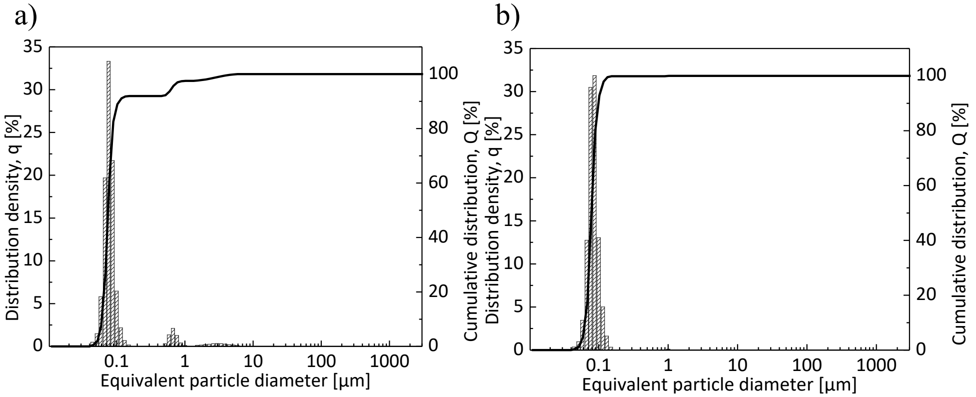

Figure 33: Particle size distribution of 01YDC-Batch1 a) as-delivered b) after calcination and milling.

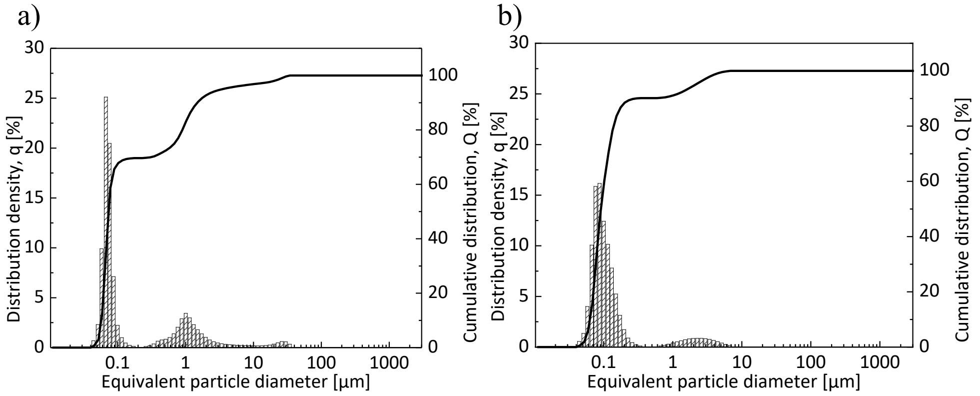

Figure 34: Particle size distribution of 10YDC-Batch1 a) as-delivered b) after calcination and milling.

The particle size distributions of 01YDC-Batch1 and 10YDC-Batch1 are shown in Figure 33 and Figure 34, respectively. Agglomerates, rather than the primary particle size, dominate the size distribution. After calcination and milling, the particle size distribution of both materials changed from bimodal to the unimodal distribution, which indicated a more homogeneous distribution. However, there were still hard agglomerates left in the case of 10YDC powder (Figure 34b). In terms of 01YDC, all the hard agglomerates were broken via milling, as illustrated in Figure 33b. In conclusion, this grinding and milling method worked effectively in powder homogenizing for Batch1.

The powders of Batch 2 and Batch 3 powders were similar. Examples of the particle size distributions of 01YDC-Batch2/3 and 10YDC-Batch2/3 are shown in Figure 35 and Figure 36. Compared to the first Batch, the second and third batches distributed more bimodally. On 10YDC-Batch3, the calcination and milling method was also applied, which results are shown in Figure 37. The bimodal distribution was slightly improved but still a relatively large number of hard agglomerated remained. These results imply that the calcination and milling method is not effective for Batch2/3 in powder homogenizing. The Batch variation is probably linked to the fluctuating production process. Thus, the powders should be either self-produced or ordered from other producers to solve this problem.

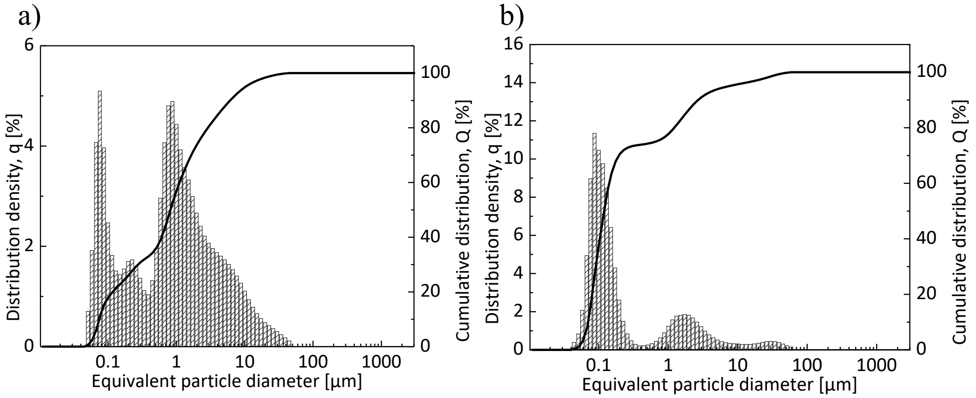

Figure 35: Particle size distribution of YDC-Batch2 a) 10YDC as-delivered b) 01YDC as-delivered.

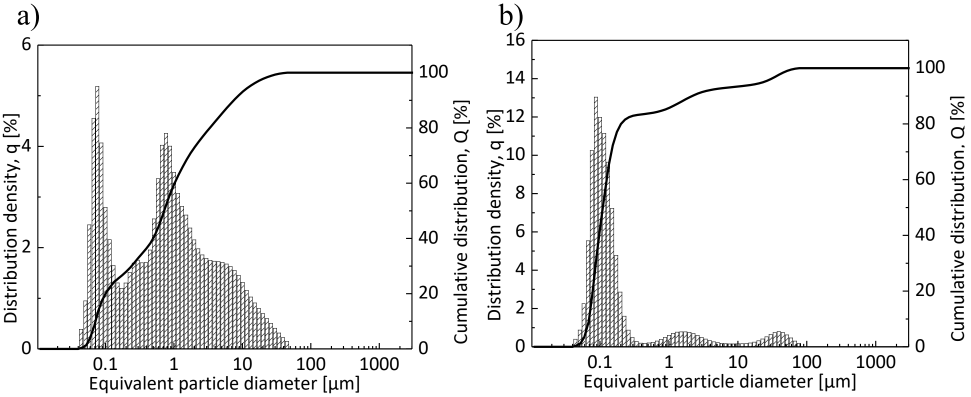

Figure 36: Particle size distribution of YDC-Batch3 a) 10YDC as-delivered b) 01YDC as-delivered.

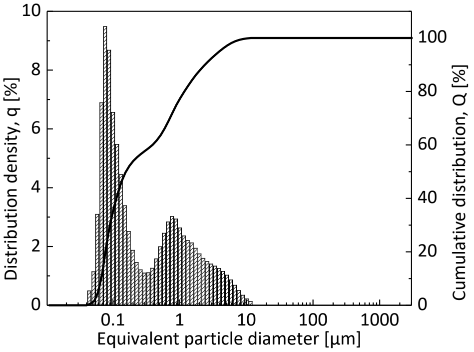

Figure 37: Particle size distribution of 10YDC-Batch3 after calcination and milling.

The morphology of the powder was also observed using TEM conducted in Ernst Ruska-Centre for Microscopy and Spectroscopy with Electrons (ER-C) at Forschungszentrum Jülich. The results are shown in the following figures.

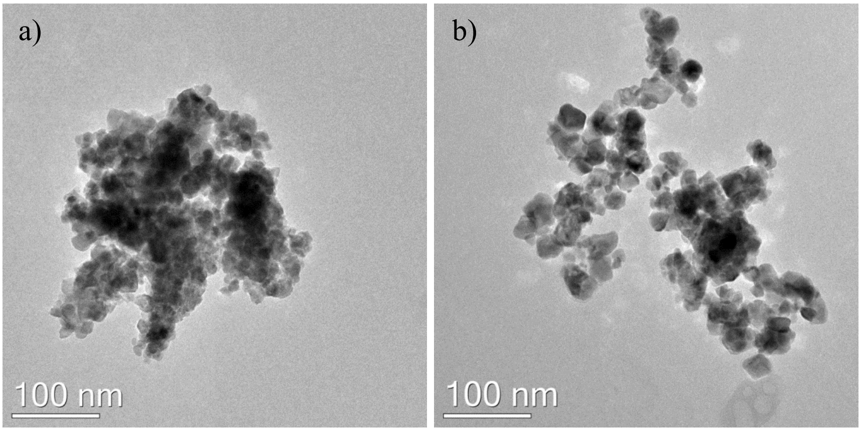

Figure 38: TEM images of as-delivered YDC-Batch1: a) 10YDC b) 01YDC.

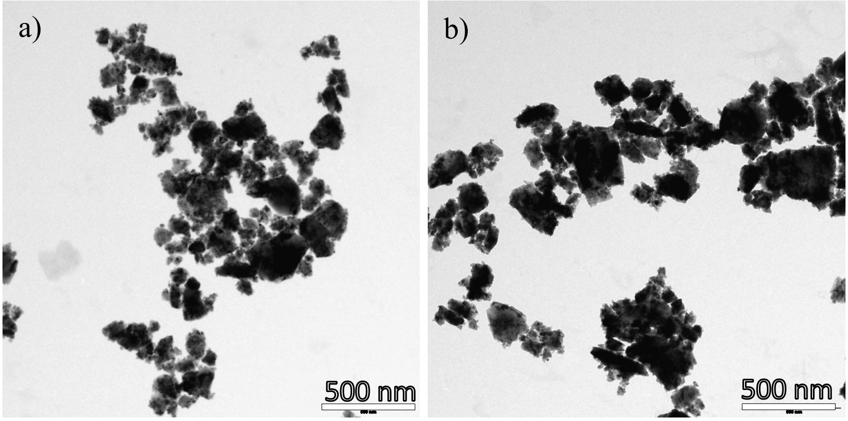

Figure 39: TEM images of YDC-Batch1 after calcination and milling: a) 10YDC b) 01YDC.

Figure 38 and Figure 39 show that the powder tends to form large agglomerates even after the calcination and milling. In terms of Figure 39a, the average particle size is 0.08 µm, which is comparable to D_{50} (0.08 µm) in PSD (Figure 34b). That is to say, results from TEM agrees with PSD results and TEM pictures can also reveal information for the smaller agglomerates. However, the PSD (Figure 34b) results also exhibit a small amount of larger agglomerates (larger than 1 µm), which was not observed in TEM. This is probably due to the small amount of particles observed in TEM.

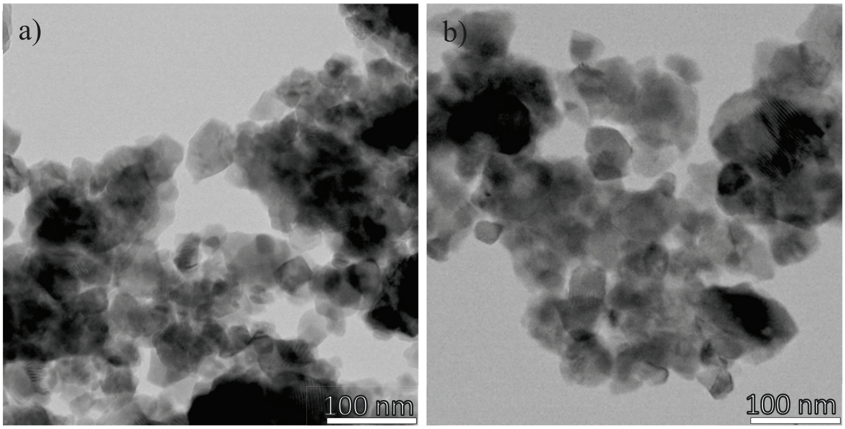

Figure 40: TEM images of as-delivered YDC-Batch2: a) 10YDC b) 01YDC.

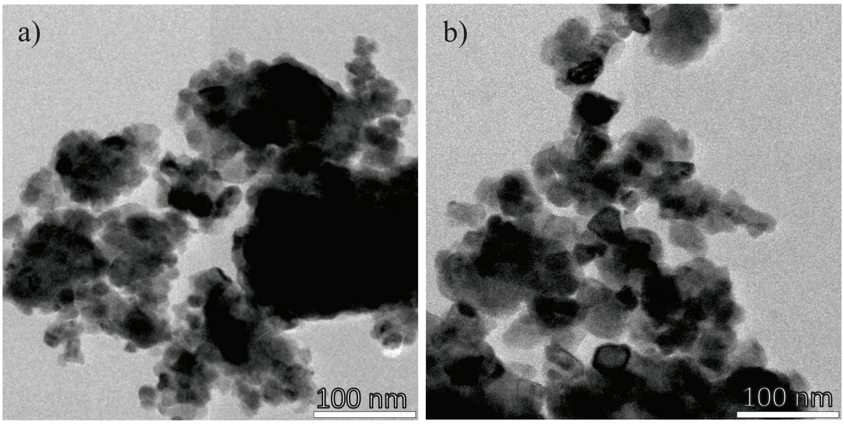

Figure 41: TEM images of as-delivered YDC-Batch3: a) 10YDC b) 01YDC.

As the same reason mentioned above, large agglomerates (larger than 1 µm) corresponding to the second peak in PSD (Figure 35 and Figure 36) was not observed in TEM of powder morphologies of Batch2 (Figure 40) and Batch3 (Figure 41). These two Batches of powder show a similarity: The proportion of agglomerates was higher in Batch2 and Batch3 than in Batch1 (Figure 38). Take Figure 40a as an example, the particle size (marked in green) is 0.07 µm, which is comparable to D_{50} for the first peak in PSD (Figure 35a).

4.1.2 Specific surface area

The results of the specific surface area are listed in Table 5.

Table 5: Results of specific surface area of YDC (*m^2/g*)

	Batch 1			Batch 2	Bacth 3	
Material	As-delivered	After calcination	After calcination and milling	As-delivered	As-delivered	After calcination and milling
01YDC	16.42	1.24	14.53	17.02	14.00	6.31
10YDC	20.62	1.59	16.93	19.9	19.18	6.42

The results with powders from Batch1 show how the BET changed with corresponding process. After the calcination of Batch 1 powders, agglomerates formed and the specific surface area decreased, After milling, the surface areas of Batch 1 increased, but were still smaller than those as delivered. In the case of Batch2/3 powders, even though the PSD was different from that of Batch 1, the BET results of the as-delivered powder were similar. It can be attributed to the small size of gas molecule, which makes physisorption possible even within the agglomerates. As explained above, the second and third batches distributed more bimodally and the calcination processes could turn soft agglomerates to hard agglomerates. The decrease of BET for Batch3 after calcination and milling also proves the formation of hard and large agglomerates in the powder, which agrees with the PSD results (Figure 37).

4.1.3 Phase composition

The single phase of the powder was confirmed with the XRD results illustrated in Figure 42.

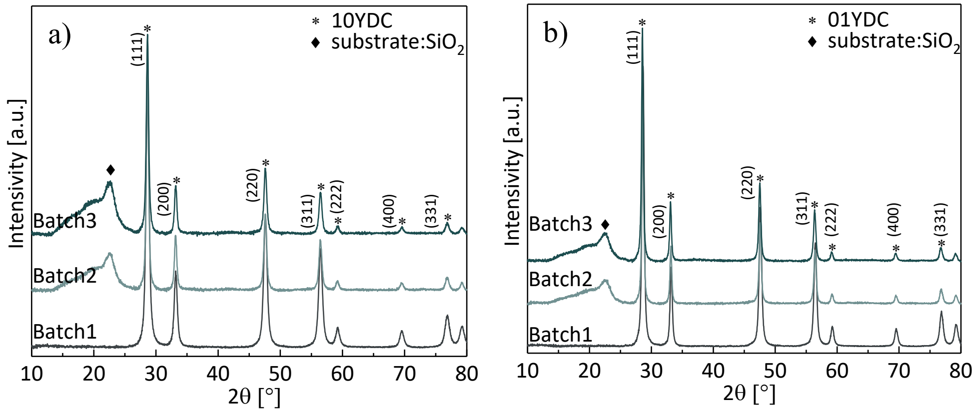

Figure 42: XRD diffraction diagram of the as-delivered powder a) 10YDC b) 01YDC.

In accordance with Figure 42, the powder is single phase with the stable fluorite structure. The detected phase near the edge of 25° is attributed to the substrate due to the small amount of powder on the substrate edge. The lattice parameter of YDC can be calculated according to the Bragg's law. The lattice parameter is 5.409 Å for 10YDC, and 5.411 Å for 01YDC.

In order to interpret the slight decrease of lattice parameter with increasing doping level, two competing aspects have to be considered: i) the ionic parameter of Y^{3+} (1.019 Å) is larger than that of Ce^{4+} (0.97 Å); ii) the decrease of lattice parameter due to the generation of oxygen vacancies. The decrease in lattice parameter accordingly to the doping level indicates that the second effect is more pronounced than the first one at RT. With increasing doping by Y, more oxygen vacancies are introduced according to Eq. 2-42. Gu *et al.* [180] reported that the lattice parameter of 20 mol % yttrium doped ceria is 5.406 Å. This result also follows the rule (higher doping level leads to smaller lattice parameter), and is in agreement with our results.

4.1.4 Chemical composition

The stoichiometry together with the purity level of the powder was measured with ICP-OES and the results are listed in Table 6.

Table 6: Results of the chemical analysis of 10YDC powders in atomic percent.

Element	Batch1 [%]	Batch2 [%]	Batch3 [%]
Ce	89.18	90.41	89.99
Y	10.10	9.34	9.47
Impurity element			
Zr	0.12	0.12	0.12
P	<0.02	0.06	0.06
Ca	0.0100	0.0400	<0.0004
Si	0.58	<0.02	<0.05

Table 7: Results of the chemical analysis of 01YDC powders in atomic percent.

Element	Batch1 [%]	Batch2 [%]	Batch3 [%]
Ce	99.12	99.58	99.26
Y	0.06	0.11	0.10
Impurity element			
Zr	0.15	0.12	0.16
P	<0.02	0.06	0.08
Ca	0.0100	0.0400	<0.0004
Si	0.64	<0.02	<0.06

The results show the amount of Ce and Y agrees with the nominal stoichiometry of 10YDC and 01YDC, with the difference of 0.4 %. In general, Zr is the impurity with the highest content and the content of Si is extremely high in Batch1.

The theoretical density of 01YDC and 10YDC is calculated on the base of stoichiometry together with the lattice parameter calculated from XRD results and reads [181]:

$$\rho_{th} = \frac{4}{A^3 N_a}\left[At_C M_C + At_Y M_Y + At_O M_O\right] \tag{4-1}$$

where ρ_{th} is the theoretical density, A is the lattice parameter, At_C, At_Y and At_O are atomic percentage of cerium, yttrium and oxygen, M_C, M_Y and M_O are atomic weight of cerium, yttrium and oxygen. The average theoretical density calculated for 10YDC and 01YDC are 6.983 g/cm^3 and 7.209 g/cm^3, respectively. Herle *et al.* [168] reported 6.991 g/cm^3 for 10YDC, which is in agreement to our results.

4.1.5 Conventional sintering behavior analysis

4.1.5.1 DTA-TG

DTA-TG experiments were conducted for a better understanding of ceria's oxidation at RT, as shown in Figure 43. Ceria powder was at first sintered under the Ar atmosphere, during which ceria got easily reduced, resulting in a mass decrease. And then after the temperature got stabilized at RT, air was purged into the system. The absorption of oxygen occurred immediately after the purge, as indicated by the sharp peak in the DTA curve and by the rapid mass increase in the TG curve. Afterwards, heat-treatment of the second period was done under air atmosphere. No obvious mass reduction was observed in the second period, different from the first one.

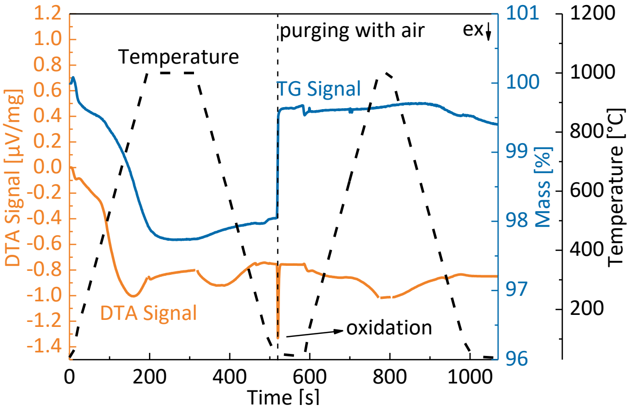

Figure 43: The DTA/TG experiments with 10YDC sintered with the first period (Ar) and the second period (air). The air is purged into the system at RT.

The DTA-TG experiments proved that the re-oxidation of ceria is fast even at RT. This result also indicates that cerium's reduction state at high temperature cannot be kept after the sample's cooling down to RT, even with a high cooling rate. Thus, it is not likely to detect reduced cerium induced by high temperatures or fields *ex-situ*, i.e. after sintering.

4.1.5.2 Dilatometric analysis

Preliminary dilatometric analyses were conducted on cylindrical samples to define the temperature range used for the following viscosity measurements. Experimental procedure for the analyses is described in Section 3.4.1.1.

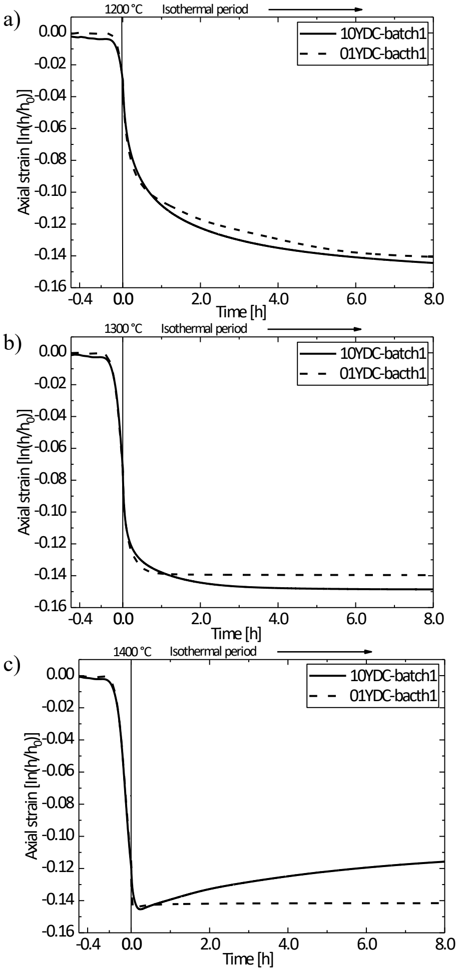

Figure 44: True axial strain-time curves of 10YDC and 01YDC after calcination and milling under a) 1200 °C, b) 1300 °C c) 1400 °C.

Table 8: Results of relative density of green body measured geometrically, final relative density of sintered specimens by Archimedes' principle under different isothermal temperatures for 10YDC for 8 h.

Isothermal temperature[°C]	Relative density [%] (green body)	Relative density [%] (after sintering)
1300	56.5%	96.0%
1400	57.8%	90.0%
1500	58.2%	84.5%

As illustrated in Figure 44 and Table 8, sintering rates of both powders increase with isothermal temperatures. The sintering rate of 01YDC is slightly higher than that of 10YDC. Sintering behaviors of 01YDC and 10YDC at 1200 °C and 1300 °C are similar, but the axial strain of 10YDC decreases during the isothermal period at 1400 °C while the axial strain of 01YDC keeps constant. The results in Table 8 imply a decrease in relative density when the isothermal temperature increases.

The difference in the sintering rate between two powders can be explained from the following two aspects: i) difference in doping level. The retardation effect of dopants was also observed with yttria doped ceria (2.5 at.%-35 at.%) [182] and samaria doped ceria (0 at.%-20 at.%) [183]. At higher doping levels, formation of defect complexes such as $(Y_2V_O)^x$ and $(YV_O)^{\cdot}$ are expected on the consideration of static electrical attraction and elastic energy. This may slow down the cation mobility and thereby a lower densification rate [136,182]. ii) particle packing effect. PSD of 01YDC exhibits a more homogeneous distribution than that of 10YDC (Figure 33 and Figure 34). A homogenous distribution of the powder improves sintering behaviors.

It is worth noting that the de-densification behavior for in 10YDC when the temperature reaches 1400 °C (Figure 44). The porosity increased when the isothermal temperature increased from 1300 °C (Figure 45) to 1400 °C (Figure 46).

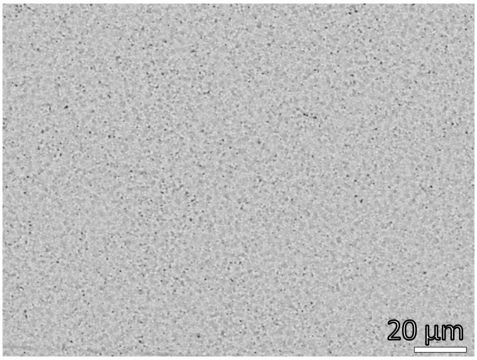

Figure 45: The SEM graphs of 10YDC sintered with the isothermal temperature of 1300 °C.

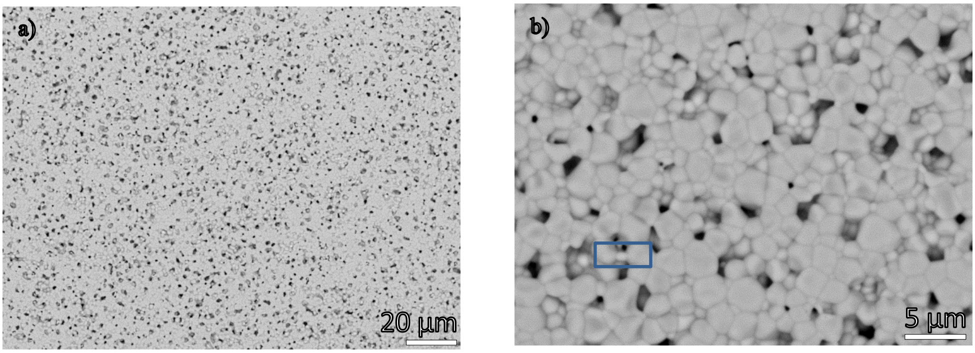

Figure 46: The SEM graphs of 10YDC sintered with the isothermal temperature of 1400 °C. a) general microstructure b) detail with the blue marked area: a typical structure observed in de-densifying microstructure.

Firstly and quite obviously, the question arises: ‘I*s the de-densification related to the reduction of ceria with a higher doping level?*’ In other words, higher porosity is introduced by oxygen release under high temperature [153,183]. In order to answer this question, a DTA experiment with MS was performed. As shown in Figure 47, no oxygen was released from the sample during the isothermal period, because no peak in the DTA signal, suggesting no endothermic reactions happened during this period. However, another possibility exists that the oxygen loss is a continuous process, in which case no peak will be observed. Even if there is a continuous oxygen loss, the oxygen loss, under the detect limitation of MS, should not be significant. Therefore, the reduction of cerium should not be the main cause of de-sintering phenomenon.

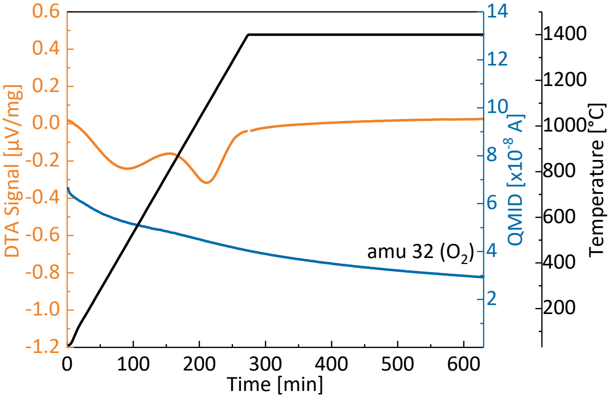

Figure 47: The DTA together with mass spectroscopy signal of oxygen of 10YDC sintered with the isothermal temperature of 1400 °C under air atmosphere.

Another explanation is related to the heterogeneous powder distribution. De-sintering phenomenon during constrained sintering was reported by Heinz *et al.* [184], due to the biaxial constraint on the film. As for a bulk specimen during the late intermediate stage or final of sintering stage, when only part of the specimen reaches a high relative density due to inhomogeneous sintering. Under this condition, the less densified part of the specimen is under a constrained sintering condition, e.g. under tensile stress.

In this work, de-sintering happened during the isothermal period after the relative density reached 95 % (Figure 44), i.e. the pore network turned into isolated pores. At this point, the question becomes '*why it only happens for 10YDC not 01YDC?*' A difference between the two kinds of samples is that the 01YDC is more homogenous than 10YDC, according to PSD shown in Figure 33 and Figure 34. The pore coarsening happen when the mass of small grains is redistributed into large grains (as illustrated in Figure 5). As a result, the small grains are absorbed and these large grains would be separated from each other, thereby the so-called de-sintering happened [27]. As an evidence for this theory, structure similar as illustrated in Figure 5 was found in the marked area in Figure 46b. The co-existing of the densified area together with the partly densified area is due to the inhomogeneity of the powder (Figure 34b). This explains why de-sintering only existing in 10YDC, which has bimodal distribution even after calcination and milling; while the 01YDC has a unimodal distribution. In order to confirm the theory, further investigation should be planned to observe the microstructure before and after the de-densification.

Then the question becomes '*why it only happens at 1400°C for 10YDC?*' The pore coarsening, i.e. the sweep of grain boundary through small grains require the grain boundary movement. The grain boundary movement is retarded by the solute drag effect, i.e. the inhibition effect of Y^{3+} and defect complexes on grain boundaries. Thereby, the grain growth, as well as the redistribution of small grains, is retarded. Thus the grain boundaries start to move only with a higher temperature, when the grain boundary mobility is high enough to get rid of the solute drag. At this temperature, the mechanisms described above take place and de-sintering happens. The further decrease of the relative density at 1500 °C (Table 8) is a proof of the existence de-sintering at temperature higher than 1300 °C when the grain boundary mobility is high.

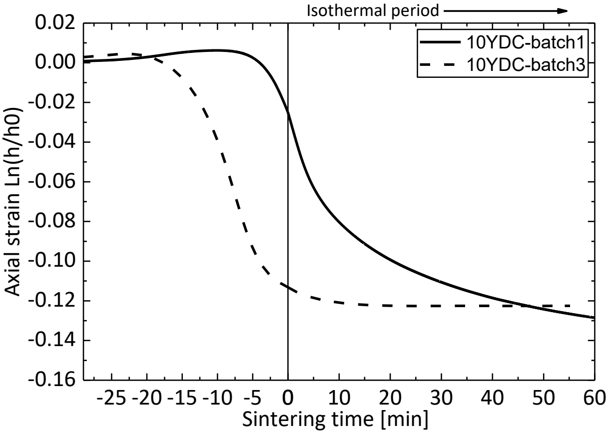

Figure 48: True axial strain-time curves of 10YDC-Batch1 after calcination and milling and 10YDC-Batch3 after calcination and milling at the isothermal temperature of 1200 °C.

Therefore, de-sintering happens under the following two conditions: i) different grain sizes due to heterogeneous powder distribution; ii) the grain boundary mobility is high enough for the redistribution of small grains. The origin of this phenomena is the inhomogeneity of the powder. In addition, this inhomogeneity hinders the densification by lowering the driving force under Energetic considerations, but increase the driving force for the grain boundary sweeping through the small grains due to a larger grain size difference. The inhomogeneous powder of 10YDC-Batch3 (after calcination and milling) as observed to stop shrinking directly when the isothermal temperature is reached at the temperature of 1200 °C in contrast to 10YDC-Batch1 (after calcination and milling) with a continuous densification behavior under this temperature (Figure 48). This is because of an even more inhomogeneous particle size distribution for 10YDC-Batch3, as shown by PSD results in Figure 34b (10YDC-Batch1) and Figure 37 (10YDC-Batch3). Therefore, the same calcination procedure turns out to be not suitable for 10YDC-Batch3.

4.2 Temperature Distribution

As introduced before, the sample temperature is the main issue to be addressed. Nowadays, the most frequently used indirect method for sample temperature calculation is the black radiation theory [185] or the modified black radiation theory [85,186]. In the simplest case, the total resistance of the specimen is the sum of the resistance of bulk, R_B and of the grain boundary, R_{GB}. Therefore, the power, W, dissipated in the specimen is as follows:

$$W = \frac{V^2}{R_C + R_{GB}} \tag{4-2}$$

Thereby, the approximate increase of the temperature of the specimen can be calculated according to the black radiation theory as follow:

$$W = 4A\varepsilon\sigma_{black}({T_s}^4 - T^4) \tag{4-3}$$

where T_s is the specimen temperature, T is the furnace temperature, W is the Joule dissipation of electrical energy, A is the total surface of specimen, ε is the emissivity, which is 0.98 and σ_{black} is the black body radiation constant, which equals to 5.67 x10^{-8} Wm^2/K^4 [185].

In order to measure the temperature directly, the most frequently used methods are infrared cameras [187] and pyrometer [4] which only provide temperature values of the sample surface. The inner temperature of the sample can be much higher if massive and rapid Joule heating is present. This issue hinders a clear separation of thermal and athermal effects. In order to clarify the problem, the sample temperature was measured using a thermocouple inside the sample in our work (section 3.3.2) using 10YDC-Batch1 after calcination and milling. In the following part, the results of temperature measurements using thermocouples are discussed, and compared with the measurements via the IR camera. Finally, the experimental measurements are compared with the simulation results.

4.2.1 Experimental measurements of temperature

The corresponding temperature inside the sample (T2) as a function of the furnace temperature (T1) for different electrical field strengths for 10YDC-Batch1 is plotted in Figure 49a. As an illustration of the temperature inhomogeneity, the difference between the sample temperature (T2) and the temperature near the sample surface (T3) as a function of furnace temperature (T1) is shown as well (Figure 49b). The effect of Joule heating under E_{rms} = 14 V/cm is negligible. However, electric field strengths higher than 14V/cm introduce an obvious temperature increase inside the sample. Smaller heat radiation at lower furnace temperature (1100 °C) leads to the highest temperature difference between T2 and T3, especially at higher electrical field strengths. This difference decreases when the furnace temperature increases.

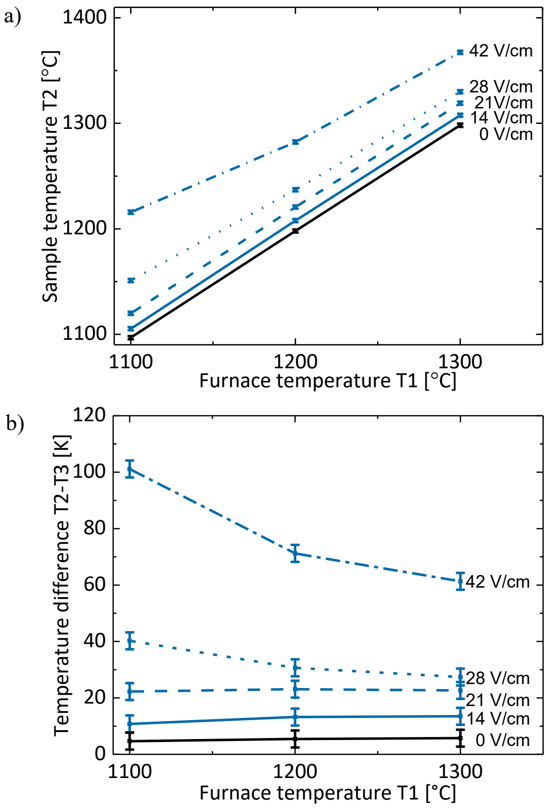

Figure 49: a) Inner sample temperature (T2) vs. furnace temperature (T1) under different electric fields for 10YDC. b) Difference between sample temperature (T2) and temperature near sample surface (T3) vs. furnace temperature (T1) under different electric fields for 10YDC.

The temperature difference between sample temperature and furnace temperature measured via IR camera is shown in Figure 50. The temperature increase for 01YDC is smaller than that for 10YDC. The smaller temperature increase is related to the lower conductivity, and therefore a lower Joule heating effect. This difference increases accordingly to the increasing electrical field strength.

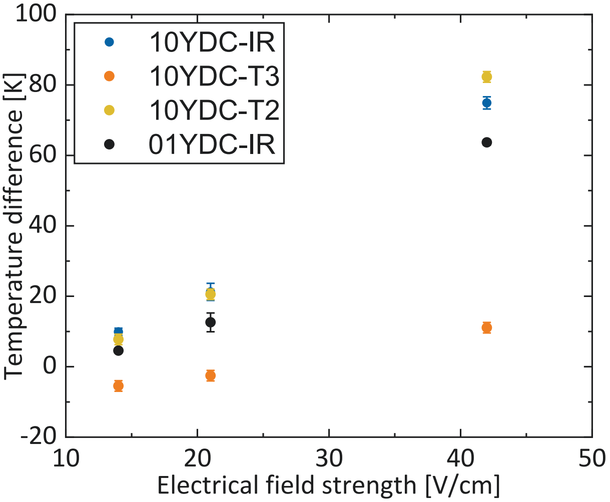

Figure 50: Difference between sample temperature and furnace temperature measured via IR camera with 10YDC and 01YDC, temperature difference between sample inner temperature (T2) and furnace temperature measured by thermocouple of the specimens of 10YDC, and temperature difference between temperature near sample surface (T3) and furnace temperature measured by thermocouple of the specimens of 10YDC with the isothermal furnace temperature of 1200 °C under E_{rms}=14 V/cm, 21 V/cm and 42 V/cm.

The measurements using IR are in good agreement with specimen temperature (T2) obtained using thermocouples. However, the surface temperature (T3) measured by thermocouple is lower than IR results, although they should theoretically be the same. The reason behind this discrepancy is because the measurements with the IR camera can be easily influenced by the thermal radiations of furnace and the heating elements. One heating element is located directly in front of specimen (Figure 27b) and this affects the measurements (shown in Figure 51).

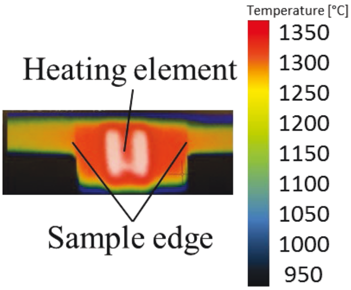

Figure 51: Illustration of the temperature measurement via IR camera.

On the base of the temperature measurements by thermocouples, isothermal furnace temperatures (T1) for the following sintering parameter measurements were adjusted to yield the same sample temperature of T2 (Figure 52). With the current flowing through the specimens, the specimen temperature increased due to the Joule heating effect. Therefore, the furnace temperature was lowered in order to compensate this temperature increase. In this way, the sample temperature in the middle of the sample was kept constant (1208 °C±3 °C) under different electrical fields.

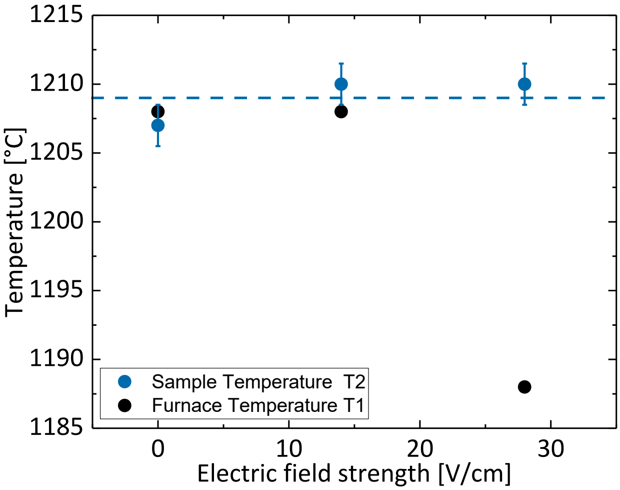

Figure 52: Experimental results of furnace temperatures (T1) to maintain the same sample temperature (T2) under different electric fields for 10YDC-Batch1.

4.2.2 Simulation results

The temperature within the densified sample was simulated using the thermo-electric finite element method for a complete understanding of the temperature distribution inside the sample. The comparison between the experimental sample temperature (T2) and the simulation results is plotted in Figure 53. The given simulated temperature is the maximal specimen temperature of the simulation. In the model, the symmetrical plane represents the whole cylindrical specimen. The simulation results are in a good agreement with T2 of the experiments.

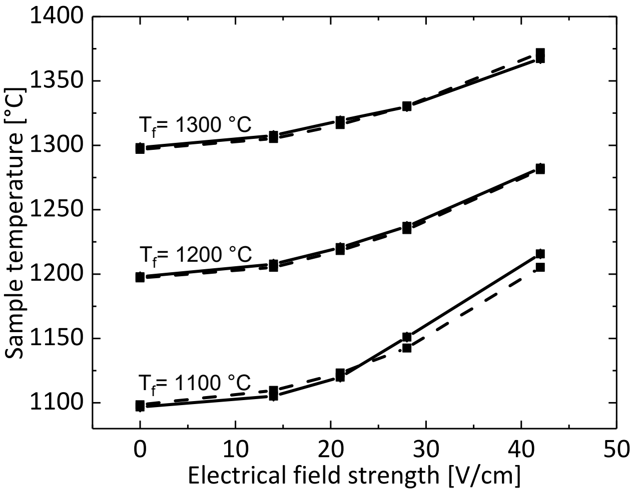

Figure 53: Comparison of sample temperature between simulation (dash lines) and experimental results (solid lines) for 10YDC-Batch1.

The temperature distribution with sample was also simulated under different electrical field strengths using FEA. An example is shown in Figure 54 for E_{rms} = 28 V/cm. With the constant T2 under higher electrical field strengths, the temperature of the bottom and top of the sample, and the side surface is lower than that in the condition with 0 V/cm due to heat conduction between the sample and alumina disks, and heat radiation. This leads to a lower average temperature (Table 9). The comparison of power density and current density between simulation and experiments is given in Table 10.

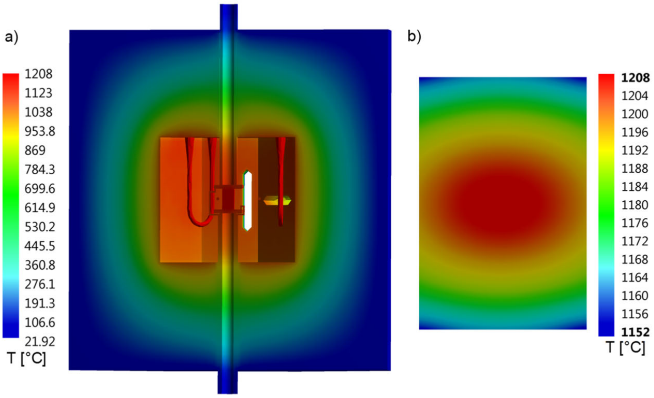

Figure 54: Simulation result of temperature distribution in loading dilatometry under E_{rms} = 28 V/cm with $T_{furnace}$ = 1188 °C: a) isometric view; b) detailed view of the sample.

Table 9: Simulation results of temperature distribution at symmetrical cross section.

Electrical field strength V/cm	$T_{average}$	T_{max}	T_{max}-T_{min}
	°C		
0	1204	1206	3
14	1202	1205	11
28	1189	1207	55

Table 10: Comparison of current density and power density between simulation and experiment.

Electrical field strength [V/cm]	**Current density [mA/mm^2]**		**Power density [mW/mm^3]**	
	simulation	experiment	simulation	experiment
14	11.7	11.2	16.2	16.8
28	20.0	21.1	55.4	60.0

It is important to note that both temperature measurements and simulation were conducted on the base of densified specimens with a higher conductivity and corresponding higher current and power density. It is therefore reasonable to assume that the highest temperature inside a densifying specimen is even lower, because the power and current density increase with densification and reaches its maximal value at the highest relative density. A further proof is that the current density during the measurement (Figure 58) is lower compared to the current density using dense specimens (Table 10), which is related to higher conductivity even though the electrical field increases due to the sample shrinkage,.

4.3 Prediction of the onset of flash sintering

To avoid the dramatic temperature increase caused by flash sintering, it is important to calculate the onset conditions of flash sintering. At a fixed furnace temperature, flash sintering event happens when the applied external electrical field reaches a limit value, and the thermal runaway model used is a model as a function of furnace temperature and external electrical field. Based on the calculation, the electrical fields can be chosen to avoid flash sintering during sintering parameter experiments. Figure 55 compares the onset of flash sintering as measured by experiments and the model described in section 2.4.2.1. As illustrated in Figure 55, no-flash conditions measured (denoted as black dots) happened under lower electrical fields compared to flash conditions (blue dots). The onset electrical field strength decreased with increasing furnace temperature. The flash conditions simulated agree well with the experimental results.

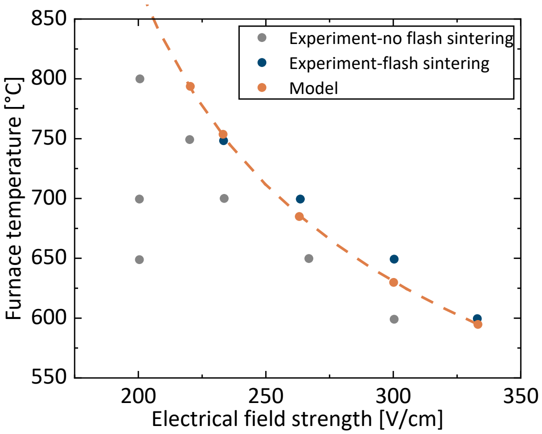

Figure 55: The Comparison of onset of flash sintering for 10YDC-Batch1 between the experiments and theoretical prediction using a thermal runaway model developed by Dr. Pereira da Silva from IEK1.

Therefore, the model was used to predict onset conditions under higher furnace temperatures. According to the model, the onset electrical field strength for 10YDC at the furnace temperature of 1400 °C was 140 V/cm. In this work, the furnace temperatures used were lower, ranging from 1000 °C to 1300 °C, and the applied electrical field in this work were also much lower than 140 V/cm. Higher electrical fields are required at lower furnace temperature to trigger the flash event. That is to say, our experimental conditions for 10YDC did not lead to a flash sintering. The onset electrical field strength for 01YDC, with a lower conductivity than 10YDC (see section 2.5.3), is theoretically higher onset electrical field than 10YDC at the same furnace temperature, because lower conductivities correspond to weaker macroscopic Joule heating effects. This implies that there is also no flash sintering for 01YDC under the experimental conditions.

4.4 Measurement of sintering parameters

4.4.1 Shrinkage during sintering

According to the experimental procedure described in section 3.4.3.2, the free axial and radial strains are plotted vs. time in Figure 56. The calculated axial strain rate vs. density under different electrical field strengths from the free sintering curves is illustrated in Figure 57, respectively, which were necessary for the following calculations of the sintering parameters. The absolute value of sintering rate under E_{rms} = 28 V/cm increases by a factor of about 2.6 compared to the condition without electrical field, whereas The absolute value of sintering rate under E_{rms} = 14 V/cm increase by a factor of about 1.6. The results show a field related improvement of shrinkage and sintering rate for a given density and a constant sample temperature, even under electrical fields lower than the ‘flash regime’ without any macroscopic Joule heating effect. This was achieved by keeping the highest temperature inside the densified sample constant under different electrical field (see section 4.2.1).

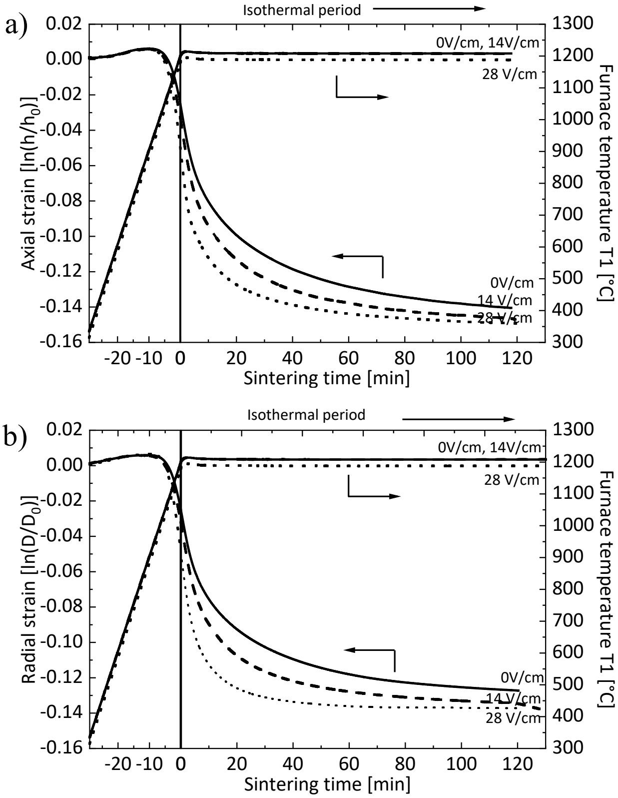

Figure 56: Axial and radial strain, furnace temperature as a function of time.

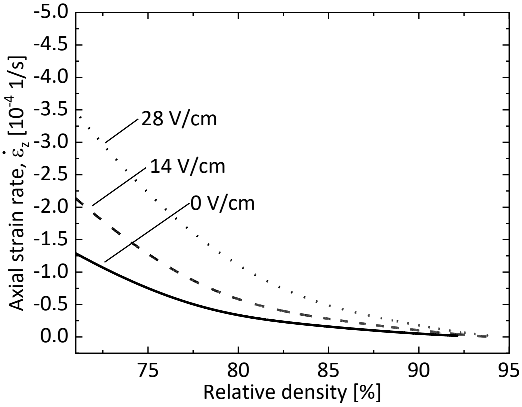

Figure 57: Axial strain rates with density under different electrical field strengths during isothermal periods (under E_{rms} = 0 V/cm, 14 V/cm and 28 V/cm).

The absolute value of power density and current density starts to deviate from 0 at around 860 °C. The power density under E_{rms}=28 V/cm increases by a factor of about 3.5 compared to the condition E_{rms}=14 V/cm, whereas the current density increase by a factor of about 1.6, which indicates that apparent conductivity of the specimen is constant under E_{rms}=14 V/cm and 28 V/cm. In contrast to the peak of power density appeared in flash sintering, the power density in our study increases until reaching a steady state during the isothermal period. In principle, onset of flash sintering correlates to a sharp powder density caused by the non-linear increase of material conductivity, which cannot be observed in Figure 58. The peak power density reported in flash sintering, which is typically 100-1000 mW/mm^3 [188]. This wide range indicates that there is no standard definition of the onset power dissipation. The highest power density under 28 V/cm is around 63 mW/mm^3 (Figure 58), significantly lower than the reported peak power density above In addition, the model predication for the onset flash sintering for 10YDC also confirms no flash sintering happened under these electrical field strengths (see section 4.3).

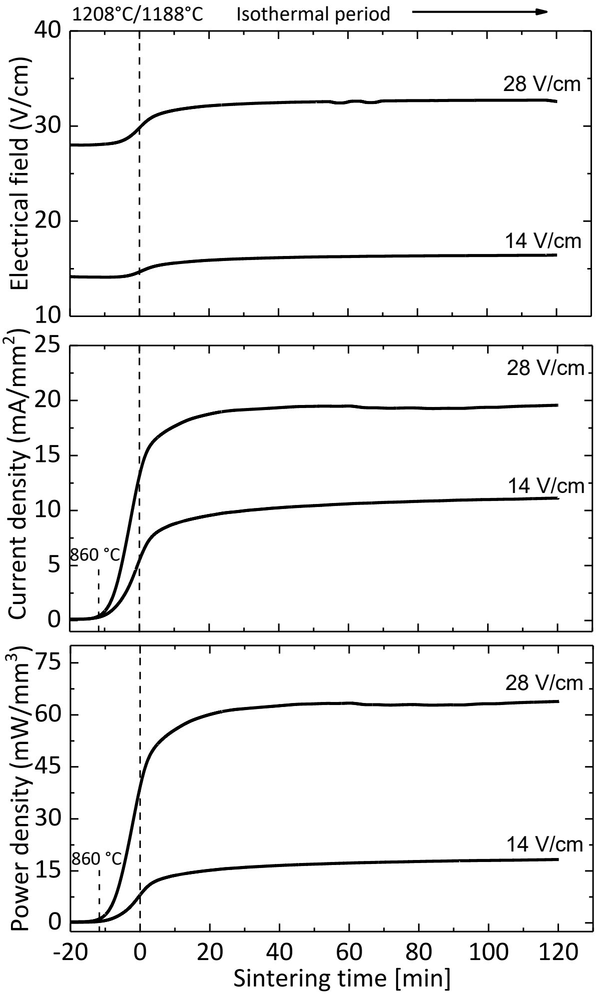

Figure 58: Electrical field, power density and current density over sintering time under E_{rms} = 14 V/cm and 28 V/cm.

In addition, in order to understand impact of field on the different diffusion paths during sintering (surface, grain boundary/volume), the sintering behaviour was observed under electric field (E_{rms}=14 V/cm) being switched off after the initial stage of sintering (strain ε=–3 %, Figure 59). The course of sintering continues comparable to the reference sample sintered completely without field. This implies that the improvement seen due to the field cannot originate from a change in the initial stage sintering (dominated by surface diffusion), but that the field is effective throughout the intermediate sintering stage, i.e. it also affects grain boundary diffusion.

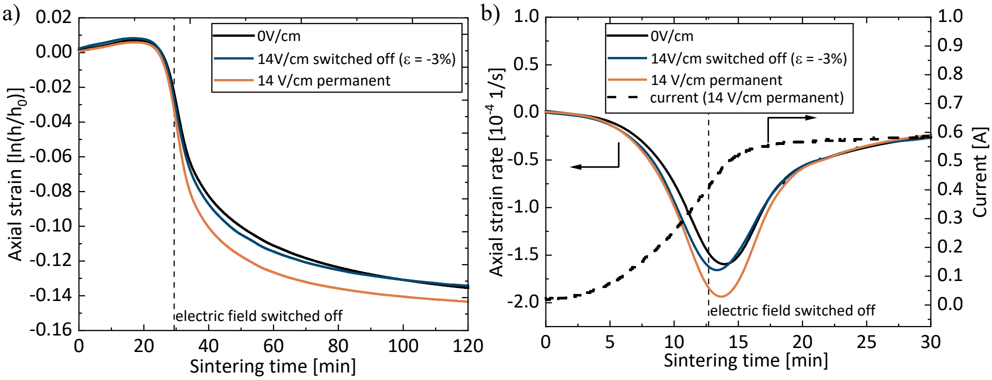

Figure 59: Sintering curves of field assisted sintering for 10YDC with the field switched off after the initial stage of sintering (under E_{rms} = 0 V/cm and 14 V/cm) with furnace temperature of 1208 °C. a) axial strain as a function of time.b) axial strain rates during isothermal periods.

4.4.2 Microstructure analysis

All sintering parameters are sensitive to grain sizes as well as porosity microstructure anisotropies. Therefore, it is of paramount importance to analyze the microstructures of the specimens.

4.4.2.1 Grain size analysis

- Specimens sintered under contacting electrical fields and compression conditions

The grain size of samples after discontinuous loading-dilatometry experiments under 2.4 MPa is depicted in Figure 60. No obvious grain growth is observed up to a relative density of 84 %. The grain sizes during sintering under different electrical field strengths do not significantly differ in this range considering the margin of error of the grain size analysis.

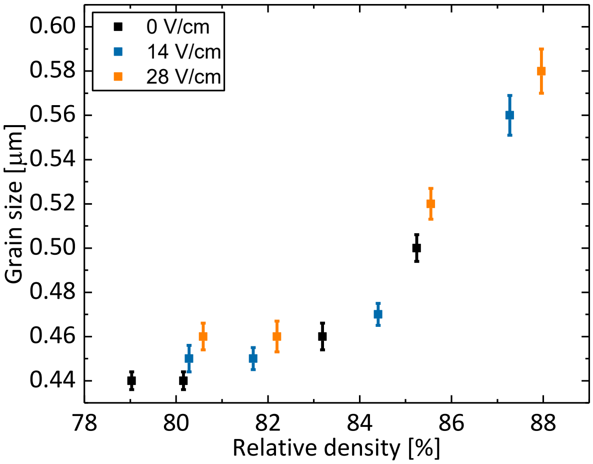

Figure 60: Sintering trajectory with the grain size of samples after discontinuous sintering forging experiments with E_{rms} = 0 V/cm, 14 V/cm and 28 V/cm as a function of relative density.

- Specimens sintered under contacting electrical fields and compression/tension conditions

To confirm the symmetric behavior under the tensile stress state, it is necessary to compare the microstructures of specimens before the load application to ensure that the uniaxial viscosities were measured for specimens of similar microstructure. As illustrated in Figure 61, no difference in the microstructure and grain size can be observed between specimens under compression and tension.

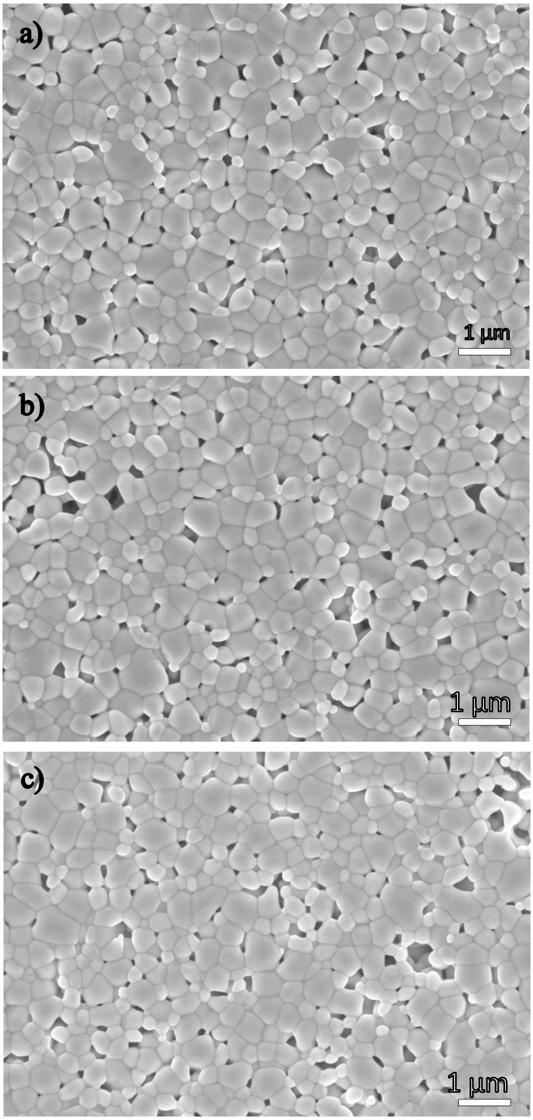

Figure 61: SEM images of the sintered specimens before the load application for a) compressive loading under 0 V/cm with the relative density of 79.5 %; b) compressive loading under E_{rms}=14 V/cm with the relative density of 79.6 %; c) tensile loading under E_{rms}=14 V/cm of 79.6 % relative density with the relative density of 79.5 %.

- Specimens sintered under non-contacting electrical fields

As shown in Figure 62-1, the grain size analysis for 10YDC of the SEM images implies a slight increase of grain size with longer holding time of 5 h (point a in Figure 62-1) with a factor of about 1.1. However, different electrical field strengths with the holding time of 2 h do not have significant influences on grain size, considering the margin of error of the grain size analysis (points b, c and d in Figure 62-1). The grain sizes of 01YDC in Figure 62-2 are about two times bigger compared to the grain sizes of 10YDC with the same holding time (points b, c and d in Figure 62-2), and the reason is the solute drag effect caused by the higher concentration of dopants in 10YDC which inhibit the grain boundary mobility. No difference in grain sizes for 01YDC with the holding time of 2 h under different electrical field strengths is observed, considering the margin of error of the grain size analysis (Figure 62-2).

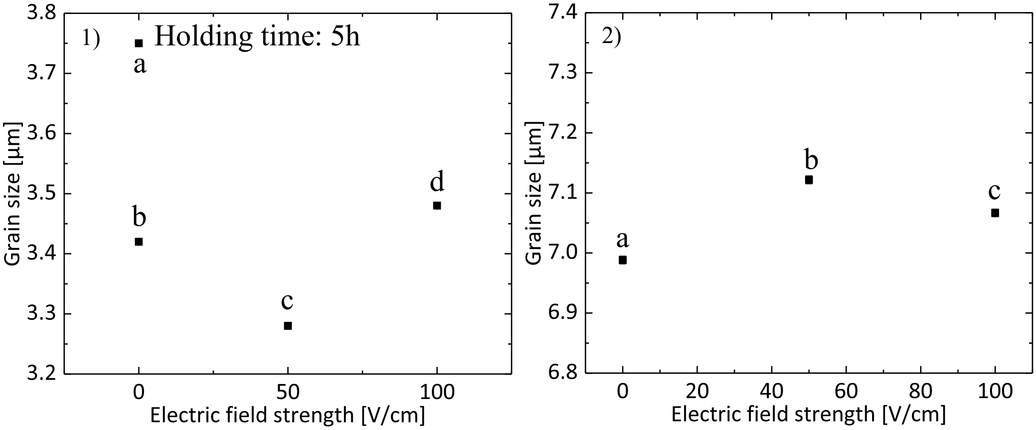

Figure 62: 1) Grain size analysis of sintered 10YDC-Batch3 at the furnace temperature of 1300 °C a) under 0 V/cm for 5 h; b) under 0 V/cm for 2 h; c) non-contacting electrical E_{rms}=50 V/cm for 2 h; d) non-contacting electrical E_{rms}=100 V/cm for 2 h. 2) Grain size analysis of sintered 01YDC-Batch3 at the furnace temperature of 1300 °C for 2 h a) under 0 V/cm; b) non-contacting electrical E_{rms}=50 V/cm; c) non-contacting electrical E_{rms}=100 V/cm.

4.4.2.2 Pore analysis

It is also important to confirm whether or not the microstructure remained isotropic in our case. Exemplary micrographs and pore orientation diagrams are given in Figure 63, where a mechanical pressure of 2.4 MPa was applied on the specimens with a relative density of 80 % under different electric field strengths. These data prove that discontinuously sinter forged samples remain isotropic after loading, which is required for the evaluation of sintering parameters of an isotropic material, according to Eq. (2-13 – 2-14).

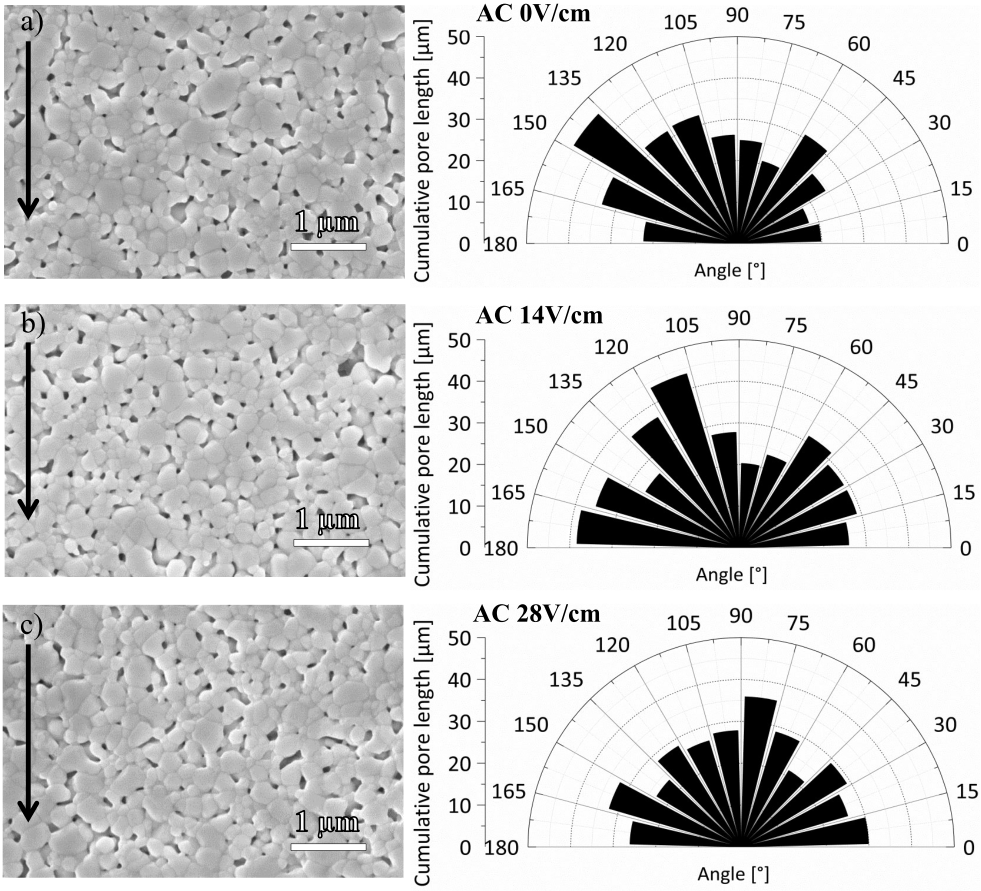

Figure 63: SEM pictures and pore orientation distribution of samples after discontinuous sinter forging experiments under 2.4 MPa, a) 0 V/cm; b) E_{rms}=14 V/cm; c) E_{rms}=28 V/cm, with the arrow denoting the electric and mechanical loading direction.

4.4.3 Uniaxial viscosity

4.4.3.1 Compressive condition under different electrical fields

During measurements of the sintering parameter, the linear relation between axial strain rate and uniaxial load was confirmed under electrical fields by applying three different loads at the relative density of 80 % under E_{rms} = 28 V/cm, as shown in Figure 64. The axial strain rate $\dot{\varepsilon}_z$ is presented as a function of the applied uniaxial stress for each density value. An example of the calculation of strain rate was listed in the appendix. For each linear fit in Figure 64, the uniaxial viscosity can be calculated according to Eq.

2-13. The resulting uniaxial viscosity as a function of the relative density is plotted in Figure 65. Taking the relative density of 80 % as an example, lower uniaxial viscosity was determined when an external electrical field was applied. Moreover, the influence of the electrical field on the sintering parameter is not directly proportional to the strength of applied electrical fields. At a fixed relative density (for example, 85 %), the uniaxial viscosity under E_{rms} = 14V/cm decreased by about a factor of 1.2, while E_{rms} = 28 V/cm prompted a decrease by about a factor of 2.4.

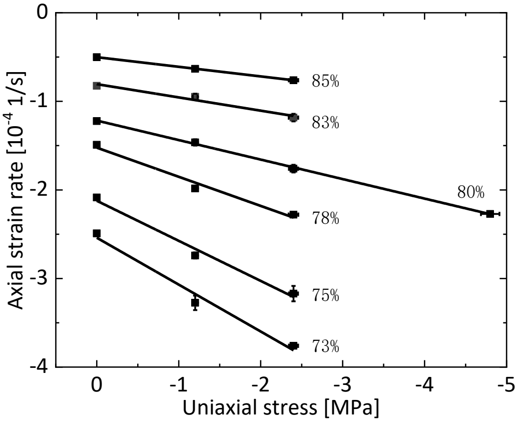

Figure 64: Axial strain rate as a function of uniaxial load for different relative densities at E_{rms} = 28 V/cm and $T_{furnace}$ = 1188 °C. A fourth load was applied at the relative density of 80 % to prove the linear dependency.

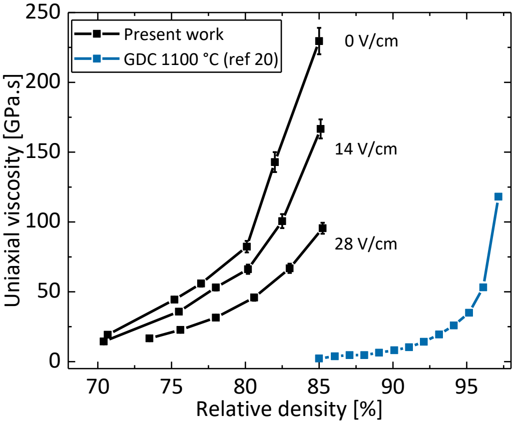

Figure 65: Uniaxial viscosity as a function of relative density using discontinuous loading-dilatometry. Comparison of the measured uniaxial viscosity as a function of relative density under different electrical fields in our work with the uniaxial viscosity of nanocrystalline gadolinium-doped ceria [52].

The application of electrical field also resulted in a decrease in the uniaxial viscosity even without any macroscopic Joule heating effect. According to thermal-electric finite element simulation, the average temperature (with the same T2) inside the sample is even lower under higher electric fields (Table 9).

According to Figure 65, the measured uniaxial viscosity first increases slowly with respect to relative density until it reaches 80%. Then, it increases progressively during further relative density increase. This behavior is observed for all conditions, i.e. with and without electrical fields. The dependency of the second term, $E_{p1}(\rho)$, according to Eq. 2-14, on relative density expresses the low uniaxial viscosity at relative densities lower than 90 % [48-51,189]. The effects of grain coarsening on uniaxial viscosity are expressed by the third term, $E_{p2}(d)$. It is proportional to the cube of the grain size for the case of grain boundary diffusion as the underlying diffusion mechanism [35].

The measured viscosity of nanocrystalline gadolinium-doped ceria sample at 1100 °C with an initial grain size of 35 nm also showed the same trend [52] (Figure 65). However, our measured results differ from the above mentioned work in the range of relative density. The difference can be attributed to a more homogenous powder compacts and smaller initial grain size in the already measured study, which not only lead to a lower uniaxial viscosity but also to a smaller grain size (around 300 nm at a relative density of 98 %). In addition, the different dopant element Y instead of Gd may also modify the sintering behavior.

The model proposed by Rahaman [50] introduced in section 2.3.2.1 was at first used to fit the uniaxial viscosity without electrical field. The parameter, a, was fitted to be 6.8 in this study. Chang used 10.5 for GDC [52], Rahaman reported 5 for ZnO and 2 for CdO [50]. In Beere's model, a is inversely proportional to the dihedral angle. Following this principle, the dihedral angle in this work should be larger than 116 ± 4 ° as reported by Chang for GDC [52]. Then, the uniaxial viscosities under the other two electrical field strengths were calculated using the same parameters, A and a, and the measured grain sizes. Subsequently, under the assumption that the activation energy (420 kJ/mol reported by Kinamuchi [152] for submicron ceria) is not changed under electric fields, the fourth term, E_{p3} was considered and the fictive sample temperature was adjusted until obtaining a good fitting between model and experiments (as shown in Figure 66). The fictive temperature was 22 K and 47 K higher than that of the fieldless sample for 14 V/cm and 28 V/cm, respectively. This enables to quantify and validate the effect of applied electric fields in terms of equivalent thermal energy transferred to the sample, but does not give any hint about the real nature of the electrical field effect.

The model shows a good agreement with the measured data (the difference remains less than 15 % up to a relative density of 84 %), except for the highest relative density of 85 % under electrical fields, where the uniaxial viscosity was overestimated. Possible explanations for the effect of electric field or sintering parameters are: change in the grain boundary structure and the activation energy for grain boundary diffusion, temperature microgradients (as macroscopic Joule heating is excluded).

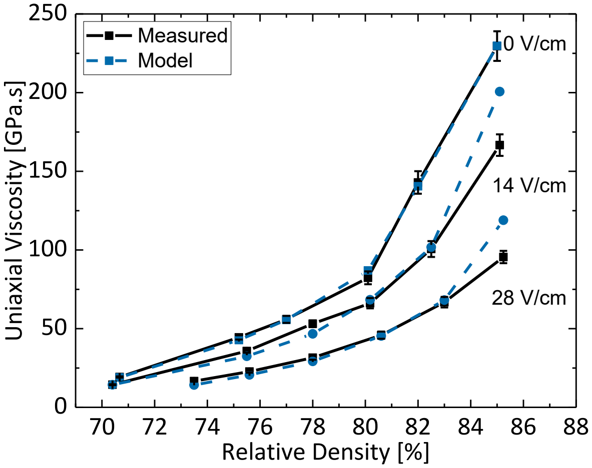

Figure 66: Comparison between measured uniaxial viscosity and theoretical prediction, introducing a fictive temperature increase in the presence of electric fields for 10YDC.

4.4.3.2 Confirmation of symmetric behavior under tensile loading

Sintering under tensile stress is a more common situation, e.g. in constrained sintering. Until now, all sintering parameters for ceramics have been obtained under compressive tests, and existing sintering models silently assume that the compressive and tensile response is symmetric. Therefore, it is a very crucial question whether the compressive response can be extrapolated to tensile stress configurations. In order to answer this question, the uniaxial viscosity was for the first time measured under tensile stress with the experimental procedure introduced in section 3.4.3.

The displacement vs. time curves obtained directly from the experiments included not only the shrinkage of the sample but also the thermal expansion of the equipment, as seen in Figure 67a, and Figure 67b shows the axial true strain on the dependence of time after excluding the thermal expansion of the equipment. Thereby, the axial strain rate can be calculated and used in the viscosity determination according to Eq. 2-14. After the discontinuous loading-dilatometry experiments conducted at NIMS, measurements under compressive condition were performed in Jülich with the experimental procedure introduced in section 3.4.3.3.

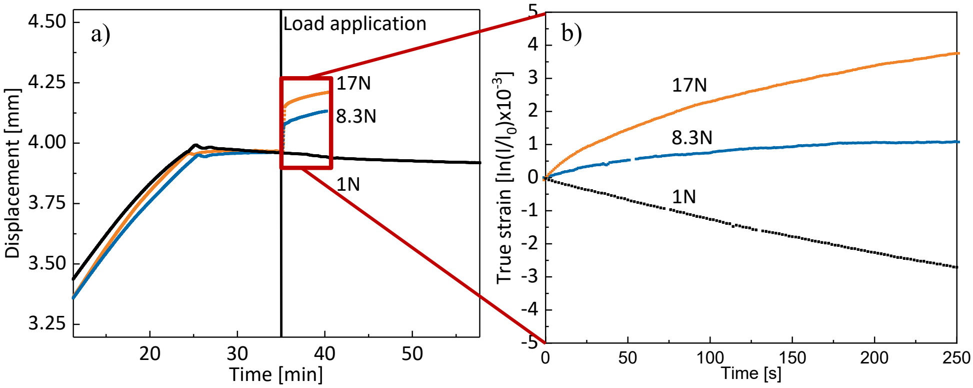

Figure 67: Sinter forging behavior under tensile loads obtained under E_{rms}=14 V/cm and $T_{furnace}$=1150 °C for 01YDC-Batch3; a) raw displacement data as a function of time measured using discontinuous loading dilatometry and b) true strains as a function of time after the thermal expansion correction during load application.

Uniaxial viscosity is related to various parameters, such as temperature, relative density and microstructure [190]. Since the experiments under tension and compression have been conducted using different experimental setups, it is important to confirm the applied experimental conditions. The comparison of the heating program between the compression and tension conditions is shown in Figure 68a. The measured furnace temperatures as a function of time agree well with each other. There is a small deviation of the temperature before reaching 900 °C. However, this small deviation is unavoidable by considering the difference in the furnace sizes and the controlling systems. Nevertheless, the orange line (Figure 68a) confirms that the isothermal temperature during the uniaxial viscosity measurement is the same.

The comparison of the current density is shown in Figure 68b, reaching a small value of 4.4 mA/mm^2 in both cases. The shorter experimental duration under the compressive loading lies in the effect of mechanical loading on densification. The tensile stress in a certain extent inhibits densification. More specifically, the sintering rate is smaller under tension and thus a longer holding time is required at 1150°C. In addition, no difference in the microstructure and grain size can be observed between specimens under compression and tension, as discussed in section 3.6.1.

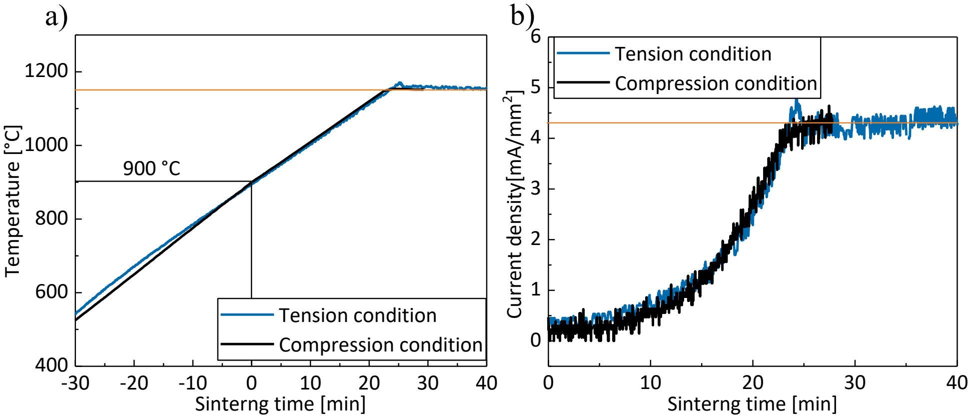

Figure 68: Comparison of experimental condition between compression mode and tension mode a) heating program b) current density.

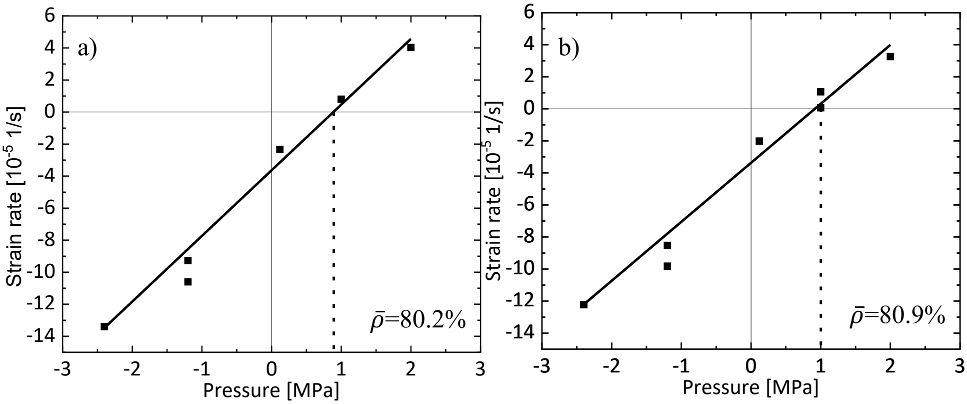

Figure 69: Axial strain rate as a function of uniaxial load for both the compression and tension tests at E_{rms}=14 V/cm and $T_{furnace}$=1150 °C for 01YDC a) at the relative density of 80.2 % and b) at the relative density of 80.9 %.

Figure 69 shows axial true strain rate as a function of uniaxial load under E_{rms}=14 V/cm and $T_{furnace}$=1150 °C. The linear relationship between axial strain rate and uniaxial load was confirmed under both the tensile and compression tests for the relative densities of 80.2 % and 80.9 % under E_{rms}=14 V/cm. According to our previous work [190], the measured uniaxial viscosity increases initially with respect to relative density. The as-determined uniaxial viscosity under E_{rms}=14 V/cm increased with the relative density from 24.4 GPa.s for 80.2 % to 27.2 GPa.s for 80.9 %, which illustrates a positive dependence of uniaxial viscosity on the relative density. Moreover, the linear relationship of the strain rates and the loading conditions validates the continuum theory, which assumes that the measurements conducted under compression can be extrapolated into the tensile regime.

Furthermore, the experiments under tension also enable the evaluation of the uniaxial sintering stress directly from the zero strain rate condition, without extrapolating the results obtained from experiments under compressive stress. The uniaxial sintering stress is a mathematical concept and is the equivalent to externally compressive stress that causes the same effect during free sintering [24,36,62]. This means that the densification in the axial direction stops when the uniaxial tensile stress that equals to the sintering stress is applied. The uniaxial sintering stress σ_z^S was experimentally determined by the extrapolation of the linear relation between uniaxial strain rate vs. uniaxial compressive stress until the uniaxial strain rate equals to zero [57], which can be described according to Eq. 2-34.

The absolute value of the sintering stress increases during the intermediate stage of sintering. As illustrated in Figure 69, as the relative density increases, the sintering stress increases (illustrated as the dash line in Figure 69).

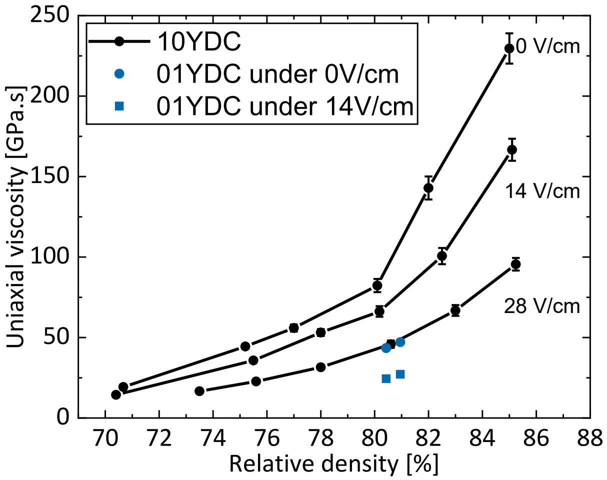

,

Figure 70: Comparison of uniaxial viscosity between 01YDC and 10YDC under different electrical fields and furnace temperature. (10YDC: T_{sample} = 1210 °C; 01YDC: T_{sample} = 1150 °C).

The influence of moderate AC electrical fields and currents on the uniaxial viscosity for 01YDC was also investigated, by measuring the uniaxial viscosity under compression without electrical fields. The uniaxial viscosity increased from 43.2 GPa.s at the relative density of 80.2 % to 47.1 GPa.s at the relative density of 80.9 %. The comparison with the values measured under electrical fields (Figure 70) indicates a decrease by a factor of about 1.7 under the electrical fields. It is worth mentioning that the value of the current density is only around 4.4 mA/mm^2, which excludes any macroscopic Joule heating effect. As discussed in section 4.4.3.1, at a fixed relative density (for example, 80.3 %) for 10YDC, the uniaxial viscosity under E_{rms}=14 V/cm decreased by about a factor of 1.2, while E_{rms}=28 V/cm prompted a decrease by about a factor of 1.8 compared to the value measured without the electrical fields [190]. However, it is hard to discuss the influence of doping level, because there is a difference of 50 K in the sample temperature. The two different experimental temperatures are chosen on the base of sintering behavior of powders: the isothermal temperature should not be too high to ensure most densification happen during the isothermal period instead of the heating period and not to be too low to ensure the load application is effective for the relative density increase. The sintering behaviors depend on the starting conditions of the powders. The starting condition of the as-delivered 01YDC-bacth3 powder is different from calcined 10YDC-Batch1 powder used in our previous work [190], as discussed in section. . These results indicate that the positive effect of the electrical field on the uniaxial viscosity is not restricted to a specific doping level.

To conclude, the discontinuous sinter-forging experiments were conducted for the first time under tensile loading. By carrying out discontinuous sinter-forging experiments under moderate AC electric fields under tension and compression, we could conclude that for 0.1 mol% yttrium-doped ceria compressive and tensile response is symmetric. This was confirmed from two experimental facts: i) the linear relationship of strain rates under the compressive and tensile loading and ii) the same uniaxial viscosity obtained at a given relative density. Furthermore, the positive effect of the electrical fields on the uniaxial viscosity of both 01YDC and 10YDC [190] indicates that the field effect is not restricted to a specific doping level.

4.4.4 Sintering stress

Besides uniaxial viscosity, sintering stress was also measured for 10YDC-Batch1. Sintering stress as a function of the relative density is plotted in Figure 71. The application of electrical field leads to an increase in the uniaxial sintering stress, even without any macroscopic Joule heating effect. Taking the relative density of 80 % as an example, larger sintering stress was determined when external electrical fields were applied. According to Figure 71, the absolute value of measured sintering stress first increases and then decreases, the transition range lying between relative density of 80 % and 84 %. It corresponds approximately to the onset of the pronounced grain growth, which is consistent to the grain size analysis (Figure 60).

At a fixed relative density, for example, 85 %, the sintering stress under E_{rms} = 14 V/cm increased by a factor of about 1.18, while E_{rms} = 28V/cm induced an increase of a factor about 1.26 in comparison with 0V/cm. While in the case of 75 %, the sintering stress under E_{rms} = 14 V/cm increased by a factor of about 1.40, while E_{rms} = 28V/cm induced an increase of a factor about 1.66 in comparison with 0V/cm. That is to say, the effect of electric fields on the sintering stress is not constant for different relative densities.

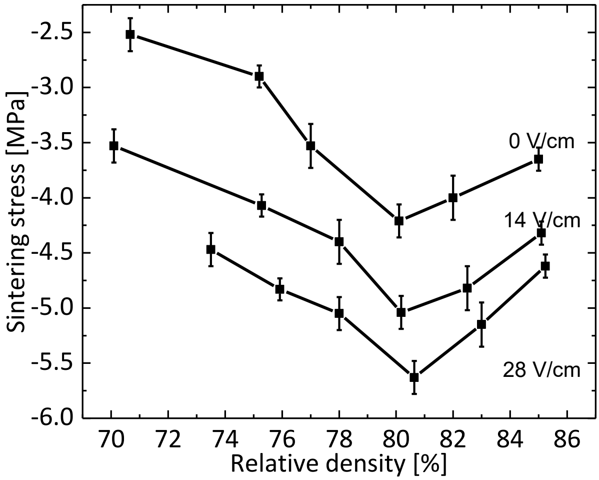

Figure 71: Sintering stress as a function of relative density using discontinuous loading-dilatometry for 10YDC-Batch1 with T_{sample} = 1210 °C.

Considering an idealized microstructure, the basic form for sintering potential can be expressed according to Eq. 2-4 (section 2.2.1.1). At low relative densities, smaller pores with larger surface curvatures dominate the microstructure, and the absolute value of the sintering stress increases along with the decreasing surface curvature. At higher relative densities, the decrease of the number of pores and especially the coarsening of the grains explains the decrease of the absolute value of the sintering stress, as shown for grain size (Figure 60) and the microstructure including pore orientation is not modified by applied stress and electric fields (Figure 63). This means that electric field could modify both grain boundary and surface energies, resulting in the measured increased sintering stress.

The definition of sintering stress according to Riedel *et al.* [48] is the mechanical stress which just equals to the surface tension forces to stop the shrinkage. That is to say, sintering stress is supposed to increase with grain boundary energy or the specific surface energy. Ghosh *et al.* [92] gave an expression of grain boundary interfacial energy dependent on the excess of enthalpy and entropy (Eq. 2-32).

According to this equation, a higher local temperature would lead to a lower grain boundary energy, due to the positive excess entropy of the boundary. This was experimentally verified by a slight decrease of relative grain-boundary energy (Υ_{GB}/Υ_s) of alumina from 1450 °C to 1650 °C of about 6 % [191]. Tsoga and Nikolopoulos [192] used the multiphase equilibration technique to determine the surface energy as well as the grain boundary energy of the equilibrium angles of polycrystalline yttria-stabilized zirconia from 1300 °C to 1600 °C, and also concluded that both surface energy and grain boundary energy decreased linearly with temperature However, it is doubtly to conclude that higher electrical fields lead to lower local temperatures. According to the above discussion, a localized temperature gradient cannot be the only explanation for the measured results. Moreover, the numerical simulation of mixed or ionically conducting ceramics shows no significant contribution of high temperature gradient (smaller than 10 K in a grain that is 100 nm in diameter) under a high current flow of 10^4 A/m^2 [104]. Even though in the work of Schwesig [9], density fluctuation in the microstructure of nanocrystalline silicon was used as an indication of existence of the microscopic temperature gradient, but without a quantification of the temperature increase.

4.4.5 Viscous Poisson’s ratio, bulk viscosity and shear viscosity

Bulk viscosity, shear viscosity and viscous Poisson’s ratio were calculated as a function of relative density according to Eq. (2-26 – 2-28). The resulting curves of bulk viscosity are shown in Figure 72, and the viscous Poisson’s ratio in Figure 73. Both bulk viscosity and Poisson’s coefficient increase along with the relative density, but change oppositely with electrical fields. The as-determined viscous Poisson’s ratio increases from 0.11 at the relative density of 70 % to 0.24 at the relative density of 85 % under E_{rms}=0 V/cm. In the case of E_{rms}=14 V/cm, the viscous Poisson’s coefficient increases from 0.12 to 0.27 in the range of 70 % to 85 %, while for E_{rms}=28 V/cm, the viscous Poisson’s ratio increases from 0.19 to 0.31 within a relative density range from 73.5 % to 85 %.

The measured viscous Poisson’s coefficient from our work is lower than the values from both Chang’s work [193] and Zuo’s work [58]. Wakai *et al.* [98] discussed the dependence of viscous Poisson’s ratio of the same relative density on different factors, and concluded that viscous Poisson’s ratio us affected by coordination number, ratio of grain boundary energy to surface energy as well as non-dimensional viscosity (Eq. 2-31). With this in mind, the difference can be attributed to either the experimentally confirmed segregation of yttrium at the grain boundary or the inhomogeneous powder compacts with large agglomerates and relative small particles. These two factors can influence not only the ratio between the grain boundary energy and surface energy but also the grain boundary sliding, which subsequently affects the uniaxial Poisson’s ratio.

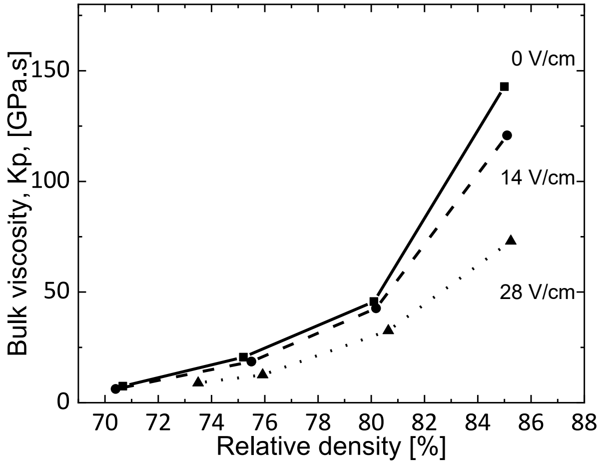

Figure 72: Bulk viscosity as a function of relative density using discontinuous loading-dilatometry.

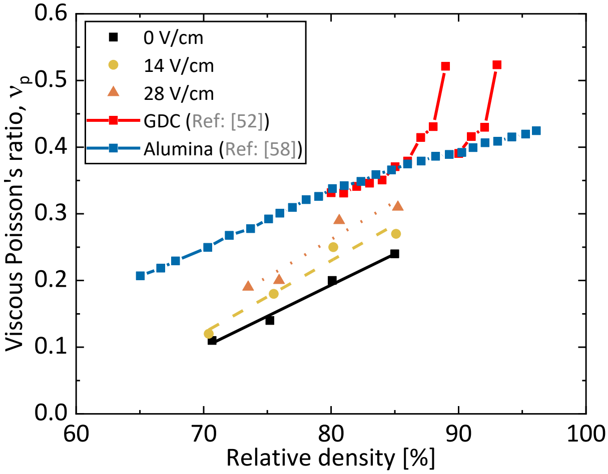

Figure 73: Uniaxial viscous Poisson's ratio as a function of relative density using discontinuous loading-dilatometry. Comparison of the measured viscous Poisson's ratio under different electrical fields of our work with the viscous Poisson's ratio of alumina, gadolinium-doped ceria (the line was added to guide the eye).

Various parameters need to be considered for the analysis of viscous Poisson's ratio, such as temperature, grain size and possible anisotropic microstructure induced by the applied stress and electric field. As already shown in Figure 60, there is hardly any difference in grain size between the different samples within the density range considered. Moreover, the highest sample temperature in the axisymmetric plane of the sample was kept the same with and without electrical fields by lowering the furnace temperature to compensate the macroscopic Joule heating effect induced by the current flowing through the specimen. Ollagnier *et al.* [56] pointed out that even though the thermodynamic boundaries for isotropic bodies are $0 < \upsilon_p < 0.5$, Poisson's ratio values between -1 and 1 are possible for anisotropic materials. Zuo *et al.* [35,189] emphasized a textured microstructure with preferred pore orientation along the load direction is the main cause of a negative viscous Poisson's ratio determined from continuous loading-dilatometry experiments. Chang *et al.* [193] also showed a dramatic increase of the viscous Poisson's ratio up to values higher than 0.6 for Gd-doped ceria with relative density higher than 84 %, and related the result to the anisotropy of the material. Figure 63 proved the isotropic microstructure of the samples after discontinuous loading-dilatometry.

Therefore, it is conceivable to conclude that the observed difference of the viscous Poisson's ratio under electrical fields can not be attributed to above mentioned variables. According to Eq. 2-30, the viscous Poisson's ratio can be formulated as a function of bulk viscosity and shear viscosity. Riedel *et al.* [49] developed a method to estimate bulk viscosity and shear viscosity of isotropic porous materials from the knowledge of microstructure. The densification process is related to the microscopic motion of individual particles. The velocity vector normal to the grain boundary is proportional to the grain boundary diffusion coefficient, while the tangential velocity is linked to the microscopic viscosity. Wakai *et al.* [16] analyzed how shear viscosity and viscous Poisson's ratio depend on grain boundary sliding, local structure, and relative density. When grain boundary diffusion is the dominating mechanism during sintering, bulk viscosity is dependent on grain boundary diffusion coefficient, and shear viscosity depends on both grain boundary diffusion coefficient and grain boundary sliding, which is characterized by the non-dimensional viscosity, η^*.

As shown in Figure 72 and Figure 74, both bulk viscosity and shear viscosity decrease with the application of electric field. Since bulk viscosity is inversely proportional to the grain boundary diffusion coefficient [60], the experimental result suggests that the grain boundary diffusion coefficient is enhanced by the application of electric field. The slight change in the bulk viscosity compared to the change in shear viscosity indicates that this enhancement by the electrical fields is not very significant. When the grain boundary sliding occurs freely ($\eta^* = 0$), the shear viscosity depends on grain boundary diffusion only, so that the effect of electric field should be the same as for bulk viscosity. However, the comparison of Figure 72 with Figure 74 shows that the influence of electric fields on shear viscosity is more significant than that on bulk viscosity, especially at E_{rms}=28V/cm. At a fixed relative density, for example, 85 %, the bulk viscosity under E_{rms}=14 V/cm decrease by a factor of about 0.8, while E_{rms}=28V/cm induced a decrease of a factor about 0.51 in comparison with 0V/cm. For the case of shear viscosity at the relative density of 85 %, the shear viscosity under E_{rms}=14 V/cm decrease by a factor of about 0.7 while E_{rms}=28V/cm induced a decrease of a factor about 0.35 in comparison with 0V/cm. The result implies following statements: (i) Non-dimensional viscosity is positive; (ii) Non-dimensional viscosity decreases with electrical fields, because shear viscosity increases with η^* [16]. Therefore, the increase in viscous Poisson's ratio observed under electric field can be related to the decrease in η^*, even though there should be a slightly increase in the grain boundary diffusion coefficient on the base of decreasing bulk viscosity with electrical fields. The decreasing non-dimensional viscosity could be related to decreasing microscopic viscosity, which is related to the grain boundary structure or a microscopic temperature gradient. Both can be possibly influenced by the electrical fields.

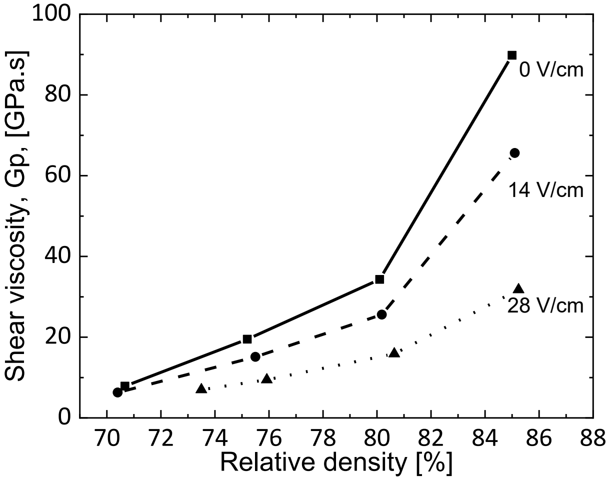

Figure 74: Shear viscosity as a function of relative density using discontinuous loading-dilatometry.

Shihkar *et al.* [194] argued that the field can provide the work for the formation of a defect by stripping the charge from a vacancy or an interstitial point, leaving them neutrally charged and free to move. The generation of defects within the grain matrix shortened the migration distance for the shear deformation, which can explain the effect of electrical fields on obviation of constrained sintering.

4.5 Field effect on activation energy

The experiment results show that electrical fields have a positive influence on the sintering behavior of both 10YDC and 01YDC. The possible mechanisms behind, however, are yet to be revealed. The low electrical fields clearly do not exercise their influence via macroscopic Joule heating. The deviation of the fitting of uniaxial viscosity (Figure 66) and the corresponding increase of sintering stress under the presence of electrical fields are athermal effects. As pointed out by Zuo *et al.* [195], the temperature increase has no effect of sintering stress, by excluding grain growth effect under higher temperature with respect to the normalizing grain size. Thus, we use the activation energy for densification as a fingerprint to find out the effect of electrical field.

The determination of activation energy requires an accurate knowledge of specimen temperature [190]. The current density is the fingerprint for macroscopic Joule heating effect. The combination of simulation and experiments on 10YDC shows that the macroscopic Joule heating effect can be neglected with the current density of 12 mA/mm^2 [190]. For 01YDC under E_{rms} = 14 V/cm, 28 V/cm and 10YDC under E_{rms}=14 V/cm, the current densities were all much lower than this value. Therefore, it is reasonable to assume the macroscopic Joule heating can be neglected for both cases. Specimen temperature was assumed to be the same as the furnace temperature. However, in the case of 10YDC under E_{rms}=28 V/cm, due to a higher current density (for example, 19 mA/mm^2 with the furnace temperature of 1008 °C), specimen temperature was measured under E_{rms}=28 V/cm with the furnace temperature of 1008 °C, 1058 °C and 1108 °C and the results were listed in Table 11. This calibrated specimen temperature was used in the evaluation of activation energy.

Table 11: Specimen temperature T2 for 10YDC under E_{rms} = 28 V/cm with different furnace temperature T1 [°C]

Furnace temperature T1	1008	1058	1108
Sample temperature T2	1055	1100	1146

The determination of activation energy in this work is based on the knowledge of specimen temperature mentioned above. The processes for activation energy determination for 01YDC and 10YDC are shown in Figure 75 and Figure 76, respectively. Figure 75a and Figure 76a show the densification curves for 01YDC and 10YDC, respectively, with the arrow indicating the increasing isothermal temperatures applied. The densification rates increased accordingly to the isothermal temperatures. The horizontal lines in the figures imply two specific relative densities: 82.5 % and 85 %, where the slopes of the curves were used to calculate densification rates. Figure 75b and Figure 76b show Arrhenius plots of the logarithm of the densification rate versus the inverse sample temperature for 01YDC and 10YDC, respectively. The activation energies calculated from Figure 75 and Figure 76 is listed in Table 12. The values are comparable to other experimental results such as 576±19 kJ/mol for nanostructured 10GDC [196] and 420 kJ/mol for submicron ceria [152]. For 10YDC, the activation energy decreases by a factor of 0.93 at E_{rms}=14 V/cm, and a factor of 0.62 at E_{rms}=28 V/cm. For 01YDC, the activation energy decreases by a factor of 0.92 at E_{rms}=14 V/cm, and a factor of 0.91 at E_{rms}=28 V/cm. The results can be summarized as follows: i) the activation energy decreases with increasing electrical field strength for both materials: 01YDC and 10YDC; ii) the decrease in activation energy is significant for 10YDC, whereas no significant change were observed for 01YDC.

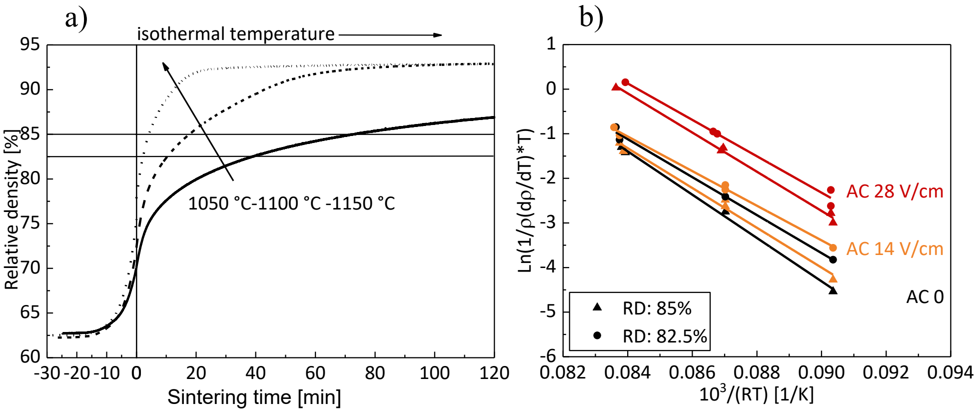

Figure 75: Activation energy measurements of 01YDC a) illustration of the relative density as a function of the sintering time under E_{rms}=14 V/cm at a isothermal temperature of 1050 °C, 1100 °C and 1150 °C; b) determination of activation energy using Arrhenius plot for E_{rms}=0 V/cm, 14 V/cm and 28 V/cm.

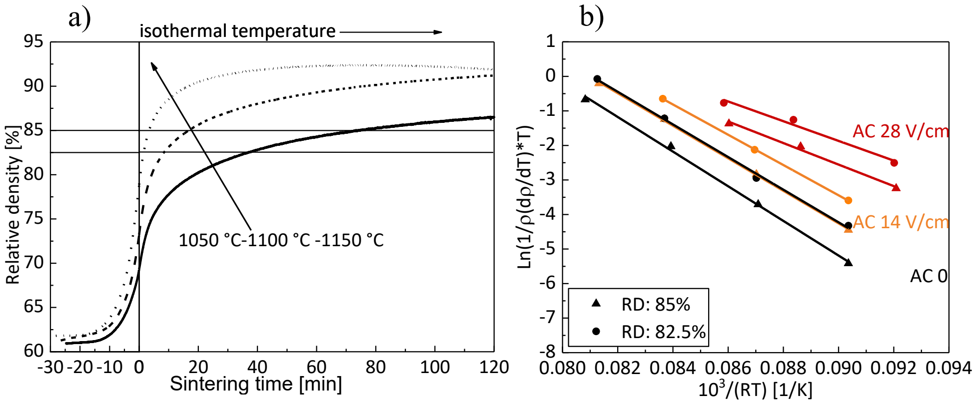

Figure 76: Activation energy measurements of 10YDC a) illustration of the relative density as a function of the sintering time under E_{rms}=14 V/cm at a isothermal temperature of 1050 °C, 1100 °C and 1150 °C; b) determination of activation energy using Arrhenius plot for E_{rms}=0 V/cm, 14 V/cm and 28 V/cm.

Table 12: Activation energies for the sintering of 01YDC and 10YDC (kJ/mol).

	Electrical field strength [V/cm]		
	0	14	28
01YDC	485±39	445±36	439±37
10YDC	502±40	466±38	311±25

In spite of the exclusion of macroscopic Joule heating effect, a local Joule heating effect at grain boundaries may still exist. Even though numerical simulation revealed no temperature gradients (smaller than 10 K in a grain with the diameter of 100 nm in mixed or ionically conducting ceramics [104]), which is supposed to be due to the small particle size. The similar conclusion has been drawn by Semenov *et al.* [105] via a metal system with thermo-electro-mechanical modeling even with ten times higher electrical loading than a typical FAST/SPS condition, considering the high thermal conductivity of metal. However, the simulations all assumed an equilibrium state of a homogeneous compact, while the real sintering behavior is a non-equilibrium process, which indicates the microscopic Joule heating at grain boundaries is still possible during the sintering. In addition, from a mesoscopic point of view, fluctuation of relative densities may occur in different areas of the specimen due to a heterogeneous powder distribution, with the microstructures in Figure 61 as examples. A temperature difference probably exists in these areas, since the conductivity of the powder compact depends on the heterogeneous relative density distribution. The activation energy measured is an average value of the whole powder compact, and the inhomogeneous temperature distribution in the heterogeneous powder compact can lead to a change of activation energy.

Sintering activation energy is also related to the defect chemistry of the material. It is widely accepted that the migration of cations is the rate limiting transport process for sintering. Dong *et al.* [151] calculated the migration energy for cation diffusion with different paths, and concluded that the migration energy for interstitial diffusion Ce^{3+} with an oxygen vacancy nearby is 24 % lower than interstitial diffusion Ce^{4+} without an oxygen vacancy nearby. In summary, the migration energy of cerium can be reduced largely due to the synergistic effect of reduction of cerium and increased concentration of oxygen vacancies (section 2.5.2).

Therefore, it is assumed that the microscopic Joule heating can influence the reduction of cerium, and thus the cation migration energy during the sintering. However, the local temperature increase may not be the only possibility in promoting the reduction of cerium. The numerical simulation obtained by a finite elements (FE) approach using the FlexPDE (PDE Solutions, Inc., Spokane Valley, USA) confirmed the existence of a magnified local electrical fields [106]. According to the simulation, the local field strengths can be higher than the applied external field by a factor of about 180 for materials with a dielectric coefficient of 30. The amplified local can be either due to the geometry of neck or the space charge layer (section 2.4.2.2), and this amplified local electrical fields can facilitate the reduction of cerium. Moreover, the reduction of cerium can introduce more oxygen vacancies. The easier migration of cation due to these two effects can also lead to the decrease of activation energy.

In order to prove the above mentioned theory, *ex-situ* XAS experiments were conducted on specimens sintered with and without electrical fields and shown in Figure 77 and Figure 78, respectively.

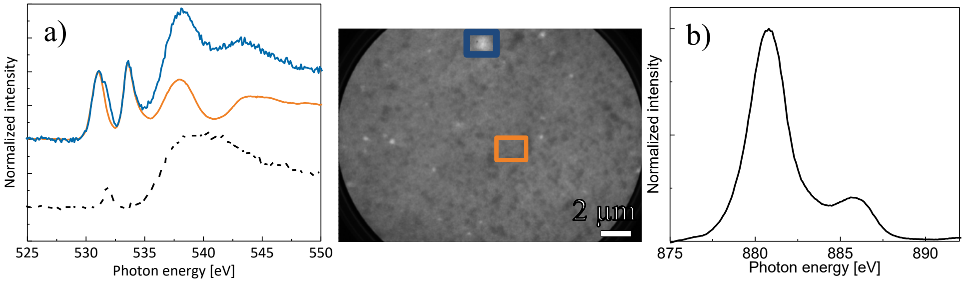

Figure 77: X-ray absorption near edge structure spectroscopy (XANES) of 10YDC sintered under 0 V/cm a) measurements of Ce-O of the areas with different contrasts (marked with blue and orange, respectively, in the SEM image) and the difference between these two curves (black dash line) b) measurements of Ce-M-edge. The XAS experiments were conducted by Dr. David Müller from PGI-6, Forschungszentrum Jülich.

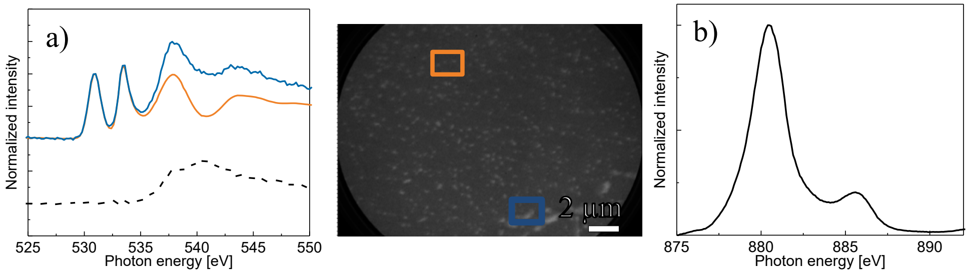

Figure 78: X-ray absorption near edge structure spectroscopy (XANES) of 10YDC sintered under E_{rms} = 28 V/cm a) measurements of Ce-O of the areas with different contrasts (marked with blue and orange, respectively, in the SEM image) and the difference between these two curves (black dash line) b) measurements of Ce-M-edge. The XAS experiments were conducted by Dr. David Müller from PGI-6, Forschungszentrum Jülich.

For both samples (Figure 77a and Figure 78a), the difference (black dash line) between areas with difference contrast (marked with blue and orange, respectively) are the signal of silicon dioxide, contaminants from the polishing process. The measurements show no signal of Ce^{3+} (Figure 77b and

Figure 78b). This result fits well to that of the DTA-TG experiments, showing an immediate oxidation of cerium at RT. It is noteworthy mentioning that the results detected at RT cannot be used to imply the condition of the experiments under higher temperature, and thus cannot exclude the possibility of the defect chemistry mechanism.

4.6 Field effect on ionic conductivity

Similar to sintering process, ionic conductivity depends not only on diffusion processes but also on defect chemistry. As mentioned in section 2.4.2.2, the electrical response of grain boundaries was found to change under DC flash sintering [88], but not under AC flash sintering [123]. Moreover, Vendrell *et al.* [197] found out that the ionic conductivity of flash-sintered Yttria-stabilized zirconia (YSZ) increased with increasing maximal current density. This phenomenon was attributed to a change in the YSZ defect structure. In order to investigate the effect of electrical fields on diffusion processes, we measured the ionic conductivities of the specimens sintered under different conditions using EIS.

The temperature dependence of bulk conductivity and specific grain boundary conductivity of 10YDC and 01YDC sintered under different conditions are shown in Figure 79 and Figure 80. The conductivities definition and their calculation methods are introduced in section 2.5.3.1. It is worth noting that the grain boundary conductivity discussed here is related to the traversable charge carrier migration across grain boundary, as explained in Figure 22 (Section 2.5.3.1). One important conclusion obtained from Figure 79 and Figure 80 is that the grain boundary conductivity is lower than grain interior conductivity: the specific grain boundary conductivities were 2-3 orders lower than bulk conductivities for 10YDC, while 3-5 orders lower for 01YDC.

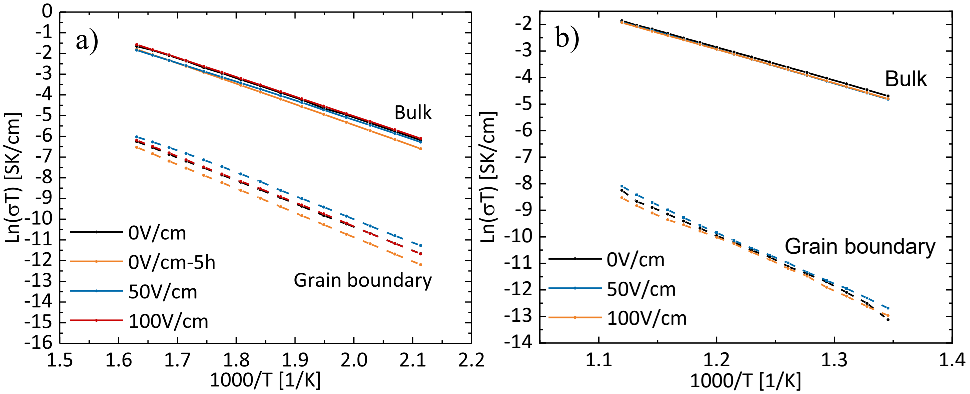

Figure 79: Arrhenius plots of specific grain-boundary conductivities and the bulk conductivities for specimens sintered at furnace temperature of 1300 °C for 2 h without electrical fields and with non-contacting E_{rms}=50 V/cm and E_{rms}=100 V/cm, with one exception for 10YDC without electrical fields for 5 h: a) 10YDC in the entire temperature range (200 °C-340 °C); b) 01YDC in the entire temperature range (450 °C-620 °C).

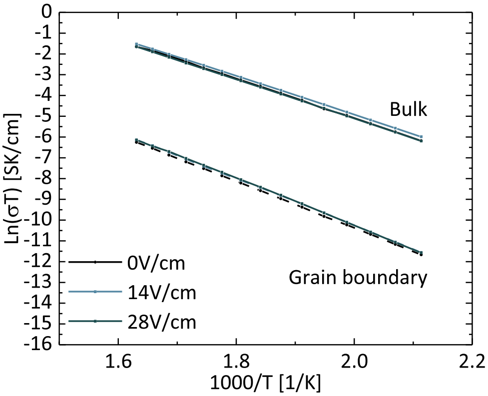

Figure 80: Arrhenius plots of specific grain-boundary conductivities and the bulk conductivities of 10YDC in the entire temperature range (200 °C-340 °C): sintered without electrical fields for the holding time of 2 h and with contacting electrical field with E_{rms}=14 V/cm and 28 V/cm for the holding time of 2 h.

As pointed out by Guo *et al.* [98], the grain boundary conductivity is 2-7 orders lower than the bulk conductivity for 20- and 2.0-mol % yttrium doped ceria (20YDC and 02YDC). The difference depends on the doping level, temperature and oxygen partial pressure. The low conductivity of the grain boundary has been earlier attributed to an intergranular siliceous phase on the triple junction point on grain boundary [98,198-199]. This theory, however, can only explain the phenomenon when the activation energy of grain boundary conductivity varying with the properties of the siliceous phases, which contradicts existing experimental results [98]. In addition, in TEM analysis of 01YDC, according to the microstructure investigation in our previous work [200], a sharp grain boundary without amorphous phases was observed.

Therefore, space charge model should be applied to explain the lower ionic conductivity of grain boundary. The lower grain boundary conductivity is caused by depletion of oxygen vacancies near grain boundary cores (section 2.4.2.2). Thereby, the traversable migration of oxygen ion across boundary is more difficult than inside the bulk [97]. Grieshammer and De Souza [201] also pointed out the depletion of mobile defects in the region of grain boundary caused by the formation of space charge layer can consequently lead to a decrease in grain boundary conductivity of doped ceria. Iguchi *et al.* [93] proved the existence of space charge layer in Y-doped $BaZrO_3$ (BZY). In addition, they estimated the space charge potential based on a model describing the current–voltage relationship of blocking grain boundaries, as proposed by Kim *et al.* [94]. Guo *et al.* [98] also reported a positive space-charge potential of acceptor-doped CeO_2, leading to an oxygen-vacancy depletion and the electron accumulation in the space-charge layer.

Corresponding activation energies for the bulk conductivities and specific grain boundary conductivities are given in Table 13 and Table 14. Activation energies were calculated on the base of the slopes of the Arrhenius plots of the logarithm of specific grain-boundary conductivities and the bulk conductivities versus the inverse temperature in Figure 79 and Figure 80. The slopes under different conditions remain constant, which indicate that activation energies did not alter with the electrical fields with or without currents. This is also confirmed by calculated activation energy values. The calculated values are comparable to the values reported by Guo *et al.*: 0.97 eV (bulk) and 1.03±0.01 eV (grain boundary) for 20YDC, as well as 1.13±0.01 eV (bulk) and 1.98±0.06 eV (grain boundary) for 02YDC [98].

Table 13: Activation energies of 10YDC in air atmosphere with the measurement error smaller than 0.01 eV.

Conditions	**Activation energy [eV]**	
	Bulk	Grain boundary
0V/cm	0.82	0.98
0V/cm-5h	0.83	1.01
Non-contacting 50V/cm	0.81	0.99
Non-contacting 100V/cm	0.81	0.98
14V/cm	0.80	0.97
28V/cm	0.81	0.97

Table 14: Activation energies of 01YDC in air atmosphere with the measurement error smaller than 0.01 eV.

Conditions	**Activation energy [eV]**	
	Bulk	Grain boundary
0V/cm	1.08	1.73
Non-contacting 50V/cm	1.10	1.71
Non-contacting 100V/cm	1.09	1.70

As shown in Figure 79, the bulk conductivities of 10YDC and 01YDC are independent of applied electrical fields with and without currents in the range of measured temperature. For 01YDC, the specific grain boundary conductivities also do not alter under different conditions. For 10YDC, as shown in Figure 79a, a long holding time (5 h) decreases the grain boundary conductivities by a factor of 0.66 compared to conductivities of specimens sintered without electrical fields, while a non-contacting E_{rms}=50 V/cm increases the grain boundary conductivities by a factor of 1.44. In addition, the influence of current during sintering on the *ex-situ* conductivities for 10YDC is shown in Figure 80. The results imply that both the bulk and grain boundary conductivities do not alter under different electrical field strengths.

As discussed before in section 4.4.2.1, there is only a slight grain size increase for 10YDC with longer holding time of 5 h with a factor of about 1.1, and a decrease with a factor of 0.96 for 10YDC under non-contacting E_{rms}=50 V/cm compared to specimens sintered without electrical fields. Basically, there is no influence of electrical fields on grain sizes for both 10YDC and 01YDC. Moreover, the densification curves of 10YDC under 0 V/cm, non-contacting E_{rms}=50 V/cm and E_{rms}=100 V/cm (Figure 81) indicate no difference during the densification processes. In addition, the calculation of ionic conductivity is already normalized by grain sizes and specimen dimensions, as introduced in section 2.5.3.1. That is to say, the difference in grain boundary conductivities should not be attributed to the difference in grain sizes. The change in the grain boundary conductivities should be related to the grain boundary structure, such as grain boundary thickness, space charge layer and so on.

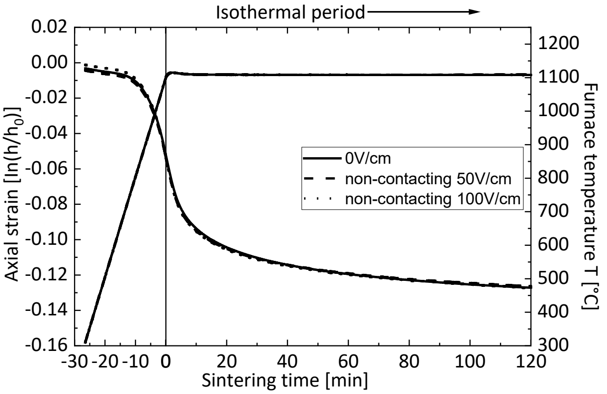

Figure 81: Axial strain, furnace temperature as a function of time for 10YDC.

In order to calculate the grain boundary conductivities (according to Eq. 2-49 and Eq. 2-50), the effective capacitances of bulk and grain boundary are necessary, as listed in Table 15. No obvious change in calculated effective bulk capacitances are observed for both cases (10YDC and 01YDC), with the biggest deviation about 10 % between 0 V/cm and the non-contacting E_{rms}=50 V/cm. However, the effective grain boundary capacitances of 01YDC decrease when sintered under non-contacting electrical fields, with a factor of about 0.6 under non-contacting E_{rms}=50 V/cm and a factor of about 0.7 under non-contacting E_{rms}=100 V/cm. For 10YDC, effective grain boundary capacitances under 0V/cm with a longer holding time increase by about a factor of 1.34, while non-contacting E_{rms}=50 V/cm with a holding time of 2 h prompts a decrease by about a factor of 0.54 compared to the fieldless sintering condition with the holing time of 2 h. Besides grain boundary capacitances, grain boundary resistances normalized by the specimen sizes are also necessary for grain boundary conductivities calculations according to Eq. 2-50, therefore, grain boundary resistivities of 10YDC under 300 °C and 01YDC under 560 °C as examples are also listed in Table 15.

The result implies the following conclusions: 1) the effective capacitances of bulk do not alter under different conditions for 10YDC and 01YDC; 2) for 01YDC, constant grain boundary conductivities are the result of an increase of resistances under electrical fields together with a decrease of grain boundary capacitances. For 10YDC, the grain boundary resistances do not alter under electrical fields, but increase under a longer holding time (5 h). Therefore the decrease of grain boundary conductivities under longer holding time for a fieldless sintering is due to an increase of both grain boundary capacitances and resistances, whereas a smaller grain boundary capacitance leads to a higher grain boundary conductivity under non-contacting E_{rms}=50 V/cm. In summary, there exists an effect of electrical fields on the effective capacitance. The effective capacitance of the material is influenced by the polarization of the defects with electric dipole moments, usually complex defects, in other words, the grain boundary structure. More specific, if the electrical field during sintering alters the defects distribution near the grain boundary, this influence should be displayed as a change in grain boundary capacity.

Table 15: Effective capacitance of 10YDC and 01YDC and grain boundary resistivity (normalized by the specimen sizes) of 10YDC (300 °C) and 01YDC (560 °C) without fields for the holding time of 2 h and 5 h, with non-contacting E_{rms}=50 V/cm and 100 V/cm for the holding time of 2 h at the atmosphere of air with the relative density of 94%-96%.

Electrical field	**Effective capacitance [F]**				**Resistivity [Ω.cm]**	
	10YDC		01YDC	01YDC	10YDC	01YDC
	Bulk	Grain boundary	Bulk	Grain boundary	Grain boundary	Grain boundary
0V/cm	2.76×10^{-11}	1.37×10^{-8}	2.60×10^{-11}	1.81×10^{-8}	2.93×10^{3}	1.77×10^{4}
0V/cm-5h	3.09×10^{-11}	1.84×10^{-8}			3.62×10^{3}	
Non-contacting 50V/cm	3.07×10^{-11}	7.47×10^{-9}	2.24×10^{-11}	1.00×10^{-8}	3.05×10^{3}	3.66×10^{4}
Non-contacting 100V/cm	2.88×10^{-11}	1.33×10^{-8}	2.50×10^{-11}	1.19×10^{-8}	3.94×10^{3}	3.92×10^{4}

The hypothesis of independent effective capacitance of bulk is obvious because the grain interior conductivity is an intrinsic property of the material (section 2.5.3). Moreover, our *ex-situ* XAS experiments showed no difference in the valence state of cerium in samples sintered with and without electrical fields, as discussed in section 4.5. The second hypothesis, the negative dependence of grain boundary capacitances on electrical fields, is related to the structure of grain boundary, such as grain boundary thickness, space charge layer and so on. Further evidence for the influence of electrical fields on the grain boundary structure is provided by TEM analysis as shown in Figure 82. The existence of Ce^{3+} was confirmed by electron energy loss spectroscopy (EELS). In addition, the width of Ce^{3+} distribution was estimated from the full width at half maximum (FWHM) of the HAADF image intensity profile across a grain boundary. The result indicates a wider distribution of Ce^{3+} across the grain boundary under non-contacting E_{rms}=50 V/cm, compared to those under 0 V/cm and non-contacting E_{rms}=100 V/cm. This wider distribution validates that a change in the distribution of complex defects occurred.

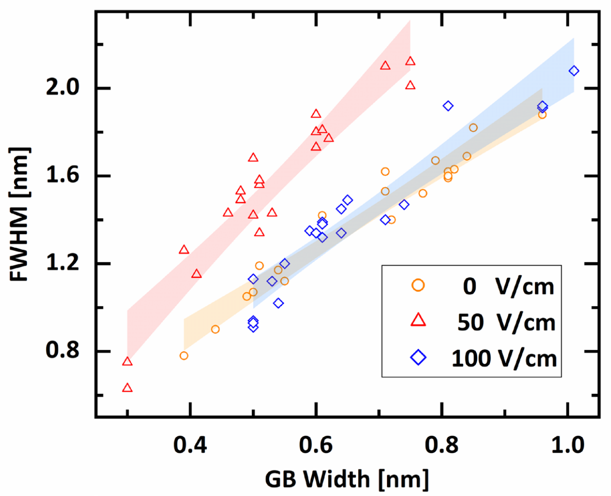

Figure 82: Full width at half maximum (FWHM) of the intensity profile of Ce^{3+} from the HAADF image across GB of 10YDC without fields and with non-contacting electrical field with E_{rms} = 50 V/cm and 100 V/cm.

In summary, electrical fields applied during sintering do not change the ion-conducting activation energy of either bulk or grain boundary. This indicates the same diffusion mechanism among specimens sintered under different conditions. The effective capacitance should be responsible for the change in ionic conductivity, and as a fingerprint of the defect chemistry, correlates to the oxygen vacancy concentration in the material. This assumption is proven directly by TEM measurement, displaying an *ex-situ* change in grain boundary, as well as the difference in Ce^{3+} distribution. This indicates that the electrical fields influence defect chemistry mechanism.

5. Conclusions and outlook

The exact underlying mechanism for field assisted sintering and more specifically flash sintering has been puzzling the materials community for a decade, after the first report of this ultra-fast densification phenomena in 2010 [12]. By applying electric fields, significantly lower than those required for the ‘flash regime’ on doped ceria samples, this work aimed at unveiling the possible mechanisms behind field assisted sintering.

Based on thoroughly designed and performed experiments, the sintering parameters were measured via the discontinuous sinter-forging technique for the first time. Generally, all sintering parameters are sensitive to grain size and to the degree of anisotropy in the microstructure potentially induced by the applied stress and electric field. For our experiments with yttria doped ceria, the grain sizes were found to be constant under different electrical field strengths and no microstructural anisotropy was induced by the loading conditions. Therefore, it is conceivable to conclude that the observed difference of sintering parameters under electrical fields cannot be attributed to macroscopic change of temperature or difference in microstructure. The results can be summarized as follows:

- Moderate electrical fields improve the sintering behavior of 10YDC, decrease uniaxial viscosity and increase the sintering stress.
- The bulk viscosity of 10YDC increases with densification and slightly decreases under electric field.
- The viscous Poisson’s ratio as well as the shear viscosity is significantly influenced by moderate electric fields of 10YDC, which can be attributed to the easier sliding of the grains
- Uniaxial viscosity for 01YDC decreases accordingly to the electrical fields, which implies the effect of electrical fields is not restricted to a specific doping level and also provides further evidence for the existence of field effect.
- The activation energies for the densification decrease by the increase of electrical field strengths for 10YDC and 01YDC, exerting larger effects for 10YDC.

The significantly enhanced sintering behavior observed under fields well below the flash regime point to several possible origins: gradual modification of the grain boundary structure (including space charge layer) and its properties (effective grain boundary conductivities and capacitances), as well as local temperature gradients undetectable at the macroscopic scale. In this work, the change of grain boundary microstructure under electrical fields is indicated by the increase of the grain boundary conductivity for 10YDC, together with the change in Ce^{3+} distribution confirmed by TEM analysis, which is related to the modified defect chemistry of the grain boundary, possibly due to localized high electrical fields.

Moreover, the symmetric behavior under tensile loading under the frame of continuum mechanics of sintering was examined. The uniaxial viscosity response of 01YDC was confirmed to be the symmetric between compressive and tensile responses. More specifically, the compressive response can be extrapolated to tensile stress configurations. Moreover, the experiments under tension also enable the evaluation of the uniaxial sintering stress directly from the zero strain rate condition, without extrapolating the results obtained from experiments under compressive stress.

In summary, this work has successfully confirmed the existence of athermal field effects on densification and sintering parameters by excluding the macroscopic Joule heating effect. However, the nature of these athermal effects as not been classified yet. On one hand, it is hard to decouple the local Joule heating effect from a direct field effect. On the other hand, it is still unclear how the electrical field interacts with grain boundaries or the space charge layer nearby.

To answer those open questions, characterization methods with high spatial and temporal resolution are required as well as the *in-situ* techniques in order to characterize the dynamics of the field assisted sintering. In addition, it is worth checking the effect of electrical fields on sintering with various frequencies. The responses of different microstructure features to the electrical fields are sensitive to the frequency according to the impedance spectroscopy measurements. In order to determine the ionic conductivities of bulk and grain boundary, the frequency required lies in the range of MHz at 200 °C and increases with increasing temperature. The frequency of AC electrical fields usually applied, however, is much lower (~50Hz) and should have no effect on sintering behavior. However, besides bulk and grain boundary, the interfaces between grains and pores have considerable influence on the sintering process, such as the surface diffusion during the initial stage of sintering. According to the impedance spectroscopy measurements, the frequency required for the impedance single of interfaces usually lies in a much lower frequency range compared to bulk and grain boundary. That is to say, these interfaces should have responses to electrical fields with a much lower frequency and are expected to interact with low frequency AC electrical fields. Therefore, these grain-pore interfaces, especially at the early stage of sintering, should also be studied in further researches, by investigating the field effect with changing frequencies of as wide range as possible. Moreover, the material used in this work is a typical oxide ceramic material, the investigation of the moderate field effects on other material systems may also lead to a deeper understanding of the mechanism. Possibilities are zirconia or yttrium stabilized zirconia, because of a possible phase change during sintering, Li-ion conducting materials for solid state batteries, because of different diffusion systems compared to the typical oxides. The investigations into other materials are also expected to open up other applications of this promising technique.

Acknowledgement

Time flies. Three years are short for an academic study, but long enough to build friendships and accumulate experience. Among my six years of stay in Germany, three years at the Institute of Energy and Climate Research (IEK-1: Materials Synthesis and Processing), Forschungszentrum Jülich GmbH. are important in every aspect. I would like to express my gratitude to all people who have given me either support on the work or in my life in Jülich.

At first, I would like to thank the funding from the German Science Foundation (DFG), under the priority program “Fields Matter” SPP 1959 [GU 933/9-1].

My sincere thanks to the head of the institute, Prof. Dr. Dipl.-Ing. Olivier Guillon, who is also my doctoral advisor (Doktorvater in German), for allowing me to conduct my doctoral study here and the excellent scientific supports. He also offers me valuable opportunities to attend international conferences and join the research exchange program. These experiences make me understand that scientific work is not only restricted to lab work and result analysis. The communications together with the cooperations with other scientists are essential as well.

My sincere thanks to my scientific supervisor, Dr. Robert Mücke, for his support in my work. I appreciate his help in my experimental work and discussions about the results. With almost no experience in lab work before, I learned a lot about lab work from him, not mentioning the modeling skills. Another important thing I have learned from him is his attitude towards the work. He also helped me for a smooth start in Jülich by finding me the apartment, which was relief at the beginning.

My sincere thanks to my co-workers in our SPP program. Working in such a big program makes me realize that one of the most important things in scientific work is networking. I also really appreciate the wonderful organization from Doris van Balen and Dr. Falk Schulze-Küppers for our annually soft skill school and convention, from which I learned a lot. I would also thank my project partners: Prof. Dr. Roger A. De Souza, Dr. Lei Jin, Jana Parras, and Zheng Ma. It is a pleasure to work with them.

My sincere thanks to all others who offer me support in scientific discussions as well as experimental supports. I would like to recognize the invaluable assistance I have received during my study. I really appreciate Prof. Dr. Wakai Fumihiro for his deep insights and knowledge of the sintering and his suggestions on the analysis of the results, Jun.-Prof. Dr. Jesus Gonzalez for his helpful dissuasions about my results and the kindness for offering supports, Dr. Chih-Long Tsai for his valuable discussions about the impedance spectroscopy measurement analysis, Dr. Christian Lenser and Dr. Mariya Ivanova for the help in operating impedance spectroscopy. I would like to thank Dr. Doris Sebold for the high-quality SEM pictures, Mark Kappertz for the valuable support for the sample preparation in the metallurgical lab, Andrea Hilgers for the particle size distribution measurements, Sigrid Schwartz-Lückge for the specific surface area measurements and cold isostatic pressing, Ralf Steinert for the cold isostatic pressing, Dr. Yoo Jung Sohn for the XRD measurements together with the lattice parameter calculation, and Marie-Theres Gerhards for the dilatometric measurements.

My sincere thanks for all the help and support during my research stay in Japan. I would like to thank Dr. Koji Morita for the interesting discussions on my experiments. My thanks also go to Prof. Byung-Nam Kim for the interest in my work and the wonderful discussions. I would also like to thank the college, Yamato Sasaki, for his help in my experiments.

My sincere thanks to my colleges in the institute for this lovely working atmosphere. Dr. Markus Mutter, who worked before in the modeling group, offered me great supports at the beginning of my PhD study in operating sintering-forging. I also want to thank Dr. Joao Gustavo Pereira da Silva, Apruv Dash, Tarini Prasad Mishra, and Moritz Kindelmann for the valuable scientific discussions. My thanks also go to other colleges: Prof. Dr. Payam Kaghazchi, Dr. Qian-li Ma, Tu Lan, Jun Zhang, Liang-yin Kuo and so on.

My sincere thanks to my family and friends. They offered me spiritual support through these years. My special thanks to my father, who is always there for me. I would like to pay my special regards to my mother, even though she passed away six years ago, but I know she is always there with me. I also want to thank my boyfriend, who always knows how to release my pressure. Last but not least, I would like to thank all my friends, and your friendship is my precise.

Appendix

Load application under 0 V/cm at the relative density of 80 % with the pressure of 1.2 MPa

time	axial strain	radial strain	relative density	radial strain rate	axial strain rate
1.00E-11	-0.07945	-0.08354	79.4	-3.54E-05	-4.94E-05
1.26E+00	-0.07948	-0.08359	79.5	-3.54E-05	-4.93E-05
2.516	-0.07966	-0.08365	79.5	-3.53E-05	-4.92E-05
3.773	-0.07965	-0.08369	79.5	-3.53E-05	-4.92E-05
5.03	-0.0797	-0.0838	79.5	-3.53E-05	-4.91E-05
6.288	-0.0798	-0.08382	79.5	-3.52E-05	-4.91E-05
7.545	-0.0797	-0.08378	79.5	-3.52E-05	-4.90E-05
8.802	-0.07989	-0.08386	79.5	-3.52E-05	-4.89E-05
10.06	-0.07981	-0.08396	79.5	-3.51E-05	-4.89E-05
11.317	-0.07994	-0.08392	79.5	-3.51E-05	-4.88E-05
12.575	-0.08016	-0.08398	79.6	-3.51E-05	-4.88E-05
13.832	-0.08013	-0.08395	79.6	-3.50E-05	-4.87E-05
15.096	-0.0802	-0.08416	79.6	-3.50E-05	-4.86E-05
16.346	-0.08025	-0.08416	79.6	-3.49E-05	-4.86E-05
17.605	-0.08028	-0.08419	79.6	-3.49E-05	-4.85E-05
18.862	-0.08037	-0.08417	79.6	-3.49E-05	-4.85E-05
20.119	-0.08046	-0.08426	79.6	-3.48E-05	-4.84E-05
21.376	-0.08051	-0.08437	79.7	-3.48E-05	-4.83E-05
22.635	-0.08056	-0.08426	79.6	-3.48E-05	-4.83E-05
23.894	-0.0806	-0.08436	79.7	-3.47E-05	-4.82E-05
25.149	-0.08063	-0.08444	79.7	-3.47E-05	-4.81E-05
26.407	-0.08076	-0.08454	79.7	-3.46E-05	-4.81E-05
27.663	-0.08081	-0.08448	79.7	-3.46E-05	-4.80E-05
28.922	-0.08085	-0.08451	79.7	-3.45E-05	-4.79E-05
30.178	-0.08096	-0.08461	79.7	-3.45E-05	-4.79E-05
31.436	-0.08088	-0.0847	79.7	-3.45E-05	-4.78E-05
32.693	-0.08101	-0.0847	79.8	-3.44E-05	-4.77E-05
33.957	-0.08115	-0.0847	79.8	-3.44E-05	-4.77E-05
35.208	-0.0812	-0.08481	79.8	-3.43E-05	-4.76E-05
36.465	-0.08123	-0.08479	79.8	-3.43E-05	-4.75E-05
37.723	-0.08126	-0.08494	79.8	-3.43E-05	-4.75E-05
38.98	-0.08138	-0.08505	79.8	-3.42E-05	-4.74E-05
40.238	-0.08138	-0.08497	79.8	-3.42E-05	-4.73E-05
41.495	-0.08141	-0.08506	79.8	-3.41E-05	-4.73E-05
42.753	-0.08151	-0.08502	79.8	-3.41E-05	-4.72E-05
44.011	-0.08154	-0.08507	79.9	-3.40E-05	-4.71E-05
45.267	-0.0817	-0.08514	79.9	-3.40E-05	-4.71E-05
46.525	-0.08176	-0.08524	79.9	-3.39E-05	-4.70E-05

47.782	-0.08186	-0.08517	79.9	-3.39E-05	-4.69E-05
49.04	-0.08183	-0.08527	79.9	-3.39E-05	-4.69E-05
50.297	-0.08195	-0.08536	79.9	-3.38E-05	-4.68E-05
51.553	-0.08189	-0.08538	79.9	-3.38E-05	-4.67E-05
52.812	-0.08196	-0.08533	79.9	-3.37E-05	-4.67E-05
54.068	-0.08206	-0.08529	79.9	-3.37E-05	-4.66E-05
55.326	-0.08217	-0.08539	80.0	-3.36E-05	-4.65E-05
56.584	-0.08235	-0.08541	80.0	-3.36E-05	-4.65E-05
57.841	-0.08222	-0.08555	80.0	-3.35E-05	-4.64E-05
59.099	-0.08237	-0.08555	80.0	-3.35E-05	-4.63E-05
60.356	-0.08235	-0.08555	80.0	-3.34E-05	-4.63E-05
61.611	-0.08242	-0.08567	80.0	-3.34E-05	-4.62E-05
62.87	-0.08239	-0.08571	80.0	-3.34E-05	-4.61E-05
64.133	-0.08255	-0.08586	80.1	-3.33E-05	-4.61E-05
65.385	-0.08261	-0.0858	80.1	-3.33E-05	-4.60E-05
66.643	-0.08262	-0.08577	80.0	-3.32E-05	-4.59E-05
67.899	-0.08269	-0.08594	80.1	-3.32E-05	-4.58E-05
69.157	-0.08277	-0.08592	80.1	-3.31E-05	-4.58E-05
70.414	-0.08274	-0.08602	80.1	-3.31E-05	-4.57E-05
71.672	-0.08286	-0.08601	80.1	-3.30E-05	-4.56E-05
72.93	-0.08291	-0.08607	80.1	-3.30E-05	-4.56E-05
74.189	-0.08295	-0.08609	80.1	-3.29E-05	-4.55E-05
75.443	-0.08307	-0.08614	80.1	-3.29E-05	-4.54E-05
76.701	-0.08312	-0.08628	80.2	-3.28E-05	-4.54E-05
77.96	-0.08319	-0.08631	80.2	-3.28E-05	-4.53E-05
79.217	-0.08326	-0.08624	80.2	-3.27E-05	-4.52E-05
80.473	-0.08327	-0.08633	80.2	-3.27E-05	-4.52E-05
81.731	-0.08331	-0.08629	80.2	-3.26E-05	-4.51E-05
82.99	-0.08338	-0.08637	80.2	-3.26E-05	-4.50E-05
84.247	-0.08345	-0.0864	80.2	-3.26E-05	-4.49E-05
85.504	-0.08353	-0.08648	80.2	-3.25E-05	-4.49E-05
86.76	-0.08358	-0.08649	80.2	-3.25E-05	-4.48E-05
88.018	-0.08358	-0.08651	80.2	-3.24E-05	-4.47E-05
89.276	-0.08361	-0.0866	80.3	-3.24E-05	-4.47E-05
90.533	-0.08371	-0.08666	80.3	-3.23E-05	-4.46E-05
91.789	-0.08385	-0.08665	80.3	-3.23E-05	-4.45E-05
93.047	-0.08382	-0.08666	80.3	-3.22E-05	-4.45E-05
94.305	-0.08389	-0.08666	80.3	-3.22E-05	-4.44E-05
95.561	-0.0839	-0.08674	80.3	-3.21E-05	-4.43E-05
96.82	-0.08399	-0.08695	80.3	-3.21E-05	-4.43E-05
98.077	-0.084	-0.08684	80.3	-3.20E-05	-4.42E-05
99.335	-0.08405	-0.08698	80.4	-3.20E-05	-4.41E-05
100.591	-0.08404	-0.08698	80.4	-3.19E-05	-4.40E-05
101.849	-0.08413	-0.08707	80.4	-3.19E-05	-4.40E-05
103.106	-0.08416	-0.08704	80.4	-3.18E-05	-4.39E-05

104.364	-0.08426	-0.08707	80.4	-3.18E-05	-4.38E-05
105.622	-0.08429	-0.0872	80.4	-3.17E-05	-4.38E-05
106.878	-0.08438	-0.08711	80.4	-3.17E-05	-4.37E-05
108.162	-0.08442	-0.08728	80.4	-3.17E-05	-4.36E-05
109.412	-0.08446	-0.08714	80.4	-3.16E-05	-4.36E-05
110.666	-0.08455	-0.0872	80.4	-3.16E-05	-4.35E-05
111.917	-0.08463	-0.0873	80.5	-3.15E-05	-4.34E-05
113.166	-0.08466	-0.08736	80.5	-3.15E-05	-4.34E-05
114.422	-0.08473	-0.08736	80.5	-3.14E-05	-4.33E-05
115.684	-0.08474	-0.08747	80.5	-3.14E-05	-4.32E-05
116.938	-0.08483	-0.08747	80.5	-3.13E-05	-4.32E-05
118.195	-0.08485	-0.08757	80.5	-3.13E-05	-4.31E-05
119.452	-0.08494	-0.08757	80.5	-3.12E-05	-4.30E-05
120.709	-0.08498	-0.08756	80.5	-3.12E-05	-4.30E-05
121.967	-0.08508	-0.08766	80.6	-3.11E-05	-4.29E-05
123.225	-0.08523	-0.08758	80.5	-3.11E-05	-4.28E-05
124.481	-0.08519	-0.08774	80.6	-3.10E-05	-4.28E-05
125.739	-0.08522	-0.08773	80.6	-3.10E-05	-4.27E-05
126.997	-0.08528	-0.08775	80.6	-3.10E-05	-4.26E-05
128.254	-0.0854	-0.08787	80.6	-3.09E-05	-4.26E-05
129.52	-0.0854	-0.08787	80.6	-3.09E-05	-4.25E-05
130.768	-0.08542	-0.08785	80.6	-3.08E-05	-4.24E-05
132.027	-0.08546	-0.08794	80.6	-3.08E-05	-4.24E-05
133.283	-0.08549	-0.08797	80.6	-3.07E-05	-4.23E-05
134.54	-0.08563	-0.08804	80.7	-3.07E-05	-4.22E-05
135.797	-0.08573	-0.08804	80.7	-3.06E-05	-4.22E-05
137.056	-0.08574	-0.0881	80.7	-3.06E-05	-4.21E-05
138.313	-0.08577	-0.08826	80.7	-3.05E-05	-4.20E-05
139.569	-0.08577	-0.08818	80.7	-3.05E-05	-4.20E-05
140.827	-0.08597	-0.08825	80.7	-3.05E-05	-4.19E-05
142.085	-0.08594	-0.08826	80.7	-3.04E-05	-4.19E-05
143.352	-0.08596	-0.08829	80.7	-3.04E-05	-4.18E-05
144.598	-0.0861	-0.08828	80.7	-3.03E-05	-4.17E-05
145.856	-0.0861	-0.08838	80.7	-3.03E-05	-4.17E-05
147.114	-0.08626	-0.08855	80.8	-3.02E-05	-4.16E-05
148.371	-0.08629	-0.08845	80.8	-3.02E-05	-4.15E-05
149.628	-0.08633	-0.08843	80.8	-3.01E-05	-4.15E-05
150.884	-0.08633	-0.08845	80.8	-3.01E-05	-4.14E-05
152.145	-0.0864	-0.08855	80.8	-3.01E-05	-4.13E-05
153.401	-0.08642	-0.08871	80.8	-3.00E-05	-4.13E-05
154.658	-0.08647	-0.08853	80.8	-3.00E-05	-4.12E-05
155.916	-0.0865	-0.08867	80.8	-2.99E-05	-4.12E-05
157.174	-0.08659	-0.08864	80.8	-2.99E-05	-4.11E-05
158.43	-0.0867	-0.08867	80.8	-2.98E-05	-4.10E-05
159.687	-0.08675	-0.08882	80.9	-2.98E-05	-4.10E-05

160.946	-0.08671	-0.0888	80.9	-2.98E-05	-4.09E-05
162.202	-0.0867	-0.0888	80.9	-2.97E-05	-4.08E-05
163.46	-0.08675	-0.08884	80.9	-2.97E-05	-4.08E-05
164.717	-0.08679	-0.08893	80.9	-2.96E-05	-4.07E-05
165.974	-0.08689	-0.08888	80.9	-2.96E-05	-4.07E-05
167.231	-0.08697	-0.08901	80.9	-2.96E-05	-4.06E-05
168.488	-0.08709	-0.08905	80.9	-2.95E-05	-4.05E-05
169.746	-0.08704	-0.08912	80.9	-2.95E-05	-4.05E-05
171.005	-0.08717	-0.08908	80.9	-2.94E-05	-4.04E-05
172.262	-0.08711	-0.08911	80.9	-2.94E-05	-4.04E-05
173.518	-0.08726	-0.08921	81.0	-2.93E-05	-4.03E-05
174.775	-0.08729	-0.08923	81.0	-2.93E-05	-4.02E-05
176.033	-0.0873	-0.08926	81.0	-2.93E-05	-4.02E-05
177.291	-0.08729	-0.08924	81.0	-2.92E-05	-4.01E-05
178.553	-0.08744	-0.08938	81.0	-2.92E-05	-4.01E-05
179.804	-0.08743	-0.08937	81.0	-2.91E-05	-4.00E-05
181.062	-0.0875	-0.08947	81.0	-2.91E-05	-3.99E-05
182.32	-0.0876	-0.08944	81.0	-2.91E-05	-3.99E-05
183.577	-0.0876	-0.08941	81.0	-2.90E-05	-3.98E-05
184.834	-0.08761	-0.08961	81.1	-2.90E-05	-3.98E-05
186.092	-0.0877	-0.08959	81.1	-2.89E-05	-3.97E-05
187.355	-0.08774	-0.08966	81.1	-2.89E-05	-3.97E-05
188.606	-0.08779	-0.08961	81.1	-2.89E-05	-3.96E-05
189.863	-0.08788	-0.08961	81.1	-2.88E-05	-3.95E-05
191.121	-0.08788	-0.08965	81.1	-2.88E-05	-3.95E-05
192.379	-0.08799	-0.08964	81.1	-2.87E-05	-3.94E-05
193.635	-0.08815	-0.08966	81.1	-2.87E-05	-3.94E-05
194.894	-0.08819	-0.08989	81.2	-2.87E-05	-3.93E-05
196.151	-0.08832	-0.08983	81.2	-2.86E-05	-3.93E-05
197.417	-0.08823	-0.08993	81.2	-2.86E-05	-3.92E-05
198.665	-0.08822	-0.08984	81.2	-2.86E-05	-3.91E-05
199.92	-0.08839	-0.08993	81.2	-2.85E-05	-3.91E-05
201.181	-0.0885	-0.08997	81.2	-2.85E-05	-3.90E-05

Load application under 14 V/cm at the relative density of 80 % with the pressure of 1.2 MPa

time	**axial strain**	**radial strain**	**relative density**	**radial strain rate**	**axial strain rate**
[s]			[%]	[1/s]	[1/s]
0	-0.08909	-0.08277	80.2	-5.00E-05	-8.92E-05
1.259	-0.08921	-0.08275	80.2	-5.00E-05	-8.91E-05
2.526	-0.08933	-0.08283	80.3	-5.01E-05	-8.90E-05
3.793	-0.08946	-0.08288	80.3	-5.02E-05	-8.90E-05
5.059	-0.09036	-0.08286	80.3	-5.02E-05	-8.89E-05
6.327	-0.09106	-0.08292	80.4	-5.03E-05	-8.88E-05
7.594	-0.09024	-0.08313	80.4	-5.03E-05	-8.88E-05
8.861	-0.09115	-0.08321	80.5	-5.03E-05	-8.87E-05
10.127	-0.0906	-0.08326	80.4	-5.04E-05	-8.86E-05
11.393	-0.09009	-0.0832	80.4	-5.04E-05	-8.86E-05
12.681	-0.09083	-0.08342	80.5	-5.04E-05	-8.85E-05
13.94	-0.09064	-0.08348	80.5	-5.04E-05	-8.85E-05
15.204	-0.09073	-0.08362	80.5	-5.04E-05	-8.84E-05
16.481	-0.09071	-0.08356	80.5	-5.04E-05	-8.83E-05
17.739	-0.09082	-0.08363	80.5	-5.03E-05	-8.83E-05
19.002	-0.09103	-0.0837	80.5	-5.03E-05	-8.82E-05
20.26	-0.0913	-0.08365	80.5	-5.03E-05	-8.81E-05
21.536	-0.09156	-0.08371	80.6	-5.03E-05	-8.80E-05
22.796	-0.09166	-0.08394	80.6	-5.02E-05	-8.80E-05
24.063	-0.09157	-0.08397	80.6	-5.02E-05	-8.79E-05
25.33	-0.09188	-0.08405	80.7	-5.01E-05	-8.78E-05
26.6	-0.09157	-0.08415	80.6	-5.01E-05	-8.77E-05
27.862	-0.09166	-0.08416	80.7	-5.00E-05	-8.76E-05
29.13	-0.09182	-0.08421	80.7	-5.00E-05	-8.75E-05
30.396	-0.0922	-0.08428	80.7	-4.99E-05	-8.74E-05
31.661	-0.09228	-0.08412	80.7	-4.98E-05	-8.73E-05
32.93	-0.09216	-0.0843	80.7	-4.97E-05	-8.72E-05
34.198	-0.09216	-0.08443	80.7	-4.97E-05	-8.71E-05
35.464	-0.09251	-0.08451	80.8	-4.96E-05	-8.70E-05
36.73	-0.09248	-0.08459	80.8	-4.95E-05	-8.69E-05
37.996	-0.09285	-0.08453	80.8	-4.94E-05	-8.68E-05
39.265	-0.09309	-0.0847	80.9	-4.93E-05	-8.66E-05
40.53	-0.09325	-0.08476	80.9	-4.93E-05	-8.65E-05
41.798	-0.09348	-0.08486	80.9	-4.92E-05	-8.64E-05
43.07	-0.09358	-0.08493	80.9	-4.91E-05	-8.62E-05
44.332	-0.09354	-0.08494	80.9	-4.90E-05	-8.61E-05
45.6	-0.0935	-0.08499	80.9	-4.89E-05	-8.59E-05
46.864	-0.0935	-0.08503	80.9	-4.88E-05	-8.58E-05
48.131	-0.09341	-0.08506	81.0	-4.87E-05	-8.56E-05
49.398	-0.09377	-0.08521	81.0	-4.86E-05	-8.55E-05
50.666	-0.09424	-0.08546	81.0	-4.85E-05	-8.53E-05

51.93	-0.09427	-0.08509	81.1	-4.84E-05	-8.51E-05
53.198	-0.09438	-0.08543	81.1	-4.83E-05	-8.49E-05
54.466	-0.09471	-0.08551	81.1	-4.82E-05	-8.47E-05
55.733	-0.09442	-0.08558	81.1	-4.80E-05	-8.45E-05
56.997	-0.09447	-0.08558	81.1	-4.79E-05	-8.44E-05
58.267	-0.09442	-0.08571	81.1	-4.78E-05	-8.41E-05
59.532	-0.09434	-0.08565	81.1	-4.77E-05	-8.39E-05
60.8	-0.09456	-0.08587	81.1	-4.76E-05	-8.37E-05
62.065	-0.09481	-0.08582	81.2	-4.75E-05	-8.35E-05
63.334	-0.09514	-0.08589	81.2	-4.74E-05	-8.33E-05
64.602	-0.09509	-0.086	81.2	-4.73E-05	-8.30E-05
65.868	-0.09528	-0.08607	81.2	-4.72E-05	-8.28E-05
67.133	-0.0957	-0.08601	81.3	-4.71E-05	-8.25E-05
68.4	-0.09544	-0.08607	81.2	-4.69E-05	-8.23E-05
69.666	-0.09552	-0.086	81.3	-4.68E-05	-8.20E-05
70.935	-0.0958	-0.08615	81.3	-4.67E-05	-8.18E-05
72.201	-0.0958	-0.08628	81.3	-4.66E-05	-8.15E-05
73.468	-0.09605	-0.08629	81.4	-4.65E-05	-8.12E-05
74.743	-0.09614	-0.08646	81.4	-4.64E-05	-8.09E-05
76.001	-0.09576	-0.08646	81.4	-4.63E-05	-8.07E-05
77.267	-0.09609	-0.0865	81.4	-4.62E-05	-8.04E-05
78.536	-0.09615	-0.08658	81.4	-4.61E-05	-8.01E-05
79.803	-0.09632	-0.08673	81.4	-4.60E-05	-7.98E-05
81.068	-0.09643	-0.08671	81.4	-4.59E-05	-7.95E-05
82.334	-0.09666	-0.08668	81.5	-4.58E-05	-7.91E-05
83.604	-0.09678	-0.08687	81.5	-4.57E-05	-7.88E-05
84.871	-0.09691	-0.08701	81.5	-4.56E-05	-7.85E-05
86.135	-0.0971	-0.08695	81.5	-4.55E-05	-7.82E-05
87.401	-0.09721	-0.08699	81.6	-4.54E-05	-7.78E-05
88.678	-0.09689	-0.08699	81.5	-4.53E-05	-7.75E-05
89.936	-0.09703	-0.08703	81.6	-4.52E-05	-7.72E-05
91.204	-0.09684	-0.08715	81.6	-4.51E-05	-7.68E-05
92.47	-0.09686	-0.08717	81.6	-4.50E-05	-7.65E-05
93.737	-0.09699	-0.08717	81.6	-4.49E-05	-7.61E-05
95.004	-0.09747	-0.08729	81.6	-4.48E-05	-7.57E-05
96.271	-0.09767	-0.08737	81.7	-4.47E-05	-7.54E-05
97.535	-0.09775	-0.08737	81.7	-4.46E-05	-7.50E-05
98.805	-0.09789	-0.08751	81.7	-4.45E-05	-7.46E-05
100.072	-0.09805	-0.08758	81.7	-4.44E-05	-7.43E-05
101.338	-0.09815	-0.08761	81.7	-4.43E-05	-7.39E-05
102.603	-0.09796	-0.08754	81.7	-4.43E-05	-7.35E-05
103.879	-0.09824	-0.08768	81.7	-4.42E-05	-7.31E-05
105.137	-0.09837	-0.08759	81.8	-4.41E-05	-7.27E-05
106.406	-0.09858	-0.08791	81.8	-4.40E-05	-7.23E-05
107.673	-0.09844	-0.08792	81.8	-4.39E-05	-7.20E-05

108.936	-0.09864	-0.08781	81.8	-4.38E-05	-7.16E-05
110.205	-0.0988	-0.08798	81.9	-4.38E-05	-7.12E-05
111.473	-0.09893	-0.08805	81.9	-4.37E-05	-7.08E-05
112.739	-0.09862	-0.0881	81.9	-4.36E-05	-7.04E-05
114.004	-0.09903	-0.0881	81.9	-4.35E-05	-7.00E-05
115.283	-0.09878	-0.08816	81.9	-4.35E-05	-6.96E-05
116.541	-0.09912	-0.08838	81.9	-4.34E-05	-6.92E-05
117.805	-0.09932	-0.08843	82.0	-4.33E-05	-6.88E-05
119.072	-0.09922	-0.08839	82.0	-4.33E-05	-6.84E-05
120.35	-0.09892	-0.0885	81.9	-4.32E-05	-6.80E-05
121.605	-0.0997	-0.08849	82.0	-4.31E-05	-6.76E-05
122.874	-0.09988	-0.08874	82.0	-4.30E-05	-6.72E-05
124.138	-0.09994	-0.08864	82.1	-4.30E-05	-6.68E-05
125.407	-0.10046	-0.08876	82.1	-4.29E-05	-6.64E-05
126.674	-0.09979	-0.08878	82.0	-4.28E-05	-6.60E-05
127.938	-0.09979	-0.0886	82.1	-4.28E-05	-6.56E-05
129.206	-0.09976	-0.08877	82.1	-4.27E-05	-6.52E-05
130.473	-0.09967	-0.08881	82.1	-4.27E-05	-6.48E-05
131.741	-0.10066	-0.08902	82.1	-4.26E-05	-6.44E-05
133.006	-0.10058	-0.0889	82.1	-4.25E-05	-6.40E-05
134.273	-0.10032	-0.08892	82.2	-4.25E-05	-6.36E-05
135.541	-0.10017	-0.08927	82.1	-4.24E-05	-6.33E-05
136.807	-0.10015	-0.08909	82.1	-4.23E-05	-6.29E-05
138.072	-0.10035	-0.08915	82.2	-4.23E-05	-6.25E-05
139.343	-0.10067	-0.08934	82.2	-4.22E-05	-6.21E-05
140.607	-0.10057	-0.08928	82.2	-4.21E-05	-6.18E-05
141.875	-0.10048	-0.08946	82.2	-4.21E-05	-6.14E-05
143.14	-0.10079	-0.08934	82.2	-4.20E-05	-6.11E-05
144.407	-0.10125	-0.08934	82.3	-4.20E-05	-6.07E-05
145.676	-0.10132	-0.08963	82.3	-4.19E-05	-6.04E-05
146.941	-0.10091	-0.08954	82.3	-4.18E-05	-6.01E-05
148.209	-0.10111	-0.08964	82.3	-4.18E-05	-5.98E-05
149.477	-0.10126	-0.08965	82.3	-4.17E-05	-5.95E-05
150.744	-0.10099	-0.08976	82.3	-4.16E-05	-5.92E-05
152.008	-0.10123	-0.08975	82.3	-4.15E-05	-5.89E-05
153.275	-0.10176	-0.08972	82.4	-4.15E-05	-5.86E-05
154.542	-0.10179	-0.09007	82.4	-4.14E-05	-5.83E-05
155.809	-0.10173	-0.08992	82.4	-4.13E-05	-5.80E-05
157.075	-0.10158	-0.08981	82.4	-4.12E-05	-5.78E-05
158.348	-0.10173	-0.08998	82.4	-4.12E-05	-5.75E-05
159.611	-0.10217	-0.09013	82.5	-4.11E-05	-5.73E-05
160.878	-0.1022	-0.09016	82.5	-4.10E-05	-5.71E-05
162.143	-0.10194	-0.09018	82.5	-4.09E-05	-5.69E-05
163.41	-0.1025	-0.09021	82.5	-4.08E-05	-5.67E-05
164.678	-0.10235	-0.09026	82.5	-4.07E-05	-5.65E-05

165.944	-0.10208	-0.09047	82.5	-4.06E-05	-5.63E-05
167.209	-0.10199	-0.09034	82.5	-4.05E-05	-5.62E-05
168.476	-0.10196	-0.09044	82.5	-4.04E-05	-5.60E-05
169.742	-0.1021	-0.09044	82.5	-4.03E-05	-5.59E-05
171.01	-0.1021	-0.09054	82.5	-4.02E-05	-5.58E-05
172.279	-0.10221	-0.09059	82.6	-4.01E-05	-5.57E-05
173.545	-0.10231	-0.0906	82.6	-4.00E-05	-5.56E-05
174.812	-0.10238	-0.09068	82.6	-3.99E-05	-5.56E-05

Load application under 28 V/cm at the relative density of 80 % with the pressure of 1.2 MPa

time	**axial strain**	**radial strain**	**relative density**	**radial strain rate**	**axial strain rate**
[s]			[%]	[1/s]	[1/s]
0	-0.08686	-0.0855	80.3	-9.31E-05	-1.11E-04
1.258	-0.08696	-0.08562	80.3	-9.35E-05	-1.11E-04
2.517	-0.08732	-0.0857	80.3	-9.38E-05	-1.11E-04
3.776	-0.08759	-0.08584	80.4	-9.41E-05	-1.12E-04
5.032	-0.08759	-0.08591	80.4	-9.43E-05	-1.12E-04
6.29	-0.08815	-0.08602	80.5	-9.46E-05	-1.12E-04
7.549	-0.08819	-0.08612	80.5	-9.48E-05	-1.12E-04
8.807	-0.0881	-0.08625	80.5	-9.50E-05	-1.12E-04
10.063	-0.08823	-0.08631	80.5	-9.52E-05	-1.12E-04
11.32	-0.08843	-0.08645	80.6	-9.53E-05	-1.13E-04
12.579	-0.08895	-0.08657	80.6	-9.55E-05	-1.13E-04
13.838	-0.08893	-0.08671	80.6	-9.56E-05	-1.13E-04
15.096	-0.08883	-0.08685	80.6	-9.56E-05	-1.13E-04
16.353	-0.0887	-0.08696	80.7	-9.57E-05	-1.13E-04
17.611	-0.0891	-0.08715	80.7	-9.58E-05	-1.13E-04
18.869	-0.08894	-0.08725	80.7	-9.58E-05	-1.13E-04
20.127	-0.08942	-0.08734	80.8	-9.58E-05	-1.13E-04
21.385	-0.08962	-0.08742	80.8	-9.58E-05	-1.13E-04
22.642	-0.08967	-0.08753	80.8	-9.57E-05	-1.13E-04
23.902	-0.08986	-0.0876	80.9	-9.57E-05	-1.13E-04
25.159	-0.09006	-0.08784	80.9	-9.56E-05	-1.13E-04
26.416	-0.09031	-0.08809	81.0	-9.55E-05	-1.13E-04
27.674	-0.09033	-0.08816	81.0	-9.54E-05	-1.13E-04
28.931	-0.09031	-0.0883	81.0	-9.53E-05	-1.13E-04
30.191	-0.09051	-0.08834	81.0	-9.52E-05	-1.13E-04
31.448	-0.09054	-0.0884	81.1	-9.50E-05	-1.13E-04
32.706	-0.09072	-0.08861	81.1	-9.49E-05	-1.13E-04
33.963	-0.09074	-0.08871	81.1	-9.47E-05	-1.12E-04
35.221	-0.09082	-0.08883	81.1	-9.45E-05	-1.12E-04
36.481	-0.09103	-0.08889	81.1	-9.43E-05	-1.12E-04
37.738	-0.09119	-0.08894	81.2	-9.41E-05	-1.12E-04
38.995	-0.09147	-0.08915	81.2	-9.38E-05	-1.12E-04
40.257	-0.09185	-0.08931	81.3	-9.36E-05	-1.12E-04
41.511	-0.09164	-0.08932	81.3	-9.34E-05	-1.11E-04
42.769	-0.09189	-0.08948	81.3	-9.31E-05	-1.11E-04
44.028	-0.09201	-0.08961	81.3	-9.28E-05	-1.11E-04
45.285	-0.09218	-0.08966	81.4	-9.25E-05	-1.11E-04
46.542	-0.0924	-0.08989	81.4	-9.22E-05	-1.10E-04
47.801	-0.09255	-0.09001	81.4	-9.19E-05	-1.10E-04
49.059	-0.09234	-0.08997	81.5	-9.16E-05	-1.10E-04
50.317	-0.09268	-0.09022	81.5	-9.13E-05	-1.10E-04

51.574	-0.09293	-0.0903	81.5	-9.10E-05	-1.09E-04
52.831	-0.093	-0.09046	81.6	-9.07E-05	-1.09E-04
54.09	-0.09297	-0.0906	81.6	-9.03E-05	-1.09E-04
55.348	-0.09312	-0.09076	81.6	-9.00E-05	-1.08E-04
56.606	-0.0934	-0.09078	81.7	-8.96E-05	-1.08E-04
57.867	-0.09345	-0.09087	81.7	-8.92E-05	-1.08E-04
59.154	-0.09391	-0.09097	81.7	-8.89E-05	-1.07E-04
60.402	-0.09417	-0.09112	81.8	-8.85E-05	-1.07E-04
61.658	-0.09388	-0.09127	81.8	-8.81E-05	-1.07E-04
62.906	-0.09392	-0.0914	81.8	-8.77E-05	-1.06E-04
64.164	-0.09416	-0.09147	81.8	-8.74E-05	-1.06E-04
65.423	-0.09452	-0.09151	81.9	-8.70E-05	-1.05E-04
66.677	-0.09486	-0.09168	81.9	-8.66E-05	-1.05E-04
67.927	-0.09506	-0.09177	81.9	-8.62E-05	-1.05E-04
69.184	-0.095	-0.09175	82.0	-8.58E-05	-1.04E-04
70.441	-0.09498	-0.09198	82.0	-8.54E-05	-1.04E-04
71.7	-0.09483	-0.09217	82.0	-8.50E-05	-1.03E-04
72.959	-0.09518	-0.09219	82.0	-8.45E-05	-1.03E-04
74.215	-0.09521	-0.09225	82.0	-8.41E-05	-1.03E-04
75.473	-0.09544	-0.09236	82.1	-8.37E-05	-1.02E-04
76.732	-0.09574	-0.09248	82.1	-8.33E-05	-1.02E-04
77.99	-0.09561	-0.09264	82.1	-8.29E-05	-1.01E-04
79.247	-0.09586	-0.09263	82.2	-8.25E-05	-1.01E-04
80.504	-0.09594	-0.09282	82.2	-8.21E-05	-1.00E-04
81.764	-0.09608	-0.09287	82.2	-8.16E-05	-9.98E-05
83.023	-0.09619	-0.09299	82.2	-8.12E-05	-9.93E-05
84.28	-0.09645	-0.09312	82.3	-8.08E-05	-9.88E-05
85.537	-0.0968	-0.09321	82.3	-8.04E-05	-9.83E-05
86.795	-0.09667	-0.09332	82.3	-8.00E-05	-9.78E-05
88.053	-0.09677	-0.09347	82.4	-7.96E-05	-9.73E-05
89.31	-0.09678	-0.09351	82.4	-7.91E-05	-9.68E-05
90.569	-0.09677	-0.09358	82.4	-7.87E-05	-9.63E-05
91.826	-0.09686	-0.09371	82.4	-7.83E-05	-9.59E-05
93.085	-0.09696	-0.09385	82.4	-7.79E-05	-9.54E-05
94.342	-0.097	-0.09395	82.5	-7.75E-05	-9.49E-05
95.601	-0.09718	-0.09404	82.5	-7.71E-05	-9.44E-05
96.859	-0.09739	-0.09412	82.5	-7.67E-05	-9.38E-05
98.115	-0.09742	-0.09419	82.6	-7.63E-05	-9.33E-05
99.373	-0.0978	-0.09436	82.6	-7.59E-05	-9.28E-05
100.632	-0.09787	-0.0944	82.6	-7.55E-05	-9.23E-05
101.89	-0.09797	-0.09446	82.6	-7.51E-05	-9.18E-05
103.149	-0.09835	-0.09457	82.7	-7.47E-05	-9.13E-05
104.405	-0.09823	-0.09467	82.7	-7.43E-05	-9.09E-05
105.664	-0.09846	-0.09467	82.7	-7.39E-05	-9.04E-05
106.922	-0.09871	-0.09486	82.8	-7.36E-05	-8.99E-05

108.179	-0.09871	-0.09512	82.8	-7.32E-05	-8.94E-05
109.437	-0.09873	-0.09506	82.8	-7.28E-05	-8.89E-05
110.693	-0.09882	-0.09513	82.8	-7.25E-05	-8.84E-05
111.953	-0.09866	-0.09526	82.8	-7.21E-05	-8.79E-05
113.211	-0.09873	-0.09533	82.8	-7.17E-05	-8.75E-05
114.468	-0.09914	-0.0954	82.9	-7.14E-05	-8.70E-05
115.726	-0.09931	-0.09541	82.9	-7.10E-05	-8.65E-05
116.984	-0.09941	-0.09565	82.9	-7.07E-05	-8.61E-05
118.242	-0.09946	-0.09562	83.0	-7.04E-05	-8.56E-05
119.5	-0.09955	-0.09576	83.0	-7.00E-05	-8.52E-05
120.757	-0.0994	-0.09583	83.0	-6.97E-05	-8.47E-05
122.015	-0.09957	-0.09587	83.0	-6.94E-05	-8.43E-05
123.277	-0.09987	-0.09607	83.0	-6.91E-05	-8.39E-05
124.532	-0.09984	-0.09612	83.1	-6.88E-05	-8.35E-05
125.79	-0.10003	-0.09619	83.1	-6.84E-05	-8.31E-05
127.047	-0.10017	-0.09622	83.1	-6.81E-05	-8.27E-05
128.305	-0.10059	-0.09629	83.2	-6.79E-05	-8.23E-05
129.563	-0.10014	-0.0965	83.2	-6.76E-05	-8.19E-05
130.822	-0.10037	-0.09661	83.2	-6.73E-05	-8.15E-05
132.079	-0.10068	-0.09667	83.2	-6.70E-05	-8.12E-05
133.336	-0.10092	-0.0968	83.3	-6.67E-05	-8.09E-05
134.594	-0.10082	-0.09683	83.3	-6.65E-05	-8.05E-05
135.852	-0.101	-0.09687	83.3	-6.62E-05	-8.02E-05
137.11	-0.10111	-0.09694	83.3	-6.60E-05	-7.99E-05
138.367	-0.10108	-0.09711	83.3	-6.57E-05	-7.96E-05
139.625	-0.10116	-0.09719	83.4	-6.55E-05	-7.93E-05
140.883	-0.10116	-0.09735	83.4	-6.52E-05	-7.91E-05
142.142	-0.10153	-0.09738	83.4	-6.50E-05	-7.88E-05
143.4	-0.10145	-0.09743	83.4	-6.48E-05	-7.86E-05
144.657	-0.1015	-0.09744	83.4	-6.46E-05	-7.84E-05
145.914	-0.10187	-0.09754	83.5	-6.44E-05	-7.82E-05
147.173	-0.10174	-0.09761	83.5	-6.42E-05	-7.80E-05
148.432	-0.10182	-0.0978	83.5	-6.40E-05	-7.78E-05
149.688	-0.1017	-0.09776	83.5	-6.38E-05	-7.77E-05
150.945	-0.10201	-0.0979	83.5	-6.36E-05	-7.76E-05
152.204	-0.1023	-0.09791	83.6	-6.34E-05	-7.75E-05
153.463	-0.10228	-0.09804	83.6	-6.33E-05	-7.74E-05
154.721	-0.10235	-0.09805	83.6	-6.31E-05	-7.73E-05
155.977	-0.10262	-0.09815	83.6	-6.29E-05	-7.73E-05
157.236	-0.10262	-0.09831	83.6	-6.28E-05	-7.72E-05
158.497	-0.10273	-0.09834	83.7	-6.26E-05	-7.72E-05
159.751	-0.10281	-0.0983	83.7	-6.25E-05	-7.72E-05
161.008	-0.10292	-0.09847	83.7	-6.24E-05	-7.73E-05
162.267	-0.10283	-0.09855	83.7	-6.22E-05	-7.74E-05
163.524	-0.10296	-0.09868	83.7	-6.21E-05	-7.74E-05

164.783	-0.10315	-0.09867	83.8	-6.20E-05	-7.76E-05
166.041	-0.10315	-0.0988	83.8	-6.19E-05	-7.77E-05
167.297	-0.10322	-0.0989	83.8	-6.18E-05	-7.79E-05
168.556	-0.10358	-0.09893	83.8	-6.17E-05	-7.81E-05
169.816	-0.10364	-0.099	83.9	-6.16E-05	-7.83E-05
171.072	-0.10361	-0.09916	83.9	-6.15E-05	-7.85E-05
172.33	-0.1037	-0.09924	83.9	-6.14E-05	-7.88E-05
173.588	-0.10393	-0.09933	83.9	-6.13E-05	-7.91E-05
174.846	-0.10403	-0.09946	83.9	-6.12E-05	-7.94E-05
176.106	-0.10417	-0.09941	84.0	-6.11E-05	-7.98E-05
177.361	-0.10412	-0.09956	84.0	-6.11E-05	-8.02E-05
178.619	-0.10433	-0.09953	84.0	-6.10E-05	-8.06E-05
179.876	-0.10441	-0.0997	84.0	-6.09E-05	-8.11E-05
181.134	-0.10435	-0.09954	84.0	-6.09E-05	-8.16E-05
182.392	-0.10443	-0.09975	84.1	-6.08E-05	-8.21E-05
183.651	-0.1047	-0.09993	84.1	-6.08E-05	-8.27E-05
184.908	-0.10453	-0.09991	84.1	-6.07E-05	-8.33E-05
186.166	-0.10485	-0.09999	84.1	-6.07E-05	-8.39E-05
187.425	-0.10503	-0.10011	84.2	-6.07E-05	-8.46E-05
188.683	-0.10523	-0.10027	84.2	-6.06E-05	-8.53E-05
189.939	-0.10517	-0.10035	84.2	-6.06E-05	-8.60E-05
191.197	-0.10521	-0.10039	84.2	-6.06E-05	-8.68E-05

Reference

[1]. M.N. Rahaman, Ceramic Processing and Sintering. CRC Taylor & Francis, Boca Raton, Fla., 2007.

[2]. O. Guillon, C. Elsässer, O. Gutfleisch, J. Janek, S. Korte-Kerzel, D. Raabe, C.A. Volkert, Manipulation of matter by electric and magnetic fields: Toward novel synthesis and processing routes of inorganic materials, Mater. Today. 21(2018) 527-536.

[3]. M. Biesuz, V.M. Sglavo, Flash sintering of ceramics, J. Eur. Ceram. Soc. 39(2019) 115-143.

[4]. O. Guillon, J. Gonzalez-Julian, B. Dargatz, T. Kessel, G. Schierning, J. Räthel, M. Herrmann, Field-Assisted Sintering Technology/Spark Plasma Sintering: Mechanisms, Materials, and Technology Developments, Adv. Eng. Mater. 16(2014) 830-849.

[5]. J. Langer, M.J. Hoffmann, O. Guillon, Direct comparison between hot pressing and electric field-assisted sintering of submicron alumina, Acta Mater. 57(2009) 5454-5465.

[6]. J. Langer, M.J. Hoffmann, O. Guillon, Electric Field-Assisted Sintering in Comparison with the Hot Pressing of Yttria-Stabilized Zirconia, J. Am. Ceram. Soc. 94(2011) 24-31.

[7]. T.B. Holland, T.B. Tran, D.V. Quach, U. Anselmi-Tamburini, J.R. Groza, A.K. Mukherjee, Athermal and thermal mechanisms of sintering at high heating rates in the presence and absence of an externally applied field, J. Eur. Ceram. Soc. 32(2012) 3675-3683.

[8]. B. McWilliams, A. Zavaliangos, Multi-phenomena simulation of electric field assisted sintering, J. Mater. Sci. 43(2008) 5031-5035.

[9]. D. Schwesig, G. Schierning, R. Theissmann, N. Stein, N. Petermann, H. Wiggers, R. Schmechel, D.E. Wolf, From nanoparticles to nanocrystalline bulk: percolation effects in field assisted sintering of silicon nanoparticles, Nanotechnology. 22(2011) 135601.

[10]. R. Kirchheim, On the mixed ionic and electronic conductivity in polarized yttria stabilized zirconia, Solid State Ion. 320(2018) 239-258.

[11]. J. Chun, M. Martin, H.-I. Yoo, On the kinetic decomposition voltage of ternary oxides, PCCP. 20(2018) 2396-2402.

[12]. M. Cologna, B. Rashkova, R. Raj, Flash Sintering of Nanograin Zirconia in <5 s at 850°C, J. Am. Ceram. Soc. 93(2010) 3556-3559.

[13]. J.G. Pereira da Silva, J.M. Lebrun, H.A. Al-Qureshi, R. Janssen, R. Raj, Temperature Distributions During Flash Sintering of 8% Yttria-Stabilized Zirconia, J. Am. Ceram. Soc. 98(2015) 3525-3528.

[14]. Y. Zhang, J.-I. Jung, J. Luo, Thermal runaway, flash sintering and asymmetrical microstructural development of ZnO and ZnO–Bi_2O_3 under direct currents, Acta Mater. 94(2015) 87-100.

[15]. R.I. Todd, E. Zapata-Solvas, R.S. Bonilla, T. Sneddon, P.R. Wilshaw, Electrical characteristics of flash sintering: thermal runaway of Joule heating, J. Eur. Ceram. Soc. 35(2015) 1865-1877.

[16]. Y. Dong, I.W. Chen, Onset Criterion for Flash Sintering, J. Am. Ceram. Soc. 98(2015) 3624-3627.

[17]. J.G.P. Da Silva, H.A. Al-Qureshi, F. Keil, R. Janssen, A dynamic bifurcation criterion for thermal runaway during the flash sintering of ceramics, J. Eur. Ceram. Soc. 36(2016) 1261-1267.

[18]. W. Ji, B. Parker, S. Falco, J.Y. Zhang, Z.Y. Fu, R.I. Todd, Ultra-fast firing: Effect of heating rate on sintering of 3YSZ, with and without an electric field, J. Eur. Ceram. Soc. 37(2017) 2547-2551.

[19]. C. Schmerbauch, J. Gonzalez-Julian, R. Röder, C. Ronning, O. Guillon, Flash Sintering of Nanocrystalline Zinc Oxide and its Influence on Microstructure and Defect Formation, J. Am. Ceram. Soc. 97(2014) 1728-1735.

[20]. H. Conrad, D. Yang, Effect of the strength of an AC electric field compared to DC on the sintering rate and related grain size of zirconia (3Y-TZP), Mater. Sci. Eng. A. 559(2013) 591-594.

[21]. M. Schie, S. Menzel, J. Robertson, R. Waser, R.A. De Souza, Field-enhanced route to generating anti-Frenkel pairs in HfO_2, Phys. Rev. Mater. 2(2018) 035002.

[22]. D. Yang, H. Conrad, Enhanced sintering rate of zirconia (3Y-TZP) by application of a small AC electric field, Scripta Mater. 63(2010) 328-331.

[23]. D. Yang, H. Conrad, Enhanced sintering rate and finer grain size in yttria-stablized zirconia (3Y-TZP) with combined DC electric field and increased heating rate, Mater. Sci. Eng. A. 528(2011) 1221-1225.

[24]. L.C. De Jonghe, M.N. Rahaman, Sintering of Ceramics, in: F. Aldinger, N. Claussen, R.M. Spriggs, K. Uchino, K. Koumoto, and M. Kaneno, (Eds), Handbook of Advanced Ceramics, Academic Press, Oxford, 2003, pp. 187-264.

[25]. K. Benthem, R. Castro, Sintering: Mechanisms of Convention Nanodensification and Field Assisted Processes. Engineering Materials. Springer, Heidelberg, 2013.

[26]. F. Wakai, T. Akatsu, Y. Shinoda, Shrinkage and disappearance of a closed pore in the sintering of particle cluster, Acta Mater. 54(2006) 793-805.

[27]. F.F. Lange, Densification of powder compacts: An unfinished story, J. Eur. Ceram. Soc. 28(2008) 1509-1516.

[28]. E.B. Slamovich, F.F. Lange, Densification of Large Pores: I, Expriments, J. Am. Ceram. Soc. 75(1992) 2498-2508.

[29]. E.B. Slamovich, F.F. Lange, Densification of Large Pores: II, Driving Potentials and Kinetics, J. Am. Ceram. Soc. 76(1993) 1584-1590.

[30]. J. Wang, R. Raj, Estimate of the Activation Energies for Boundary Diffusion from Rate-Controlled Sintering of Pure Alumina, and Alumina Doped with Zirconia or Titania, J. Am. Ceram. Soc. 73(1990) 1172-1175.

[31]. H. Su, D.L. Johnson, Master Sintering Curve: A Practical Approach to Sintering, J. Am. Ceram. Soc. 79(1996) 3211-3217.

[32]. M. Aminzare, F. Golestani-fard, O. Guillon, M. Mazaheri, H.R. Rezaie, Sintering behavior of an ultrafine alumina powder shaped by pressure filtration and dry pressing, Mater. Sci. Eng. A. 527(2010) 3807-3812.

[33]. J. Langer, Vergleich der durch das elektrische Feld aktivierten Sintertechnologie mit dem Heißpressverfahren anhand von Oxidkeramiken, in Material- und Geowissenschaften. Technische Universität Darmstadt: Darmstadt.

[34]. E.A. Olevsky, Theory of sintering: from discrete to continuum, Mater. Sci. Eng. R Rep. 23(1998) 41-100.

[35]. R. Zuo, E. Aulbach, J. Rödel, Experimental determination of sintering stresses and sintering viscosities, Acta Mater. 51(2003) 4563-4574.

[36]. R.K. Bordia, G.W. Scherer, On constrained sintering—I. Constitutive model for a sintering body, Acta Metall. 36(1988) 2393-2397.

[37]. R. Raj, R.K. Bordia, Sintering behavior of bi-modal powder compacts, Acta Metall. 32(1984) 1003-1019.

[38]. P.Z. Cai, G.L. Messing, D.J. Green, Determination of the Mechanical Response of Sintering Compacts by Cyclic Loading Dilatometry, J. Am. Ceram. Soc. 80(1997) 445-452.

[39]. C.H. Hsueh, A.G. Evans, R.M. Cannon, R.J. Brook, Viscoelastic stresses and sintering damage in heterogeneous powder compacts, Acta Metall. 34(1986) 927-936.

[40]. D.J. Green, O. Guillon, J. Rödel, Constrained sintering: A delicate balance of scales, J. Eur. Ceram. Soc. 28(2008) 1451-1466.

[41]. J.K. Mackenzie, R. Shuttleworth, A Phenomenological Theory of Sintering, Proc. Phys. Soc., B. 62(1949) 833-852.

[42]. G.W. Scherer, Sintering inhomogeneous glasses: Application to optical waveguides, J. Non-Cryst. Solids. 34(1979) 239-256.

[43]. G.W. Scherer, Sintering of Low-Density Glasses: I, Theory, J. Am. Ceram. Soc. 60(1977) 236-239.

[44]. V. Skorohod, Rheological basis of the theory of sintering, Kiev: Naukova Dumka. (1972).

[45]. V. Skorohod, E. Olevsky, Continuum theory for sintering of the porous bodies: model and application, Sci. Sinter,. 23(1991) 79-91.

[46]. R.M. McMeeking, L.T. Kuhn, A diffusional creep law for powder compacts, Acta Metall. Mater. 40(1992) 961-969.

[47]. A.C.F. Cocks, Overview no. 117 The structure of constitutive laws for the sintering of fine grained materials, Acta Metall. Mater. 42(1994) 2191-2210.

[48]. J. Svoboda, H. Riedel, H. Zipse, Equilibrium pore surfaces, sintering stresses and constitutive equations for the intermediate and late stages of sintering—I. computation of equilibrium surfaces, Acta Metall. Mater. 42(1994) 435-443.

[49]. H. Riedel, H. Zipse, J. Svoboda, Equilibrium pore surfaces, sintering stresses and constitutive equations for the intermediate and late stages of sintering—II. Diffusional densification and creep, Acta Metall. Mater. 42(1994) 445-452.

[50]. M.N. Rahaman, L.C. De Jonghe, R.J. Brook, Effect of Shear Stress on Sintering, J. Am. Ceram. Soc. 69(1986) 53-58.

[51]. K.R. Venkatachari, R. Raj, Shear Deformation and Densification of Powder Compacts, J. Am. Ceram. Soc. 69(1986) 499-506.

[52]. J. Chang, O. Guillon, J. Rödel, S.-J.L. Kang, Uniaxial viscosity of gadolinium-doped ceria determined by discontinuous sinter forging, J. Eur. Ceram. Soc. 27(2007) 3127-3133.

[53]. J.-B. Ollagnier, O. Guillon, J. Rödel, Viscosity of LTCC Determined by Discontinuous Sinter-Forging, Int. J. Appl. Ceram. Technol. 3(2006) 437-441.

[54]. G. Okuma, J. Gonzalez-Julian, O. Guillon, F. Wakai, Comparison between sinter forging and X-ray microtomography methods for determining sintering stress and bulk viscosity, J. Eur. Ceram. Soc. 38(2018) 2053-2058.

[55]. Z.Z. Du, A.C.F. Cocks, Constitutive models for the sintering of ceramic components—I. Material models, Acta Metall. Mater. 40(1992) 1969-1979.

[56]. J.-B. Ollagnier, O. Guillon, J. Rödel, Effect of Anisotropic Microstructure on the Viscous Properties of an LTCC Material, J. Am. Ceram. Soc. 90(2007) 3846-3851.

[57]. R.K. Bordia, G.W. Scherer, On constrained sintering—II. Comparison of constitutive models, Acta Metall. 36(1988) 2399-2409.

[58]. R. Zuo, E. Aulbach, J. Rödel, Viscous Poisson's coefficient determined by discontinuous hot forging, J. Mater. Res. 18(2003) 2170-2176.

[59]. S.M. Salamone, L.C. Stearns, R.K. Bordia, M.P. Harmer, Effect of Rigid Inclusions on the Densification and Constitutive Parameters of Liquid-Phase-Sintered $YBa_2Cu_3O_{6+x}$ Powder Compacts, J. Am. Ceram. Soc. 86(2003) 883-892.

[60]. F. Wakai, Z.S. Nikolić, Effect of grain boundary sliding on shear viscosity and viscous Poisson's ratio in macroscopic shrinkage during sintering, Acta Mater. 59(2011) 774-784.

[61]. T. Kraft, H. Riedel, Numerical simulation of solid state sintering; model and application, J. Eur. Ceram. Soc. 24(2004) 345-361.

[62]. R. Raj, Analysis of the Sintering Pressure, J. Am. Ceram. Soc. 70(1987) C210-C211.

[63]. R. Zuo, E. Aulbach, J. Rödel, Continuum Mechanical Approach to Sintering of Nanocrystalline Zirconia, Adv. Eng. Mater. 7(2005) 949-952.

[64]. J. Kanters, U. Eisele, J. Rödel, Cosintering Simulation and Experimentation: Case Study of Nanocrystalline Zirconia, J. Am. Ceram. Soc. 84(2001) 2757-2763.

[65]. E.A. Olevsky, D.V. Dudina, Sintering by High-Voltage Electric Pulses, Field-Assisted Sintering: Science and Applications, Springer International Publishing, Cham, 2018, pp. 37-87.

[66]. E.A. Olevsky, D.V. Dudina, Sintering by Low-Voltage Electric Pulses (Including Spark Plasma Sintering (SPS)), Field-Assisted Sintering: Science and Applications, Springer International Publishing, Cham, 2018, pp. 89-191.

[67]. S. Grasso, Y. Sakka, G. Maizza, Electric current activated/assisted sintering (ECAS): a review of patents 1906-2008, Sci. Technol. Adv. Mater. 10(2009) 053001-053001.

[68]. A.J. Jacobson, Materials for Solid Oxide Fuel Cells, Chem. Mater. 22(2010) 660-674.

[69]. H. Zhu, J. Liu, Emerging applications of spark plasma sintering in all solid-state lithium-ion batteries and beyond, J. Power Sources. 391(2018) 10-25.

[70]. R. Kali, A. Mukhopadhyay, Spark plasma sintered/synthesized dense and nanostructured materials for solid-state Li-ion batteries: Overview and perspective, J. Power Sources. 247(2014) 920-931.

[71]. T. Jiang, Z. Wang, J. Zhang, X. Hao, D. Rooney, Y. Liu, W. Sun, J. Qiao, K. Sun, Understanding the Flash Sintering of Rare-Earth-Doped Ceria for Solid Oxide Fuel Cell, J. Am. Ceram. Soc. 98(2015) 1717-1723.

[72]. J.S.C. Francis, M. Cologna, D. Montinaro, R. Raj, Flash Sintering of Anode–Electrolyte Multilayers for SOFC Applications, J. Am. Ceram. Soc. 96(2013) 1352-1354.

[73]. A.M. Laptev, H. Zheng, M. Bram, M. Finsterbusch, O. Guillon, High-pressure field assisted sintering of half-cell for all-solid-state battery, Mater. Lett. 247(2019) 155-158.

[74]. S.-W. Baek, J.-M. Lee, T.Y. Kim, M.-S. Song, Y. Park, Garnet related lithium ion conductor processed by spark plasma sintering for all solid state batteries, J. Power Sources. 249(2014) 197-206.

[75]. F. Lalère, J.B. Leriche, M. Courty, S. Boulineau, V. Viallet, C. Masquelier, V. Seznec, An all-solid state NASICON sodium battery operating at 200 °C, J. Power Sources. 247(2014) 975-980.

[76]. S.F. Wang, J. Zhang, D.W. Luo, F. Gu, D.Y. Tang, Z.L. Dong, G.E.B. Tan, W.X. Que, T.S. Zhang, S. Li, L.B. Kong, Transparent ceramics: Processing, materials and applications, Prog. Solid State Chem. 41(2013) 20-54.

[77]. L. An, A. Ito, T. Goto, Transparent yttria produced by spark plasma sintering at moderate temperature and pressure profiles, J. Eur. Ceram. Soc. 32(2012) 1035-1040.

[78]. O. Guillon, Effects of Applied Stress and Heating Rate in Field Assisted Sintering, in: R. Castro and K. van Benthem, (Eds), Sintering: Mechanisms of Convention Nanodensification and Field Assisted Processes, Springer Berlin Heidelberg, Berlin, Heidelberg, 2013, pp. 195-213.

[79]. G. Bernard-Granger, A. Addad, G. Fantozzi, G. Bonnefont, C. Guizard, D. Vernat, Spark plasma sintering of a commercially available granulated zirconia powder: Comparison with hot-pressing, Acta Mater. 58(2010) 3390-3399.

[80]. R.C. Frye, J.E. Griffith, Y.H. Wong, A Field-Assisted Bonding Process for Silicon Dielectric Isolation, J. Electrochem. Soc. 133(1986) 1673-1677.

[81]. H. Junjie, W. Xiaohui, C. Renzheng, G. Zhilun, L. Longtu, Preparation of Textured Bismuth Titanate Ceramics Using Spark Plasma Sintering, J. Am. Ceram. Soc. 87(2004) 1404-1406.

[82]. U. Anselmi-Tamburini, J.E. Garay, Z.A. Munir, Fast low-temperature consolidation of bulk nanometric ceramic materials, Scripta Mater. 54(2006) 823-828.

[83]. S.C. Byeon, K.S. Hong, Electric field assisted bonding of ceramics, Mater. Sci. Eng. A. 287(2000) 159-170.

[84]. A.M. Raftery, J.G. Pereira da Silva, D.D. Byler, D.A. Andersson, B.P. Uberuaga, C.R. Stanek, K.J. McClellan, Onset conditions for flash sintering of UO_2, J. Nucl. Mater. 493(2017) 264-270.

[85]. H. Charalambous, S.K. Jha, X.L. Phuah, H. Wang, H. Wang, J.S. Okasinski, T. Tsakalakos, In situ measurement of temperature and reduction of rutile titania using energy dispersive x-ray diffraction, J. Eur. Ceram. Soc. (2018).

[86]. S.K. Jha, H. Charalambous, H. Wang, X.L. Phuah, C. Mead, J. Okasinski, H. Wang, T. Tsakalakos, In-situ observation of oxygen mobility and abnormal lattice expansion in ceria during flash sintering, Ceram. Int. 44(2018) 15362-15369.

[87]. D. Liu, J. Liu, Y. Gao, F. Liu, K. Li, J. Xia, Y. Wang, L. An, Effect of the applied electric field on the microstructure and electrical properties of flash-sintered 3YSZ ceramics, Ceram. Int. 42(2016) 19066-19070.

[88]. J.-C. M'Peko, J.S.C. Francis, R. Raj, Impedance Spectroscopy and Dielectric Properties of Flash Versus Conventionally Sintered Yttria-Doped Zirconia Electroceramics Viewed at the Microstructural Level, J. Am. Ceram. Soc. 96(2013) 3760-3767.

[89]. J. Zhang, F. Meng, R.I. Todd, Z. Fu, The nature of grain boundaries in alumina fabricated by fast sintering, Scripta Mater. 62(2010) 658-661.

[90]. F. Meng, Z. Fu, J. Zhang, H. Wang, W. Wang, Y. Wang, R. Todd, Q. Zhang, Study on the structure and properties of fine-grained alumina fast sintered with high heating rate, Mater. Res. Bull. 43(2008) 3521-3528.

[91]. M. Tokita, Recent and future progress on advanced ceramics sintering by Spark Plasma Sintering, Nanotechnologies in Russia. 10(2015) 261-267.

[92]. S. Ghosh, A.H. Chokshi, P. Lee, R. Raj, A Huge Effect of Weak dc Electrical Fields on Grain Growth in Zirconia, J. Am. Ceram. Soc. 92(2009) 1856-1859.

[93]. F. Iguchi, C.-T. Chen, H. Yugami, S. Kim, Direct evidence of potential barriers at grain boundaries in Y-doped $BaZrO_3$ from dc-bias dependence measurements, J. Mater. Chem. 21(2011) 16517-16523.

[94]. S.K. Kim, S. Khodorov, C.-T. Chen, S. Kim, I. Lubomirsky, How to interpret current–voltage relationships of blocking grain boundaries in oxygen ionic conductors, PCCP. 15(2013) 8716-8721.

[95]. J. Maier, Ionic conduction in space charge regions, Prog. Solid State Chem. 23(1995) 171-263.

[96]. X. Guo, J. Maier, Grain Boundary Blocking Effect in Zirconia: A Schottky Barrier Analysis, J. Electrochem. Soc. 148(2001) E121-E126.

[97]. S. Kim, J. Fleig, J. Maier, Space charge conduction: Simple analytical solutions for ionic and mixed conductors and application to nanocrystalline ceria, PCCP. Physical chemistry chemical physics. 5(2003) 2268-2273.

[98]. X. Guo, W. Sigle, J. Maier, Blocking Grain Boundaries in Yttria-Doped and Undoped Ceria Ceramics of High Purity, J. Am. Ceram. Soc. 86(2003) 77-87.

[99]. S. Diouf, A. Fedrizzi, A. Molinari, A fractographic and microstructural analysis of the neck regions of coarse copper particles consolidated by spark plasma sintering, Mater. Lett. 111(2013) 17-19.

[100]. G. Corapcioglu, M. Ali Gulgun, K. Kisslinger, S. Sturm, S.K. Jha, R. Raj, Microstructure and microchemistry of flash sintered K 0.5 Na 0.5 NbO 3, J. Ceram. Soc. Jpn. 124(2016) 321-328.

[101]. H. Yoshida, A. Uehashi, T. Tokunaga, K. Sasaki, T. Yamamoto, Formation of grain boundary second phase in $BaTiO_3$ polycrystal under a high DC electric field at elevated temperatures, J. Ceram. Soc. Jpn. 124(2016) 388-392.

[102]. A. Uehashi, K. Sasaki, T. Tokunaga, H. Yoshida, T. Yamamoto, Formation of secondary phase at grain boundary of flash-sintered $BaTiO_3$, Microscopy. 63(2014) i19-i20.

[103]. K.S.N. Vikrant, R.E. García, Charged grain boundary transitions in ionic ceramics for energy applications, npj Computational Materials. 5(2019) 24.

[104]. T.B. Holland, U. Anselmi-Tamburini, D.V. Quach, T.B. Tran, A.K. Mukherjee, Effects of local Joule heating during the field assisted sintering of ionic ceramics, J. Eur. Ceram. Soc. 32(2012) 3667-3674.

[105]. A.S. Semenov, J. Trapp, M. Nöthe, O. Eberhardt, T. Wallmersperger, B. Kieback, Thermo-electro-mechanical modeling, simulation and experiments of field-assisted sintering, J. Mater. Sci. 54(2019) 10764-10783.

[106]. T.B. Holland, U. Anselmi-Tamburini, D.V. Quach, T.B. Tran, A.K. Mukherjee, Local field strengths during early stage field assisted sintering (FAST) of dielectric materials, J. Eur. Ceram. Soc. 32(2012) 3659-3666.

[107]. J.-W. Jeong, J.-H. Han, D.-Y. Kim, Effect of Electric Field on the Migration of Grain Boundaries in Alumina, J. Am. Ceram. Soc. 83(2000) 915-918.

[108]. D. Yadav, R. Raj, Two unique measurements related to flash experiments with yttria-stabilized zirconia, J. Am. Ceram. Soc. 100(2017) 5374-5378.

[109]. T.P. Mishra, V. Avila, R.R.I. Neto, M. Bram, O. Guillon, R. Raj, On the role of Debye temperature in the onset of flash in three oxides, Scripta Mater. 170(2019) 81-84.

[110]. M. Jongmanns, R. Raj, D.E. Wolf, Generation of Frenkel defects above the Debye temperature by proliferation of phonons near the Brillouin zone edge, New Journal of Physics. 20(2018) 093013.

[111]. M. Jongmanns, D.E. Wolf, Element-specific displacements in defect-enriched TiO_2: Indication of a flash sintering mechanism, J. Am. Ceram. Soc. 103(2020) 589-596.

[112]. B. Yoon, D. Yadav, R. Raj, E. Sortino, S. Ghose, P. Sarin, D. Shoemaker, Measurement of O and Ti atom displacements in TiO_2 during flash sintering experiments, J. Am. Ceram. Soc. 101(2018) 1811-1817.

[113]. A.V. Granato, Interstitialcy model for condensed matter states of face-centered-cubic metals, Phys. Rev. Lett. 68(1992) 974-977.

[114]. S.V. Khonik, A.V. Granato, D.M. Joncich, A. Pompe, V.A. Khonik, Evidence of Distributed Interstitialcy-Like Relaxation of the Shear Modulus due to Structural Relaxation of Metallic Glasses, Phys. Rev. Lett. 100(2008) 065501.

[115]. J. Janek, C. Korte, Electrochemical blackening of yttria-stabilized zirconia – morphological instability of the moving reaction front, Solid State Ion. 116(1999) 181-195.

[116]. J.S. Thorp, H.P. Buckley, The dielectric constants of current-blackened single crystral yttria-stabilized zirconia, J. Mater. Sci. 8(1973) 1401-1408.

[117]. S. Jo, R. Raj, Transition to electronic conduction at the onset of flash in cubic zirconia, Scripta Mater. 174(2020) 29-32.

[118]. N. Masó, A.R. West, Electronic Conductivity in Yttria-Stabilized Zirconia under a Small dc Bias, Chem. Mater. 27(2015) 1552-1558.

[119]. Y. Dong, I.W. Chen, Oxygen potential transition in mixed conducting oxide electrolyte, Acta Mater. 156(2018) 399-410.

[120]. Y. Dong, H. Wang, I.-W. Chen, Electrical and hydrogen reduction enhances kinetics in doped zirconia and ceria: I. grain growth study, J. Am. Ceram. Soc. 100(2017) 876-886.

[121]. Y. Dong, I.-W. Chen, Electrical and hydrogen reduction enhances kinetics in doped zirconia and ceria: II. Mapping electrode polarization and vacancy condensation in YSZ, J. Am. Ceram. Soc. 101(2018) 1058-1073.

[122]. W. Qin, H. Majidi, J. Yun, K. van Benthem, Electrode Effects on Microstructure Formation During FLASH Sintering of Yttrium-Stabilized Zirconia, J. Am. Ceram. Soc. 99(2016) 2253-2259.

[123]. Y. Du, A.J. Stevenson, D. Vernat, M. Diaz, D. Marinha, Estimating Joule heating and ionic conductivity during flash sintering of 8YSZ, J. Eur. Ceram. Soc. 36(2016) 749-759.

[124]. A. Younis, D. Chu, S. Li, Cerium Oxide Nanostructures and their Applications, Functionalized Nanomaterials, 2016.

[125]. J. Kašpar, P. Fornasiero, M. Graziani, Use of CeO_2-based oxides in the three-way catalysis, Catal. Today. 50(1999) 285-298.

[126]. H.C. Yao, Y.F.Y. Yao, Ceria in automotive exhaust catalysts: I. Oxygen storage, J. Catal. 86(1984) 254-265.

[127]. P. Jasinski, T. Suzuki, H.U. Anderson, Nanocrystalline undoped ceria oxygen sensor, Sensor Actuat B-Chem. 95(2003) 73-77.

[128]. H.J. Beie, A. Gnörich, Oxygen gas sensors based on CeO_2 thick and thin films, Sensor Actuat B-Chem. 4(1991) 393-399.

[129]. J.G. Lee, J.H. Park, Y.G. Shul, Tailoring gadolinium-doped ceria-based solid oxide fuel cells to achieve 2 W cm−2 at 550 °C, Nat. Commun. 5(2014) 4045.

[130]. M. Melchionna, P. Fornasiero, The role of ceria-based nanostructured materials in energy applications, Mater. Today. 17(2014) 349-357.

[131]. D.P. Fagg, A.L. Shaula, V.V. Kharton, J.R. Frade, High oxygen permeability in fluorite-type $Ce_{0.8}Pr_{0.2}O_{2-\delta}$ via the use of sintering aids, J. Membr. Sci. 299(2007) 1-7.

[132]. M.P. Lobera, J.M. Serra, S.P. Foghmoes, M. Søgaard, A. Kaiser, On the use of supported ceria membranes for oxyfuel process/syngas production, J. Membr. Sci. 385-386(2011) 154-161.

[133]. L. Malavasi, C.A.J. Fisher, M.S. Islam, Oxide-ion and proton conducting electrolyte materials for clean energy applications: structural and mechanistic features, Chem. Soc. Rev. 39(2010) 4370-4387.

[134]. S.R. Bishop, Chemical expansion of solid oxide fuel cell materials: A brief overview, Acta Mechanica Sinica. 29(2013) 312-317.

[135]. L.P. Bulat, A.V. Novotel'nova, V.B. Osvenskii, A.I. Sorokin, D.A. Pshenai-Severin, A.S. Tukmakova, D. Yerezhep, Field-assisted sintering of effective materials for alternative power engineering, Tech. Phys. Lett. 43(2017) 658-661.

[136]. D.Y. Wang, D.S. Park, J. Griffith, A.S. Nowick, Oxygen-ion conductivity and defect interactions in yttria-doped ceria, Solid State Ion. 2(1981) 95-105.

[137]. H. Inaba, H. Tagawa, Ceria-based solid electrolytes, Solid State Ion. 83(1996) 1-16.

[138]. H. Yahiro, K. Eguchi, H. Arai, Electrical properties and reducibilities of ceria-rare earth oxide systems and their application to solid oxide fuel cell, Solid State Ion. 36(1989) 71-75.

[139]. C.W.M. Castleton, J. Kullgren, K. Hermansson, Tuning LDA+U for electron localization and structure at oxygen vacancies in ceria, J. Chem. Phys. 127(2007) 244704.

[140]. M. Mogensen, N.M. Sammes, G.A. Tompsett, Physical, chemical and electrochemical properties of pure and doped ceria, Solid State Ion. 129(2000) 63-94.

[141]. I.K. Naik, T.Y. Tien, Small-polaron mobility in nonstoichiometric cerium dioxide, J. Phys. Chem. Solids. 39(1978) 311-315.

[142]. B.C.H. Steele, J.M. Floyd, The Oxygen Self-Diffusion and Electrical Transport Properties of Non-stoichiometric Ceria and Ceria Solid Solutions, Proc. Brit. Ceramic Soc. 19(1971) 55-76.

[143]. P.-L. Chen, I.W. Chen, Role of Defect Interaction in Boundary Mobility and Cation Diffusivity of CeO_2, J. Am. Ceram. Soc. 77(1994) 2289-2297.

[144]. P.-L. Chen, I.W. Chen, Grain Growth in CeO_2: Dopant Effects, Defect Mechanism, and Solute Drag, J. Am. Ceram. Soc. 79(1996) 1793-1800.

[145]. S. Omar, Doped Ceria for Solid Oxide Fuel Cells, Cerium Oxide - Applications and Attributes, 2019.

[146]. T.H. Etsell, S.N. Flengas, Electrical properties of solid oxide electrolytes, Chem. Rev. 70(1970) 339-376.

[147]. Z.-P. Li, T. Mori, F. Ye, D. Ou, G.J. Auchterlonie, J. Zou, J. Drennan, Cerium-Reduction-Induced Defects Clustering, Ordering, and Associated Microstructure Evolution in Yttrium-Doped Ceria, J Phys. Chem. C. 116(2012) 5435-5443.

[148]. J.A. Kilner, B.C.H. Steele, 5 - Mass Transport in Anion-Deficient Fluorite Oxides, in: O.T. Sørensen, Editor, Nonstoichiometric Oxides, Academic Press, 1981, pp. 233-269.

[149]. M. Nakayama, M. Martin, First-principles study on defect chemistry and migration of oxide ions in ceria doped with rare-earth cations, PCCP. 11(2009) 3241-3249.

[150]. S. Beschnitt, T. Zacherle, R.A. De Souza, Computational Study of Cation Diffusion in Ceria, J Phys. Chem. C. 119(2015) 27307-27315.

[151]. Y. Dong, L. Qi, J. Li, I.-W. Chen Electron Localization Enhances Cation Diffusion in Reduced ZrO_2, CeO_2 and $BaTiO_3$. arXiv e-prints, 2018. DOI: arXiv:1808.05198.

[152]. Y. Kinemuchi, K. Watari, Dilatometer analysis of sintering behavior of nano-CeO_2 particles, J. Eur. Ceram. Soc. 28(2008) 2019-2024.

[153]. V. Esposito, D.W. Ni, Z. He, W. Zhang, A.S. Prasad, J.A. Glasscock, C. Chatzichristodoulou, S. Ramousse, A. Kaiser, Enhanced mass diffusion phenomena in highly defective doped ceria, Acta Mater. 61(2013) 6290-6300.

[154]. D.W. Ni, J.A. Glasscock, A. Pons, W. Zhang, A. Prasad, S. Sanna, N. Pryds, V. Esposito, Densification of Highly Defective Ceria by High Temperature Controlled Re-Oxidation, J. Electrochem. Soc. 161(2014) F3072-F3078.

[155]. S.M. Haile, G. Staneff, K.H. Ryu, Non-stoichiometry, grain boundary transport and chemical stability of proton conducting perovskites, J. Mater. Sci. 36(2001) 1149-1160.

[156]. A. Lasia, Definition of Impedance and Impedance of Electrical Circuits, Electrochemical Impedance Spectroscopy and its Applications, Springer New York, New York, NY, 2014, pp. 7-66.

[157]. E. Barsoukov, J.R. Macdonald, eds. Impedance Spectroscopy: Theory, Experiment, and Applications. 2nd ed. 2005, John Wiley & Sons, Inc: Hoboken, NJ.

[158]. K. Funke, D. Wilmer, Concept of mismatch and relaxation derived from conductivity spectra of solid electrolytes, Solid State Ion. 136-137(2000) 1329-1333.

[159]. B.A. Boukamp, Derivation of a Distribution Function of Relaxation Times for the (fractal) Finite Length Warburg, Electrochim. Acta. 252(2017) 154-163.

[160]. J.T.S. Irvine, D.C. Sinclair, A.R. West, Electroceramics: Characterization by Impedance Spectroscopy, Adv. Mater. 2(1990) 132-138.

[161]. C. Ho, Application of AC techniques to kinetic studies of electrochemical systems, in Department of Materials Science and Engineering. 1980, Stanford University.

[162]. N.M. Beekmans, L. Heyne, Correlation between impedance, microstructure and composition of calcia-stabilized zirconia, Electrochim. Acta. 21(1976) 303-310.

[163]. LA-950 Laser Particle Size Analyzer. Available from: https://www.horiba.com/de/scientific/products/particle-characterization/zeta-potential-analysis/details/la-950-laser-particle-size-analyzer-108/.

[164]. Principles and Applications of Laser Diffraction Technology. 2018; Available from: https://www.azom.com/article.aspx?ArticleID=16153.

[165]. A. Hartridge, M.G. Krishna, A.K. Bhattacharya, Structure and Optical Properties of Nanocrystalline Yttria Doped Ceria Thin Films, Int. J. Mod Phys B. 12(1998) 1573-1583.

[166]. T.-S. Oh, Y.S. Tokpanov, Y. Hao, W. Jung, S.M. Haile, S. R., Determination of optical and microstructural parameters of ceria films, J. Appl. Phys. 112(2012) 103535.

[167]. Physisorption Technology. Available from: https://www.horiba.com/us/en/scientific/products/particle-characterization/technology/surface-area/.

[168]. S. Brunauer, P.H. Emmett, E. Teller, Adsorption of Gases in Multimolecular Layers, JACS. 60(1938) 309-319.

[169]. P. Coppens, The structure factor, in: U. Shmueli, Editor, International Tables for Crystallography Volume B: Reciprocal space, Springer Netherlands, Dordrecht, 2001, pp. 10-24.

[170]. G.K. Williamson, W.H. Hall, X-ray line broadening from filed aluminium and wolfram, Acta Metall. 1(1953) 22-31.

[171]. TMA 402 F1/F3 Hyperion® Thermomechanical Analyzer - Vertical Dilatometer. Available from: https://www.netzsch-thermal-analysis.com/en/products-solutions/thermomechanical-analysis/tma-402-f1f3-hyperion/.

[172]. E. Aulbach, R. Zuo, J. Rödel, Laser-assisted high-resolution loading dilatometer and applications, Exp. Mech. 44(2004) 71-75.

[173]. H. Yoshida, Y. Sasaki, Low temperature and high strain rate superplastic flow in structural ceramics induced by strong electric-field, Scripta Mater. 146(2018) 173-177.

[174]. A. Mohanram, G.L. Messing, D.J. Green, Measurement of Viscosity of Densifying Glass-Based Systems by Isothermal Cyclic Loading Dilatometry, J. Am. Ceram. Soc. 87(2004) 192-196.

[175]. X. Hao, Y. Liu, Z. Wang, J. Qiao, K. Sun, A novel sintering method to obtain fully dense gadolinia doped ceria by applying a direct current, J. Power Sources. 210(2012) 86-91.

[176]. L. Spiridigliozzi, M. Biesuz, G. Dell'Agli, E. Di Bartolomeo, F. Zurlo, V.M. Sglavo, Microstructural and electrical investigation of flash-sintered Gd/Sm-doped ceria, J. Mater. Sci. 52(2017) 7479-7488.

[177]. A.R.C. Gerlt, A.K. Criner, L. Semiatin, E.J. Payton, On the grain size proportionality constants calculated in M.I. Mendelson's "Average Grain Size in Polycrystalline Ceramics", J. Am. Ceram. Soc.

[178]. O. Guillon, L. Weiler, J. Rödel, Anisotropic Microstructural Development During the Constrained Sintering of Dip-Coated Alumina Thin Films, J. Am. Ceram. Soc. 90(2007) 1394-1400.

[179]. R. Mücke, N.H. Menzler, H.P. Buchkremer, D. Stöver, Cofiring of Thin Zirconia Films During SOFC Manufacturing, J. Am. Ceram. Soc. 92(2009) S95-S102.

[180]. Y. Gu, G. Li, G. Meng, D. Peng, Sintering and electrical properties of coprecipitation prepared Ce0.8Y0.2O1.9 ceramics, Mater. Res. Bull. 35(2000) 297-304.

[181]. S.I. Ahmad, P. Koteshwar Rao, I.A. Syed, Sintering temperature effect on density, structural and morphological properties of Mg- and Sr-doped ceria, J. Taibah. Univ. Sci. 10(2016) 381-385.

[182]. J.-G. Li, Y. Wang, T. Ikegami, T. Ishigaki, Densification below 1000 °C and grain growth behaviors of yttria doped ceria ceramics, Solid State Ion. 179(2008) 951-954.

[183]. J.-G. Li, T. Ikegami, T. Mori, Low temperature processing of dense samarium-doped CeO_2 ceramics: sintering and grain growth behaviors, Acta Mater. 52(2004) 2221-2228.

[184]. J.M. Heintz, O. Sudre, F.F. Lange, Instability of Polycrystalline Bridges that Span Cracks in Powder Films Densified on a Substrate, J. Am. Ceram. Soc. 77(1994) 787-791.

[185]. R. Raj, Joule heating during flash-sintering, J. Eur. Ceram. Soc. 32(2012) 2293-2301.

[186]. P. Kumar M K, D. Yadav, J.-M. Lebrun, R. Raj, Flash sintering with current rate: A different approach, J. Am. Ceram. Soc. 102(2019) 823-835.

[187]. H. Yoshida, K. Morita, B.-N. Kim, Y. Sakka, T. Yamamoto, Reduction in sintering temperature for flash-sintering of yttria by nickel cation-doping, Acta Mater. 106(2016) 344-352.

[188]. M. Yu, S. Grasso, R. McKinnon, T. Saunders, M.J. Reece, Review of flash sintering: materials, mechanisms and modelling, Adv. Appl. Ceram. 116(2017) 24-60.

[189]. R. Zuo, E. Aulbach, R.K. Bordia, J. Rödel, Critical Evaluation of Hot Forging Experiments: Case Study in Alumina, J. Am. Ceram. Soc. 86(2003) 1099-1105.

[190]. C. Cao, R. Mücke, O. Guillon, Effect of AC field on uniaxial viscosity and sintering stress of ceria, Acta Mater. 182(2020) 77-86.

[191]. M.N. Kelly, S.A. Bojarski, G.S. Rohrer, The temperature dependence of the relative grain-boundary energy of yttria-doped alumina, J. Am. Ceram. Soc. 100(2017) 783-791.

[192]. A. Tsoga, P. Nikolopoulos, Surface and grain-boundary energies in yttria-stabilized zirconia (YSZ-8 mol%), J. Mater. Sci. 31(1996) 5409-5413.

[193]. J. Chang, O. Guillon, J. Rödel, S.-J.L. Kang, Characterization of warpage behaviour of Gd-doped ceria/NiO–yttria stabilized zirconia bi-layer samples for solid oxide fuel cell application, J. Power Sources. 185(2008) 759-764.

[194]. S.K. Jha, R. Raj, Electric Fields Obviate Constrained Sintering, J. Am. Ceram. Soc. 97(2014) 3103-3109.

[195]. R. Zuo, J. Rödel, Temperature dependence of constitutive behaviour for solid-state sintering of alumina, Acta Mater. 52(2004) 3059-3067.

[196]. R.M. Batista, E.N.S. Muccillo, Dilatometry analysis of the sintering process of nanostructured gadolinia-doped ceria, J. Therm. Anal. Calorim. 126(2016) 1007-1013.

[197]. X. Vendrell, D. Yadav, R. Raj, A.R. West, Influence of flash sintering on the ionic conductivity of 8 mol% yttria stabilized zirconia, J. Eur. Ceram. Soc. 39(2019) 1352-1358.

[198]. S. Lübke, H.D. Wiemhöfer, Electronic conductivity of Gd-doped ceria with additional Pr-doping, Solid State Ion. 117(1999) 229-243.

[199]. S. Wang, T. Kobayashi, M. Dokiya, T. Hashimoto, Electrical and Ionic Conductivity of Gd-Doped Ceria, J. Electrochem. Soc. 147(2000) 3606-3609.

[200]. J.P. Parras, C. Cao, Z. Ma, R. Mücke, L. Jin, R. Dunin-Borkowski, O. Guillon, R.A. De Souza, The grain-boundary resistance of CeO_2 ceramics: A combined microscopy-spectroscopy-simulation study of a dilute solution, J. Am. Ceram. Soc. n/a.

[201]. S. Grieshammer, R.A. De Souza, 7 - Fundamentals of electrical conduction in ceramics, in: O. Guillon, Editor, Advanced Ceramics for Energy Conversion and Storage, Elsevier, 2020, pp. 277-320.

Band / Volume 497
Aquisition of temporally and spatially highly resolved data sets of relevant trace substances for model development and model evaluation purposes using a mobile measuring laboratory
D. Klemp, R. Wegener, R. Dubus, U. Javed (2020), 110 pp
ISBN: 978-3-95806-465-2

Band / Volume 498
Charakterisierung des Werkstoffverhaltens während des Kosinterns einer neuartigen, inert gestützten Festoxidbrennstoffzelle
F. Grimm (2020), ix, 168 pp
ISBN: 978-3-95806-482-9

Band / Volume 499
WEGE FÜR DIE ENERGIEWENDE
Kosteneffiziente und klimagerechte Transformationsstrategien für das deutsche Energiesystem bis zum Jahr 2050
M. Robinius et al (2020), VIII, 141 pp
ISBN: 978-3-95806-483-6

Band / Volume 500
Mechanical Behavior of Solid Electrolyte Materials for Lithium-ion Batteries
G. Yan (2020), x, 139 pp
ISBN: 978-3-95806-484-3

Band / Volume 501
Retrieval of atmospheric quantities from remote sensing measurements of nightglow emissions in the MLT region
Q. Chen (2020), 208 pp
ISBN: 978-3-95806-485-0

Band / Volume 502
Auswirkungen der Energiewende auf das deutsche Gastransportsystem
B. Gillessen (2020), XVII, 186
ISBN: 978-3-95806-487-4

Band / Volume 503
Lagrangian Simulation of Stratospheric Water Vapour: Impact of Large-Scale Circulation and Small-Scale Transport Processes
L. Poshyvailo (2020), 124 pp
ISBN: 978-3-95806-488-1

Band / Volume 504
Water Management in Automotive Polymer-Electrolyte-Membrane Fuel Cell Stacks
S. Asanin (2020), XVIII, 172 pp
ISBN: 978-3-95806-491-1

Band / Volume 505
Towards a new real-time irrigation scheduling method: observation, modelling and their integration by data assimilation
D. Li (2020), viii, 94 pp
ISBN: 978-3-95806-492-8

Band / Volume 506
Modellgestützte Analyse kosteneffizienter CO_2-Reduktionsstrategien
P. M. Lopion (2020), XIV, 269 pp
ISBN: 978-3-95806-493-5

Band / Volume 507
Integration of Renewable Energy Sources into the Future European Power System Using a Verified Dispatch Model with High Spatiotemporal Resolution
C. Syranidou (2020), VIII, 242 pp
ISBN: 978-3-95806-494-2

Band / Volume 508
Solar driven water electrolysis based on silicon solar cells and earth-abundant catalysts
K. Welter (2020), iv, 165 pp
ISBN: 978-3-95806-495-9

Band / Volume 509
Electric Field Assisted Sintering of Gadolinium-doped Ceria
T. P. Mishra (2020), x, 195 pp
ISBN: 978-3-95806-496-6

Band / Volume 510
Effect of electric field on the sintering of ceria
C. Cao (2020), xix, 143 pp
ISBN: 978-3-95806-497-3

Weitere ***Schriften des Verlags im Forschungszentrum Jülich*** unter
http://wwwzb1.fz-juelich.de/verlagextern1/index.asp

Energie & Umwelt / Energy & Environment
Band / Volume 510
ISBN 978-3-95806-497-3

Mitglied der Helmholtz-Gemeinschaft

JÜLICH
Forschungszentrum